

AD-A244 460



PL-TR-91-2276(I)

2

**DEVELOPMENT OF A MAGNETOSPHERIC
SPECIFICATION MODEL**

J. W. Freeman	B. A. Bales
R. A. Wolf	R. V. Hilmer
R. W. Spiro	A. Nagai
G-H. Voigt	R. Lambour
B. A. Hausman	

Rice University
Department of Space Physics & Astronomy
Houston, TX 77251

30 June 1991

DTIC
ELECTE
DEC 05 1991
S D D

Final Report Volume I
15 November 1987-31 March 1990

APPROVED FOR PUBLIC RELEASE; DISTRIBUTION UNLIMITED



PHILLIPS LABORATORY
AIR FORCE SYSTEMS COMMAND
HANSCOM AIR FORCE BASE, MASSACHUSETTS 01731-5000

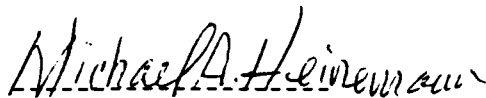
91-16859



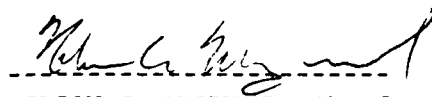
91 12 0

12

This technical report has been reviewed and is approved for publication.

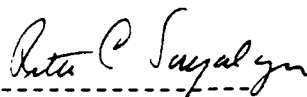


MICHAEL A. HEINEMANN
Contract Manager
Space Plasmas and Fields Br.
Space Physics Division



NELSON C. MAYNARD, Chief
Space Plasmas and Fields Br.
Space Physics Division

FOR THE COMMANDER



RITA C. SAGALYN
Director
Space Physics Division

This report has been reviewed by the ESD Public Affairs Office (PA) and is releasable to the National Technical Information Service (NTIS).

Qualified requestors may obtain additional copies from the Defense Technical Information Center. All others should apply to the National Technical Information Service.

If your address has changed, or if you wish to be removed from the mailing list, or if the addressee is no longer employed by your organization, please notify PL/TSI, Hanscom AFB, MA 01731. This will assist us in maintaining a current mailing list.

Do not return copies of this report unless contractual obligations or notices on a specific document require that it be returned.

Figure 1. The effect of the concentration of the *Agrobacterium* suspension on the transformation efficiency of *Agrobacterium* strains.

Final (15 Nov 1987-31 Mar 1990) Vol I

2. 1. *Plumbeus* *recondens* *nov.*

PE 62101F
PR 2688
TA 04
WU GB

Contract:

F19628-87-K-0001

1. The following is a list of the names of the persons who have been appointed to the various committees of the Board of Directors of the American Telephone and Telegraph Company, for the year ending December 31, 1914:

PL-TR-91-2276 (I)

PL-TR-91-2276 (I)

THE UNIVERSITY OF CHICAGO

THE UNIVERSITY OF CHICAGO

THE UNIVERSITY OF CHICAGO

137

... ..

SAR

CONT OF BLOCK 13:

The model is accompanied by an application program that allows specification of fluxes at an arbitrary point in the magnetosphere within the modeling region. Consistent with its primary function, the MSM has been tested against spacecraft data for 2 substantial storms and has been shown to produce a good characterization of the enhancements of 40 KeV electron fluxes in the equatorial plane. The model never failed to predict high fluxes when they were observed, although it did predict high fluxes in some cases when they were not observed and it did fail to predict flux dropouts observed by the spacecraft. The MSM is ready for adaptation for use in an operational setting where the goal is real-time and retrospective specification of hazardous charged particle fluxes associated with geomagnetic storms.

Accession For	
NTIS ORASH	✓
DTIC	✓
U.S. Government	✓
Instructions	✓
By	
DATE	
APPROVED BY	
SIGNATURE	
A-1	



The following scientists contributed to the research reported in this document:

B. A. Bales

J. W. Freeman, Jr.

B. A. Hausman

R. V. Hilmer

R. Lambour

A. Nagai

R. W. Spiro

G.-H. Voigt

R. A. Wolf

All are employees or students at Rice University, Houston, Texas.

Table of Contents

Cover Page

Form 1473

Abstract of Report

List of all Scientists Who Contributed to the Research

Table of Contents

1. Introduction

1.0. Background

1.1. Objectives

2. Scientific Description of the Magnetospheric Specification Model

2.0. Introduction

2.0.1. Goals and Objectives

2.0.2. Logical Structure of the MSM

2.1. Input Data from the Environmental Database

2.1.0. MSM Input Parameters

2.1.0.1. Parameters called by INDATA

2.1.0.2. The GEO Satellite Particle Data

2.1.1. Input Parameter Interpolation

2.2. Front-end Models and Default Models

2.2.1. Front-end Models

2.2.2. Default Models

2.2.2.1. The Hardy Model of Precipitating Auroral Fluxes

2.2.2.2. The Garrett Model of Geostationary Orbit Fluxes

2.3. The Magnetic-Field Model

2.3.0. Introductory Comments

2.3.1. Inputs to the Magnetic-Field Model

2.3.2. Pre-Computed Magnetic-Field Matrices

2.4. The Electric-Field Model

2.4.0. Introductory Comments

2.4.1. Division of the Ionosphere into Regions

2.4.2. Determination of the Ellipse Parameters A, B, DX, and DY

2.4.2.1. Location of Ellipse 2, i.e., Boundary b

2.4.2.2. Location of Ellipse 3, which is Boundary c

2.4.2.3. Calculation of A, B, DX, DY for Ellipses 2 and 3

2.4.2.4. Calculation of A, B, DX, DY for Ellipse 1

2.4.3. Potential in Region 0 (Polar Cap)

2.4.4. Potential in Region 3 (Middle and Low Latitudes)

2.4.4.0. Introductory Comments

2.4.4.1. General Expression for the Low-Latitude Potential

2.4.4.2. Estimation of $E_{\text{west, max}}(\theta_{\text{shield}})$

2.4.4.3. Estimation of VBAR

2.4.5. Potential in Region 2 (Main Sunward Flow Region of the Auroral Ionosphere)

2.4.6. Potential in Region 1 (The Electric-Field-Reversal Region)

2.4.7. Potentials and Electric Fields on the Boundaries

2.4.8. Numerical Illustrations

2.5. Initial-Condition, Boundary-Condition, and Reference Fluxes

2.5.0. Introductory Comments

2.5.1. Properties of the Kappa Distribution

2.5.2. Calculation of FLXMAT for Electrons

2.5.2.1. FLXMAT for Electrons at $r = 13$

2.5.2.2. FLXMAT for Electrons at $r=6.6$

2.5.2.3. FLXMAT for Electrons at $r = 3$ and 4

2.5.3. Calculation of FLXMAT for H^+ and O^+ Ions

- 2.5.3.0. Introductory Comments
- 2.5.3.1. Calculation of FLXMAT for $r = 13$ for Ions
- 2.5.3.2. Calculation of FLXMAT for $r = 6.6$ for Ions
- 2.5.3.3. Calculation of FLXMAT for $r = 4$ for Ions
- 2.5.3.4. Calculation of FLXMAT for $r = 3$ for Ions
- 2.5.4. Initial-Condition Fluxes
 - 2.5.4.1. Calculation of the value of FLXMAT at grid points
 - 2.5.4.2. Calculation of the Initial Condition Flux
 - 2.5.4.3. Conversion between Fluxes and Number Invariant η
- 2.5.5. The Boundary-Condition on η
- 2.5.6. The Reference Flux
- 2.5.7. The Minimum Flux
- 2.5.8. The Threshold Flux
- 2.6. Particle Tracer and Loss Algorithms
 - 2.6.1. The Equations of Adiabatic Drift
 - 2.6.1.1. Differential Equations
 - 2.6.1.2. The MSM Coordinate Grid
 - 2.6.1.3. Equation of Motion in Terms of the MSM Grid
 - 2.6.2. Operation of the Particle Tracer
 - 2.6.2.1. Walking Test Particles Backwards in Time
 - 2.6.2.2. The Loss Equation and its Integration
 - 2.6.3. Electron-Loss
 - 2.6.3.1. The Strong-Pitch-Angle-Scattering Rate
 - 2.6.3.2. $\eta_{\text{threshold}}$ for Strong Pitch-Angle Scattering
 - 2.6.3.3. Weak Loss Rate
 - 2.6.4. Ion-Loss

- 2.6.4.0. Introductory Comments
 - 2.6.4.1. Charge-Exchange Theory
 - 2.6.4.2. Incorporation of Charge-Exchange Calculations in the MSM
 - 2.6.5. Calculation of Fluxes of Precipitating Particles
 - 2.6.5.0. Introductory Comments
 - 2.6.5.1. Calculation of the Precipitating Electron Fluxes within our Main Modeling Region
 - 2.6.5.2. Electron Precipitation Poleward of our Main Modeling Region
- 2.7. Limitations of the MSM
- 2.8. MSM Output
- 3. **Test Events: March 22, 1979 and April 21-23, 1988**
 - 3.0. Introduction
 - 3.1. The March 22, 1979 Event
 - 3.2. The April 21-23, 1988 Event
 - 3.2.1. Geophysical Conditions for the Event
 - 3.2.2. Comparison With MSM Output
- 4. **Validation Statistics**
 - 4.1 Model Inputs
 - 4.2 Model Outputs
 - 4.2.1. The Interpolation
 - 4.2.2. Results
 - 4.3. The Garrett Model
 - 4.4. Evaluation of Accuracy
 - 4.5. Conclusions
- 5. **MSM Source Code Description and Documentation**
 - 5.0. Language and Documentation

6. The Field line Tracing Program, MAPINT

6.0. Background

6.1. How MAPINT Works

6.2. MAPINT Operating Instructions

6.3. MAPINT Validation using the April 21-23, 1988 Event

7. Summary

Acknowledgements

References

Appendix:

A. Documentation on the MSM and Subroutines

B. MSM Source Code and Subroutines

C. MSM Sample Input and Output

D. MAPINT Source Code and Documentation

E. MSM Reference List: Correlation Studies

F. Hilmer's Thesis

G. Hausman's Thesis

1. INTRODUCTION

1.0. Background

The magnetosphere contains plasma and energetic particles which, during times of magnetic disturbances, pose serious hazards for spacecraft. These hazards take the form of spacecraft surface charging, deep dielectric charging and disturbance of spacecraft electronics by direct penetration of energetic particles. Most commonly the effect is an electrical transient which propagates throughout the spacecraft electronics. Not only can temporary or permanent malfunctions result, but the anomalies may mimic intrinsic or adversary induced electronic component failures.

Diagnosis and prevention of environmentally related spacecraft anomalies requires a knowledge of the space plasma and energetic particle fluxes at each spacecraft at all times. Since most satellites do not carry a complete suite of particle measuring instruments, and even if they did they could not forecast local conditions, it is necessary to develop other means to specify the state of space weather. Fortunately, our understanding of the physics of magnetospheric processes has advanced to the point where it is now possible to build computer models which can, using real-time data from monitoring spacecraft and ground observatories, compute particle fluxes at arbitrary positions in the magnetosphere. The Magnetospheric Specification Model represents the first such operational model to be developed. As this contract report will show, this effort has been remarkably successful.

1.1. Objectives

The objective of this contract has been to develop a comprehensive model of the Earth's magnetosphere for operational use by the Air Weather Service. The model is designed to specify magnetospheric conditions using real-time data provided by an environmental database at the Space Forecast Center. The computational system includes models of global magnetic and electric fields, inner magnetospheric particles, and precipitating auroral particles. It can be operated in conjunction with ionospheric, thermospheric, solar-wind and solar-wind/magnetosphere transport models provided by other contractors. The model makes optimum use of datasets from operational Air Force, DoE and NOAA spacecraft and ground-based observatories. In each case, a back-up source for the required input data values has been provided in order that the model can continue to function in the absence of one or more input values.

2. SCIENTIFIC DESCRIPTION OF THE MAGNETOSPHERIC SPECIFICATION MODEL

2.0. Introduction

This scientific description is intended to provide an overview of the MSM. More detail on certain topics, particularly regarding the detailed operation of the MSM, can be found in other sections of this report and especially in the Appendix.

2.0.1. Goals and Objectives

The goals of the MSM were the following:

- (i). It should produce the most accurate and reliable specifications possible, given the available input parameters, the state of magnetospheric science, and the personnel and computing facilities available to the Air Weather Service.
- (ii). It should provide a limited capability for forecasting, specifically upper- and lower-limit forecasts.
- (iii). It should have a flexible modular structure, to allow for future substitution of new and improved routines.
- (iv). It should be comprehensive enough to be capable, with minor alterations, of specifying a wider range of physical parameters than is now required.
- (v). It should have as much theoretical consistency as possible, given the constraints listed under item 1.

The basic objective of the MSM is to specify certain magnetospheric parameters based on real-time input data that is expected to be available to the Space Forecast Center. The major physical parameters calculated by the MSM include the following:

(i). Magnetospheric Particle Fluxes.

1-100 keV Electrons at Synchronous Orbit. Calculation of these fluxes was the primary objective for the MSM. Test data were made available to us, and model predictions have been extensively checked against these test data, as discussed in sections 3 and 4.

Electrons and Ions at $L \approx 2$ to 10, Energies $100 \text{ eV} < E < 100 \text{ keV}$. Calculation of these particle fluxes constituted a secondary objective for the MSM. The model calculates these fluxes, but very little data have been available to allow testing of model accuracy.

Electrons and Ions with $E > 100 \text{ keV}$. For electrons between 100 and 300 keV, the MSM estimates fluxes by a simple algorithm that is based on observed geosynchronous fluxes. For electrons above 3 MeV, the Koons-Gorney model is available and will be installed shortly.

(ii). Energy Fluxes and Average Energies of Precipitating Electrons and Ions. These parameters are specified by the MSM and are thus available for use by the ionospheric model, if needed. Comparison of predicted electron precipitation against data for April 21-23, 1988 is discussed in Section 3. The statistical electron-precipitation model of [Hardy,

1985 #1]. Because of the lack of real-time data for testing of a full ion-precipitation algorithm, the MSM is set to use the statistical ion-precipitation algorithm of [Hardy, 1989 #2].

(iii). Ionospheric Electric Fields. The ionospheric potential distribution is provided for possible use by the ionosphere model, if needed.

(iv). Magnetospheric E- and B-Fields. These fields must be computed by the MSM as part of its overall modeling of the magnetosphere. The B-field model is directly used by the application program *MAPINT* to map fluxes from the equatorial plane to an arbitrary point on a field line.

2.0.2. Logical Structure of the MSM.

The overall logical structure of the MSM is diagrammed in Figure 2.1, and the basic organizational structure of the present section is based on the figure. Figure 2.2 illustrates the major subroutines and provides a more detailed flow chart of the MSM. The basic input data required for the full model run are read from the Environmental Database and are subjected to interpolation operations (described in Section 2.1.1). In most cases, the input data stream, suitably interpolated, still does not directly specify all of the input parameters required by the MSM. The input data is therefore fed into a set of front-end models, which utilizes whatever data are available to estimate the remaining parameters that are required by the central routines of the MSM (Section 2.2). Next the matrices describing the essential characteristics of the magnetic field are computed for mark-time during the period to be modeled. (Fifteen-minute intervals have been used in our tests.) The magnetic-field model, which represents the most complex element of the MSM, is described briefly in Section 2.3, and fully in Appendix f, which is Robert Hilmer's Ph.D. thesis. After the completion of the computation of the magnetic-field matrices for the modeled period, the program computes a single matrix that specifies the electrostatic potential at every grid point, for each mark-time during the event. The electric-field model is described in Section 2.4.

2.1 Input Data from the Environmental Database

The MSM uses real-time data from a variety of sources to establish initial and boundary conditions for the particle distribution functions, and to establish input parameters for the E- and B-field models. These data are retrieved from the environmental database through a subroutine called *INDATA* (see figure 2.2). *INDATA* is called by the MSM to access the input data files but *INDATA* must be written by the contractor preparing the environmental database. (Note: In the version of MSM delivered with this report, *INDATA* exists as a stub to access the test datasets delivered with the model.) As input data are brought in they are tested for gaps in a subroutine called *PARGEN*. If data are missing from a given input parameter for a time gap in excess of a certain time, "front-end" models are used to generate substitute values for the missing data values. The front-end models rely on empirical algorithms described in section 2.1.3. The data are also interpolated to obtain values at the model step times. This interpolation is described in section 2.1.2.

In addition to the data brought in through *INDATA*, that are used as input to the models primary calculations, the MSM also uses geostationary satellite particle flux data to provide a comparison with the model output.

2.1.0. MSM Input Parameters

The MSM requires seven basic input parameters, plus two sets of geostationary particle data for estimates of errors in the model output. These parameters, together with their applications in the MSM their variable names and units are as follows:

Input Parameters Used by the MSM

Table 2.1

Input parameter and use	Name	Unit
Kp (Used for initial and boundary fluxes)	FKP	NONE
Dst (Determines ring current strength in B-field model)	DST	NANOTESLA
LOW LAT BOUNDARY OF THE AURORA (Determines auroral zone boundary in E-field model and is used to constrain the B-field mapping)	DLATAZ	DEGREES
POLAR CAP POTENTIAL (Input to E-field model)	PCP	KILOVOLTS
POLAR CAP POTENTIAL PATTERN (Input to E-field model)	XIPATT	NONE
SOLAR WIND VELOCITY (Determines standoff distance in B-field model)	SWVEL	Km/s
SOLAR WIND DENSITY (Determines standoff distance in B-field model)	SWDEN	PROT/CM ³
GEO ELECTRON FLUX (Used to check model predictions) *	EPSAT1	ELEC/CM ² -S-Sr-Kev
GEO ION FLUX (Used to check model predictions) *	EPIONS	IONS/CM ² -S-SrKev

* - Not loaded by calls to *INDATA*.

The low latitude boundary of the aurora is determined from the electron precipitation data from the DMSP satellites through an algorithm developed by the Geophysics Laboratory. The boundary position is adjusted for midnight magnetic local time using the algorithm published by Gussenhoven et al.[1983].

The polar cap potential drop is derived from DMSP ion drift meter data by an algorithm developed at the University of Texas at Dallas by Rod Heelis and Marc Hairston.

The polar cap potential pattern type is from Maynard - Heppner as digitized by Fred Rich. Three patterns are possible. The choice of type is determined by an algorithm provided by the University of Texas at Dallas group. For the tests run to date, only two pattern types have been required. These are representative of the IMF conditions B_z south and north.

Solar wind data is intended to be from a solar wind monitor. For our tests this data was derived from the NSSDC OMNI dataset [King,1989].

The GEO electron and ion fluxes are obtained from geostationary satellites whenever possible and are read by the MSM differently from the rest of the parameters.

Kp and Dst are provided by the Air Force and NOAA.

2.1.0.1. Parameters Called by INDATA

Each input parameter (except the GEO electron and ion fluxes) is loaded separately by calling *INDATA*. The form of the call to *INDATA* is: CALL INDATA(param-name,STARTT,ENDT,NDIM,DARRY,NUMNUM)

The arguments of the call have the following meanings:

param-name is a valid parameter name from the MSM input parameter list.

STARTT is the starting time for the current data request.

ENDT is the ending time for the current data request.

NDIM is the maximum number of input parameter values that may be returned and the horizontal dimension of the data array, DARRY.

DARRY is the two dimensional array to be retrieved from the environmental database. The size of DARRY will be NDIM by 8.

NUMNUM is the number of data values placed in DARRY by *INDATA*.

The format consists of an eight-word record as follows:

Word 1 = data value at t

Word 2 = year at t (full year required eg. 1990)

Word 3 = decimal day at t

Word 4 = spacecraft geomagnetic latitude at t

Word 5 = spacecraft geomagnetic longitude at t

Word 6 = spacecraft altitude at t

Word 7 = magnetic local time at t

Word 8 = data error quality value at t

where t represents the time tag for the data value, ie. words 2 and 3 and data values are expected one after the other in time-sequential order with a complete block of all available data making up one call to *INDATA*.

The last five words are ignored in the present version of the MSM.

Data words not used or empty are represented by -999.

All parameters are assumed to be single precision, floating point numbers.

2.1.0.2. The GEO Satellite Particle Data

The electron and ion flux data from geostationary satellites are not used to set model conditions and they must be formatted with greater flexibility because of the variability of detector energy channels available and the possibility of further changes in detector suites in the future. Therefore, these data are not handled in the same manner as the other seven input data parameters. They are instead called directly as files with the the following format:

Header record:

Number of energy channels in the following data record	Year (eg. 1988)	Decimal day (eg. 112.500 =noon, April 21 in leap yr)	Geographic latitude of satellite (degrees)	Geographic longitude of satellite (degrees-east)	Altitude of satellite (Km)	Magnetic local time of the satellite (HrMin.)
--	-----------------	--	--	--	----------------------------	---

Data record:

Low end of energy channel 1 (KeV)	High end of energy channel 1 (KeV)	Log10 Flux (No./cm ² -S-Sr-KeV) channel 1	1 sigma error in Flux channel 1	Species (-1=electrons, 1=ions)
Low end of energy channel 2 (KeV)	High end of energy channel 2 (KeV)	Log10 Flux (No./cm ² -S-Sr-KeV) channel 2	1 sigma error in Flux channel 2	Species (-1=electrons, 1=ions)
-----	-----	-----	-----	-----
-----	-----	-----	-----	-----
-----	-----	-----	-----	-----
Low end of energy channel n (KeV)	High end of energy channel n (KeV)	Log10 Flux (No./cm ² -S-Sr-KeV) channel n	1 sigma error in Flux channel n	Species (-1=electrons, 1=ions)

All variable are assumed to be single precision floating point numbers.

Data words not used or empty are represented by -999.

Data from different satellites may be interleaved but are assumed to be time sequential.

2.1.1. Input Parameter Interpolation

Input data values have time tags that not generally simultaneous with the time steps for a given model run. (The model nominal time step is a 15 minute interval beginning with the model start time.) Since input data values are required at each model time step, a linear interpolation is performed between nearest neighbor data values. Several methods of smoothing the data were examined and rejected because they resulted in a loss of time resolution or, in the case of spline fits, caused unrealistic overshoot (see Quarterly Status Report no. 10. The required interpolation occurs in the subroutines *DNTTRP* and *DTXIPT*.

At same time that the interpolation takes place, a time gap sensing routine determines data gaps between the required model time step time and the nearest available data time. This is done so that significant data gaps can be filled by proxy values for the input parameters. These proxy "values" are determined by the Front-end models. The maximum allowable time gap before proxy values are used was determined separately for each

parameter by a statistical study. In this study, for a run of data from April 21-23, 1988, an increasing number of data points were intentionally deleted and replaced by linear interpolations and the RMS error computed after each new deletion. Proxy data values were then inserted in place of the interpolations and the RMS error computed again. At each point, the two RMS errors were compared. When the RMS error obtained with proxy values inserted became lower than that for no data values but with interpolations, the maximum time gap was considered to be established.

2.2. Front-end Models and Default Models

An important constraint placed on the MSM, early in the program, was that it must "fail gracefully". This meant that the model must maintain its accuracy and validity in the event of loss of some or even all of the input data parameters, except Kp. In order to meet this constraint, two strategies were devised.

The first strategy was the development of Front-end models which provide values for the input data parameters if one of the values were missing from the input data stream, either intermittently or for a long period. A separate Front-end model is required for each input data parameter and in some cases several backup models are required.

The second strategy involved the use of so-called "Default" models to completely replace the MSM computed flux output if the only remaining input data parameter is Kp.

2.2.1. Front-end Models

As indicated above, data gaps in the real-time input parameters must be filled with proxy values. Front-end models which rely on other parameters present in the data stream were developed to provide these values. In one case, the parameter required by the model itself is a secondary parameter derived from the input parameters, solar wind velocity and solar wind density. This parameter is the standoff distance.

Since it was anticipated that the Front-end models would be primarily empirically based and would probably be dependent on Kp, Dst, or similar geophysical parameters, the first step was an extensive literature search to look for paper relating various parameters. This search was conducted by Robert Hilmer and took a one month. The search netted 131 papers. These are listed in the Appendix as the MSM Reference List: Correlation Studies. The papers were arranged in a matrix format such that all papers relating any two parameters could be quickly identified. This matrix is also reproduced in the Appendix.

Next, algorithms were developed which made use of the relationships found in the literature. In one case, published relationships were put together to yield a new relationship between the low latitude boundary of the aurora and the inner edge of the plasma sheet. In another case, a new empirical relationship was established between Kp and Dst. Development of these Front-end model algorithms is discussed in detail in Quarterly Status Reports nos. 3, 9, and 10.

The following table indicates the sources of the input parameter values and references to additional input values required by the MSM:

Table 2.2

FRONT END MODEL INPUT PARAMETER SOURCES

PARAMETER	USED IN	METHOD OF DETERMINATION (in order of priority)
Dst	B-field	1. Ground magnetometers 2. $Dst = -355 + 5.25 * DLATAZ$ 3. $Dst = -Kp^4$ for $Kp < 4$: $Dst = -20 - ((Kp * 10) - 40) * 2.6$ for $Kp > 4$ 4. Persistence if less than 6 hours
Low latitude boundary of the aurora	B-field	1. DMSP or NOAA satellite data 2. $DLATAZ = 66.95 - 2.03 * Kp$ (Gussenhoven et al., 1983)
Polar-cap potential drop	E-field	1. Ion drift data from DMSP (Heelis and Hairston). 2. $PCP(Kv) = 14.587 + 1.7 * (Kp * 10)$ (Reiff, Private comm.)
Polar-cap pattern type	E-field	1. Ion drift data from DMSP (Heelis and Hairston) 2. Default: assume pattern #1
Standoff Dist. (replaces SWVEL & SWDEN if missing)	B-field	1. If solar wind parameters are available, then: $R_s = [(f B_o^2) / (2 \pi \rho_o V_o^2)]^{1/6}$, where $f=1.35$, B_o =surf. field at the equator, ρ_o =S.W. mass density, and V_o = the S.W. velocity, otherwise: 2. $R_s = 11.7 / Kp$, but, $R_s \geq 6 R_e$ at all times
Inner edge of plasma sheet at midnight in equatorial plane	B-field	See section 2.3
Poleward edge of model region	E-field	See section 2.4.2
Poleward edge of field-reversal region	E-field	See section 2.4.2
Boundary p,Ti,Te	Partrac	See section 2.5
Initial p,Ti,Te	Partrac	See section 2.5

Notice that the lowest priority algorithm is either Kp based or else a fixed default value. This means that the MSM can run on Kp alone.

2.2.2. Default Models

In order to meet the constraint that the MSM produce useful output under conditions when only Kp is available as input data, two Kp based statistical models were incorporated to replace the computed output of the MSM in the event of loss of all input data except Kp. These were the Hardy et al., [1985] model of precipitating electron and ion fluxes in the auroral zone and a model developed by Garrett for the electrons and ions at geostationary orbit.

It was determined, during testing that the MSM run on Kp alone produces better output than the Garrett model, however, the Garrett model has proven useful because it is used to establish the initial conditions for the model in the vicinity of the geostationary orbit. It is probable that the MSM computed auroral precipitation output based on Kp is also better than the Hardy et al. model output, but we have not been able to confirm this since DMSP precipitating particle data had not been made available by the end of the contract. Both the Hardy et al. and Garrett models are average models and therefore contain no intrinsic time dependence other than that derived from the variation in Kp. We also evaluated for possible application, an average auroral precipitation model by Foster et al. [1986]. This model was not used because it is driven by a precipitation power index not readily available.

2.2.2.1. The Hardy et al. Model of Precipitating Auroral Fluxes

The Hardy et al. model is actually two models, one for electrons and one for ions. They are represented in the MSM by the subroutines *AURL1* and *AURL2S* for electrons and ions respectively.

The electron model was published by Hardy et al. [1985] and updated coefficients were provided to us by W. J. McNeil of Radex Inc. and David Hardy of GL. The model employs an Epstein function to model the auroral electron fluxes in latitude and a Fourier series for the local time dependence. The Epstein function has the form

$$e(h) = r + s_1(h - h_0) + (s_2 - s_1) \times \ln \left[\frac{1 - \frac{s_1}{s_2} e^{-(h - h_0)}}{1 - \frac{s_1}{s_2}} \right] \quad (2.2-1)$$

where $e(h)$ is the energy or number flux dependent on the peak flux, r , the latitude, h , the latitude of peak flux, h_0 , and s_1 and s_2 , the slopes on either side of the peak. The Fourier series has the form

$$\alpha(T) = \sum_{n=0}^6 C_n^\alpha \cos\left(\frac{n\pi T}{12}\right) + S_n^\alpha \sin\left(\frac{n\pi T}{12}\right) \quad (2.2-2)$$

where α is the calculated parameter which can be either r , h_0 , s_1 , or s_2 . For each Kp interval, this analytic function requires 52 coefficients represented in the above equation by C and S . These coefficients are embedded in the MSM and can be found in the appendix. The model is used as follows: to determine an energy flux for a given latitude, h , and local time, T , use the Fourier series to determine r , h_0 , s_1 , and s_2 . Then insert these into the Epstein function along with h .

2.2.2.2 The Garrett Model of Geostationary Orbit Fluxes

Garrett et al. [1981a, 1981b] published a statistical analysis of the geostationary orbit electron and ion environment based on data from ATS 5 and 6. Garrett and DeForest [1979] had previously outlined an analytical approach to modeling such average flux values in terms of the moments of the distribution functions. Early in the MSM project it was realized by John Gaudet that this early work formed the nucleus upon which could be built a more substantial characterization of the geostationary fluxes which would be useful to the MSM. Based on this, using additional data from Scatha and P-78, in addition to the ATS 5 and 6 data, Hank Garrett and John Gaudet prepared a new model (or rather set of models) of geostationary electrons and ions for the MSM. Akira Nagai then adapted these for use in the MSM. Generically these are referred to as the Garrett model and they are embedded at numerous places in the MSM subroutines.

The Garrett model uses a Fourier expansion of the diurnal and semi-diurnal local time components and a linear fit to A_p . The fits determine the coefficients of the expansions of the four moments of the distributions functions. These moments are then converted to bi-maxwellian distribution functions which are integrated to provide the fluxes in any required energy passband. The equation for the moments, M_i is

$$\begin{aligned}
 M_i = & C_1 + C_2 \cos\left(\frac{lt \pi}{12}\right) + C_3 \sin\left(\frac{lt \pi}{12}\right) + \\
 & C_4 \cos\left(\frac{lt \pi}{6}\right) + C_5 \sin\left(\frac{lt \pi}{6}\right) + \\
 & A_p \left[C_6 + C_7 \cos\left(\frac{lt \pi}{12}\right) + C_8 \sin\left(\frac{lt \pi}{12}\right) + \right. \\
 & \left. C_9 \cos\left(\frac{lt \pi}{6}\right) + C_{10} \sin\left(\frac{lt \pi}{6}\right) \right]
 \end{aligned}
 \tag{2.2-3}$$

The C_s are the coefficients obtained by Garrett and Gaudet, and lt is the local time. A_p is 8 times the linearized value of K_p times 3. There are eight moments, M_i , number density and number flux and energy density and energy flux for the electrons and ions.

During testing of the Garrett model, it was determined that there were problems with the model predicting unphysically high temperatures at high K_p near midnight. This was solved by restricting K_p to values of 6 or lower when the Garrett Model is used. Also, the Garrett model gives unrealistically low fluxes at higher energies because of the low high-energy tail inherent in the maxwellian distribution.

2.3. The Magnetic-Field Model

2.3.0. Introductory Comments

Over the course of contract F19628-87-K-0001, a completely new magnetic-field model was developed for use in the Magnetospheric Specification Model and the Rice Convection Model. This new magnetic-field model, which constitutes the most complex component of the MSM, represents several years of work by Robert Hilmer, carried out under the supervision of Hannes Voigt. We attempt only a brief summary of this model within the main body of this report. A complete and detailed description is contained in Hilmer's Ph.D. thesis, which is included as Appendix f.

The major goal in this endeavor was a B-field model that would be flexible enough to represent a wide variety of magnetospheric B-field configurations, using input parameters that would be available in the MSM input datastream. The observation-based B-field models that are most commonly used by magnetospheric physicists today are those of *Tsyganenko* [1987,1989] and *Tsyganenko and Usmanov* [1982], but those models, which are solidly based on averaged magnetic-field observations, characterize the state of the magnetosphere by a single parameter Kp . However, the magnetic-field configuration can vary widely for a given value of Kp . The MSM is designed to run from much more detailed real-time observational information than just Kp . Therefore, a magnetic-field model was needed that could respond flexibly to independent variations in several input parameters.

2.3.1. Inputs to the Magnetic-Field Model.

The input parameters used by the MSM's magnetic-field model are the following:

- (i) Magnetopause standoff distance, which is estimated from the solar-wind ρV^2 if solar-wind data are available. Otherwise, the standoff distance is estimated from Kp and a statistical relation. (See Section 2.2.).
- (ii) Dst, which is derived from ground magnetometers stations.
- (iii) Mapping of the equatorward edge of the diffuse aurora at local midnight. The latitude of the equatorward edge is estimated from real-time DMSP electron data, using an algorithm supplied separately by the USAF Geophysics Lab. We have used this direct observational information, along with published statistical information, to place a restriction on the mapping of the field line that connects the equatorward edge of the aurora at local midnight to the inner edge of the plasma sheet. The description presented here supersedes that presented in Section 5.4 of Appendix f. We know of no study based on observational statistics that relates Λ_{mid} , the invariant latitude of the equatorward edge of the diffuse aurora at local midnight, to r_{mid} , the equatorial geocentric distance of the inner edge of the plasma sheet at the same local time. However, statistical studies have related each parameter to Kp . The results of *Gussenhoven et al.* [1983] suggest that

$$\Lambda_{mid} \approx 66.95^\circ - 2.03 Kp \quad (2.3-1)$$

Statistical analysis of the Kp -dependence of r_{mid} is somewhat more difficult. However, we have used the published statistical studies of *Horwitz et al.* [1986] and *Kivelson* [1976] to obtain rough upper- and lower-estimate linear formulas relating r_{mid} to Kp . To get an idea of the relationship between Λ_o and r_{mid} we eliminated Kp between those two formulas and equation (2.3.1). The resulting upper- and lower-estimate formulas for r_{mid} as a function of Λ_{mid} are displayed as *rhigh* and *rlow* in Figure 2.3.1. The data on which those formulas are based came mainly from the geosynchronous-orbit region of the

magnetosphere, and we expect those formulas to lose validity when the equatorward edge is outside the range from 4 to 7 R_E . It is clear, in fact, that the formulas give ridiculous values for $\Lambda_{mid} \leq 48^\circ$. However, it is useful to bear in mind another simple approximate relationship between r_{mid} and Λ_{mid} , namely the dipole formula:

$$r_{dipole} = [\cos(\Lambda_{mid})]^{-2} \quad (2.3.2)$$

which is also displayed in the figure. We expect that r_{mid} will always exceed r_{dipole} , because the midnight field is normally expected to be inflated relative to the dipole, but we also suspect that the ratio r_{mid}/r_{dipole} will approach unity when the inner edge comes close to the Earth in times of extremely high activity, because precipitation and charge-exchange loss near the Earth should rapidly reduce the convected plasma-sheet population and inhibit its capability to distend the field lines. Another extreme case with which the MSM will occasionally have to deal is that in which the measured equatorward edge of the aurora is indicated to be at extremely high latitude. It is our understanding that the inner edge of the plasma sheet at local midnight is rarely, if ever, observed to be at $> 10 R_E$ geocentric distance. With all these considerations in mind, we chose for the MSM the following prescription for the mapping of the low-latitude edge of the aurora at local midnight:

$$\frac{r_{mid}}{r_{dipole}} = 1 + 0.25 \left(\frac{r_{dipole}}{5} \right)^2 \quad \text{for } r_{dipole} < 5 \quad (2.3.3a)$$

$$\frac{r_{mid}}{r_{dipole}} = 1.25 \quad \text{for } 5 \leq r_{dipole} < 8 \quad (2.3.3b)$$

$$r_{mid} = 10 \quad \text{for } r_{dipole} \geq 8 \quad (2.3.3c)$$

Equation 2.3.3 does not appear in the main MSM or the MAPINT program anywhere. It was, however, used continually in the generation of the magnetic-field matrices at Rice. It is described here, since it represents a significant approximation that should be borne in mind when the MSM is used.

(iv) (Collapse). The Hilmer-Voigt model includes a feature that allows collapse of the midnight region of the magnetotail, as apparently occurs in the expansion phase of a magnetospheric substorm. Although this is an interesting feature from a scientific viewpoint, we are not utilizing it in the present version of the MSM, because we have not found an automatic algorithm for deducing substorm-associated tail-field collapse in the data stream that is expected to be routinely available for MSM operations.

(v) (Dipole tilt). The Hilmer-Voigt model allows the Earth's magnetic dipole to be tilted away from the nominal direction perpendicular to the solar-wind velocity vector. However, the way in which the magnetic-field model has had to be incorporated within the MSM -- in terms of pre-computed matrices -- has precluded using this basic feature of the B-field model.

2.3.2. Pre-Computed Magnetic-Field Matrices.

The computing facilities that are now expected to be available for routine operation of the MSM preclude real-time computation of magnetic-field models. Therefore, we have precomputed a super-grid of magnetic-field models, in which each model is characterized by the following three parameters:

- (i) Magnetopause standoff distance (6, 8, 10, 12, and 14 R_E).
- (ii) Dst (-400, -300, -200, -150, -100, -50, 0, and 50 nT).

(iii) Equatorward edge of the diffuse aurora at local midnight (16 latitudes from 49.5° to 69.3°).

Each B-field model in this supergrid is characterized by five matrices: *XMIN*, *YMIN*, and *ZMIN*, which specify the location of the "equatorial mapping point" of the field line in GSM coordinates, for each point in the fixed ionospheric grid; *BMIN*, the equatorial field strength; and

$$VM = [\int ds/B]^{-2/3} \quad (2.3.4)$$

where the integral extends along a field line, from the southern ionosphere to the northern. The parameter *VM* determines the gradient/curvature drift of the particles. The five matrices provide all necessary magnetic-field information for running the main MSM. We interpolate on the supergrid of matrices to find the five matrices that represent the essential characteristics of the magnetic field at any given time.

It should be remarked that two of the above-mentioned matrices, *ZMIN* and *BMIN*, are not actually used in the present version of the MSM. They are being included to facilitate future enhancement of model capabilities: *ZMIN* will be required if dipole tilt is included in future versions of the model; *BMIN* is included to facilitate explicit computation of drift velocities for particles that mirror near the equatorial plane, should that capability be needed in special cases.

An application program, *MAPINT*, can map from an arbitrary point *P* within the modeled region of the magnetosphere to the equatorial plane or ionosphere, and thus locate point *P* within our grid. This application program is described in Section 3.

The Hilmer-Voigt magnetic field is computed as a superposition of the fields due to five basic currents, as follows:

- (i) The Earth's main field, currently assumed to be a dipole B_d ;
- (ii) B_{rc} , the field due to the ring current;
- (iii) B_{tail} , the field due to the cross-tail current;
- (iv) B_{cf} , the field due to the Chapman-Ferraro currents, which flow of the magnetopause.

The technical details of the Hilmer-Voigt magnetic-field model are described in Appendix f.

2.4. The Electric-Field Model

2.4.0. Introductory Comments.

A new model of the ionospheric electric field was developed for the MSM, a model that was specifically designed to be driven by observational parameters that will be available in real-time for the MSM, specifically the polar-cap potential drop, the polar-cap pattern type, and the equatorward edge of the diffuse aurora at local midnight.

2.4.1. Division of the Ionosphere into Regions.

The essence of the MSM's electric-field model involves dividing the ionosphere up into four different regions as shown in Figure 2.4-1. The four regions, which are treated quite differently, are the following:

Region 0: The polar cap, inside the boundary marked *a* above, which is the poleward boundary of the "electric-field-reversal region";

Region 1: The electric-field-reversal region; within our simplified view, this is coincident with the area occupied by the region-1 Birkeland currents;

Region 2: The region of the main auroral sunward flow; it extends from boundary *b*, which is the equatorward edge of the electric-field reversal region, to boundary *c*, which is the equatorward edge of the shielding layer;

Region 3: The low-latitude region, from *c* to the magnetic equator.

The three boundaries (*a*, *b*, and *c*) are defined to be ellipses, which satisfy the following equation:

$$\frac{(x-DX)^2}{A^2} + \frac{(y-DY)^2}{B^2} = 1 \quad (2.4-1a)$$

where

$$x = \theta \cos(\phi) \quad (2.4-1b)$$

$$y = \theta \sin(\phi) \quad (2.4-1c)$$

where θ is invariant colatitude, and ϕ is magnetic local time (0 at noon, $\pi/2$ at dusk...). We do not make any a priori assumptions about whether *A* or *B* is bigger.

2.4.2. Determination of the Ellipse Parameters *A*, *B*, *DX*, and *DY*.

In the program, the parameters defining the three electric-field ellipses shown in Figure 2.4-1 are defined by the three-component vectors *A*(3), *B*(3), *DX*(3), and *DY*(3). In each case, the first component represents boundary *a*, the polewardmost boundary that lies at the high-latitude edge of the electric-field-reversal region, component 2 represents boundary *b*, which lies at the equatorward edge of the electric-field-reversal region, and component 3 represents boundary *c*, which lies at the equatorward edge of the shielding-layer region.

2.4.2.1. Location of Ellipse 2, i.e., Boundary *b*.

We have chosen to associate this boundary, which in the ionosphere is the equatorward edge of the electric-field-reversal region, with the high-*L* boundary of our main modeling region. Furthermore, we choose the following "reasonable" locations for this boundary in the equatorial plane:

$$r_{noon}^{model\ bound.} = 0.95 r_{standoff} \quad (2.4-2a)$$

$$r_{dawn}^{model\ bound.} = r_{dusk}^{model\ bound.} = 1.40 r_{standoff} \quad (2.4-2b)$$

$$r_{midnight}^{model\ bound.} = 2.00 r_{standoff} \quad (2.4-2c)$$

Specifically, we define $r_{dawn}^{model\ bound.}$ to be the equatorial geocentric distance of a field line that lies at the equatorward edge of the electric-field-reversal region and crosses the conducting layer of the ionosphere at local dawn. It will not cross the equatorial plane exactly at local dawn, of course, due to the tendency of outer-magnetospheric field lines to be swept back antisunward. The parameter $r_{dusk}^{model\ bound.}$ is defined in a similar way.

We have made the physical assumption that the equatorward edge of the electric-field-reversal region of the ionosphere maps to the equatorial locations specified in equation (2.4-2). In fact, it is not clear observationally how far out in the tail the equatorward edge of the electric-field-reversal region maps. Although our choice is sensible, it may not be very accurate.

In any case, we assume that boundary *b* (ellipse 2) is an ellipse in the ionosphere in flat-polar coordinates, and we determine the exact location of that ellipse by using the magnetic-field model to map from the equatorial plane to the ionosphere. Note that the ionospheric location of ellipse 2 is defined by magnetic-field mapping from the equatorial plane, not from a measured boundary.

Our magnetic-field-model-based algorithm for locating ellipse 2 was chosen for two practical reasons:

- (i) The input data stream that is presently expected to be available for operational use of the MSM does not include the location of the equatorward edge of the electric-field-reversal region or (roughly equivalently) the equatorward edge of the region-1 Birkeland currents. Routine automatic determination of these boundaries is somewhat difficult.
- (ii) There is always a chance that, for operations in extreme magnetospheric conditions or with sparse or bad input data, our magnetic-field model will be highly inaccurate. If we chose our main modeling boundary from an observed ionospheric boundary, the equatorial map of that boundary might be ridiculous from the viewpoint of particle tracing: either on field lines that extend to unphysically large distances from Earth or field lines that lie inside synchronous orbit. Either of these circumstances would prevent the particle tracer from functioning and would compromise the primary objective of the model. Our conservative algorithm for locating ellipse 2 essentially eliminates the probability of this type of failure.

We have found that our magnetic-field-model-based algorithm for locating boundary *b* sometimes leads to ionospheric-electric-field patterns that are not optimally realistic. We have, therefore, developed an algorithm for post-correcting the ionospheric-electric-field pattern, after the magnetospheric particle traces have all been completed, using the location of the main ionospheric electric-field reversal as additional input information. Since this information is not expected to be included in the data stream that will be routinely available to the MSM, we have not included that correction algorithm in the MSM package. However, it is available on request.

2.4.2.2. Location of Ellipse 3, which is Boundary *c*

To estimate this boundary from the available observations, we make use of its close proximity to the equatorward edge of the diffuse aurora, a boundary that has been studied

extensively. From Figure 6 of the paper by *Gussenhoven et al.* [1983], we estimate that the dawn equatorward edge is about 1° poleward of the midnight equatorward edge, on the average. The duskside equatorward edge lies several degrees further poleward. However, we expect the electric-field boundary to lie equatorward of the boundary of the electron precipitation, because ions, which do most of the shielding, penetrate better on the dusk side. Therefore, for the purpose of setting the equatorward boundary of the sunward-flow region, we choose the equatorward edge at dusk also to be 1° poleward of the midnight equatorward edge, *i.e.*,

$$\Lambda_{dawn}^{eq.edge} = \Lambda_{dusk}^{eq.edge} = \Lambda_{midnight}^{eq.edge} + 1^\circ \quad (2.4-3)$$

Table 2 of *Gussenhoven et al.* (1983) gives straight-line *Kp* fits to the noon and midnight equatorward edges, and we use those to estimate the noon-midnight difference. We define "noon" to be the average between 1100-1200 and 1200-1300, and "midnight" to be the average between 2300-2400 and 0000-0100. We eliminate *Kp* from the fit formulas and write the noon equatorward edge simply as a function of the midnight equatorward edge. The resulting formula is

$$\Lambda_{noon}^{eq.edge} = \Lambda_{midnight}^{eq.edge} + \frac{(66.95 - \Lambda_{midnight}^{eq.edge}) \times 7.725 + (\Lambda_{midnight}^{eq.edge} - 56.8) \times 2.80}{10.15} \quad (2.4-4)$$

Simply combining (2.4-1)-(2.4-4) does not offer a positive guarantee that ellipse 2 lies poleward of ellipse 3, since ellipse 2 is derived from the magnetic-field model and ellipse 3 is derived from real-time data and statistical rules. On the other hand, the electric-field model will do something ridiculous if ellipse 3 slips poleward of ellipse 2. Ridiculous results are also guaranteed if the two boundaries get unphysically close to each other. Therefore, we enforce minimum thicknesses for region 2, for noon, dawn, dusk, and midnight. First, we set some (arbitrary) input parameters, namely

$$\Delta \Lambda_{noon}^{min} = \Delta \Lambda_{midnight}^{min} = 3.0^\circ \quad (2.4-5)$$

$$\Delta \Lambda_{dusk}^{min} = \Delta \Lambda_{dawn}^{min} = \frac{4.5 \times 10^{-6} PCP}{E_{max}} \quad (2.4-6a)$$

where *PCP* is the polar-cap potential drop in volts, and E_{max} , the maximum allowable value of the average dawnward electric field across region 2 at dawn or dusk, is given (arbitrarily) by

$$E_{max} = 0.1 \text{ V/m} \quad (2.4-6b)$$

We now define

$$\delta_i = \Lambda_i^{mod.bound.} - \Delta \Lambda_i^{min.} - \Lambda_i^{eq.edge} \quad (2.4-7)$$

for *i* = noon, dawn, dusk, and midnight. In each case, if $\delta_i < 0$, we then set

$$\Lambda_i^{eq.edge} \rightarrow \Lambda_i^{eq.edge} + \delta_i \quad (2.4-8)$$

2.4.2.3. Calculation of A , B , DX , DY for Ellipses 2 and 3.

Having thus located the latitudes at which ellipses 2 and 3 cross the noon, dusk, midnight, and dawn meridians, we have the information needed to calculate the parameters A , B , DX , and DY for those ellipses. The formulas used are the following:

$$DX(L) = -\frac{1}{2}[\Lambda_{noon}^L - \Lambda_{midnight}^L] \quad (2.4-9a)$$

$$DY(L) = -\frac{1}{2}[\Lambda_{dusk}^L - \Lambda_{dawn}^L] \quad (2.4-9b)$$

$$X^L = \frac{1}{2}[180^\circ - \Lambda_{noon}^L - \Lambda_{midnight}^L] \quad (2.4-10a)$$

$$Y^L = \frac{1}{2}[180^\circ - \Lambda_{dawn}^L - \Lambda_{dusk}^L] \quad (2.4-10b)$$

$$A(L) = \sqrt{\frac{(X^L)^2 (Y^L)^2 - [DX(L)]^2 [DY(L)]^2}{(Y^L)^2 - [DY(L)]^2}} \quad (2.4-11a)$$

$$B(L) = \sqrt{\frac{(X^L)^2 (Y^L)^2 - [DX(L)]^2 [DY(L)]^2}{(X^L)^2 - [DX(L)]^2}} \quad (2.4-11b)$$

2.4.2.4. Calculation of A , B , DX , DY for Ellipse 1.

As discussed in section 2.4.3, our treatment of the potential distribution in the region poleward of our main modeling region is based on a computerized version *Rich and Maynard* [1989] of the *Heppner and Maynard* [1987] empirical model of the ionospheric potential distribution. To utilize that model within our formalism, we had to draw ellipses on each of the seven Heppner-Maynard-Rich patterns that correspond to our ellipses 1 and 2. From those ellipses, the drawing of which involved some subjectivity, we derived parameters A , B , DX , and DY , which we label, in the program *AHM*, *BHM*, *DXHM*, and *DYHM*. These parameters, which are given in Table 2.4-1, have two indices, the first indicating ellipse number, and the second, which is called *IPATT*, running from 1 to 7 and indicating the Heppner-Maynard-Rich patterns. These Heppner-Maynard-Rich patterns are scaled to fit into our model polar cap, as discussed in Section 2.4.3. We estimate the width of the electric-field-reversal by assuming that that width scales in the same way as the entire polar cap does. The resulting formulas for calculating the parameters for ellipse #1 are as follows

$$A(1) = A(2) * \frac{AHM(1, IPATT)}{AHM(2, IPATT)} \quad (2.4-12a)$$

$$B(1) = B(2) * \frac{BHM(1, IPATT)}{BHM(2, IPATT)} \quad (2.4-12b)$$

$$DX(1) = DX(2) + \frac{A(2)}{AHM(2, IPATT)} [DXHM(1, IPATT) - DXHM(2, IPATT)] \quad (2.4-12c)$$

$$DY(1) = DY(2) + \frac{B(2)}{BHM(2, IPATT)} [DYHM(1, IPATT) - DYHM(2, IPATT)] \quad (2.4-12d)$$

Table 2.4-1. Heppner-Maynard Ellipse Parameters

Ellipse	IPATT	AHM	BHM	DXHM	DYHM
1	1	17.45	14.26	-2.66	1.60
1	2	12.13	13.78	-5.53	0.80
1	3	16.06	14.31	-3.19	1.12
1	4	13.72	13.78	-0.11	0.05
1	5	14.79	14.73	-2.45	0.48
1	6	12.82	11.70	-1.65	3.40
1	7	15.00	12.07	-2.23	1.22
2	1	20.00	16.97	-3.30	1.33
2	2	16.17	16.70	-7.45	0.32
2	3	18.88	17.07	-4.10	1.54
2	4	19.31	17.23	-1.76	0.85
2	5	18.30	17.93	-2.77	0.69
2	6	16.60	17.50	-2.98	1.86
2	7	17.93	16.60	-3.14	0.21

2.4.3. Potential in Region 0 (Polar Cap).

We directly used the subroutine *EPOT* that was kindly supplied by F. J. Rich for this region. The mathematical techniques used in that subroutine were described by *Rich and Maynard* [1989], and will not be discussed here. We just describe here our procedure for scaling and sliding the Heppner-Maynard-Rich patterns.

Suppose that the H-M-R model implies that boundary *a* satisfies the equation

$$\frac{(x_{HM} - DXHM)^2}{A_{HM}^2} + \frac{(y_{HM} - DYHM)^2}{B_{HM}^2} = 1 \quad (2.4.13)$$

and our real-time observational data indicate that boundary *a* should satisfy

$$\frac{(x - DX)^2}{A^2} + \frac{(y - DY)^2}{B^2} = 1 \quad (2.4.14)$$

Here x_{HM} , y_{HM} , x , y are related to the corresponding colatitude θ and local time ϕ by relations like (1b) and (1c). We define the "rule of corresponding points" to be

$$\frac{x_{HM} - DX_{HM}}{A_{HM}} = \frac{x - DX}{A} \quad (2.4.15a)$$

$$\frac{y_{HM} - DY_{HM}}{B_{HM}} = \frac{y - DY}{B} \quad (2.4.15b)$$

At the beginning of our modified version of the Heppner-Maynard-Rich subroutine (called EPOT), we do a change of coordinates. Given the x and y for which we would like to compute a potential, we use equation (2.4.15) to compute corresponding x_{HM} and y_{HM} values for the corresponding points in the Heppner-Maynard-Rich pattern. From x_{HM} and y_{HM} , we compute the corrected geomagnetic latitude and local time of the corresponding point in the H-M-R pattern, and we use those values in the main H-M-R calculation. We then use the original EPOT algorithm to calculate the potential V_{HM} at point (x_{HM}, y_{HM}) . A final scaling process scales the potentials themselves for consistency with the polar-cap potential drop PCP that has been estimated on the basis of real-time input data:

$$V = V_{HM} \left[\frac{PCP}{VMAX(IPATT) - VMIN(IPATT)} \right] \quad (2.4.16)$$

where $VMAX$ and $VMIN$ are the maximum and minimum potential values in the Heppner-Maynard-Rich pattern for the relevant pattern. The values of $VMAX$ and $VMIN$, which we read off matrices representing the Heppner-Maynard patterns, are given in Table 2.4-2.

Table 2.4-2. Maximum and Minimum Potentials in the Heppner-Maynard-Rich Patterns

<i>IPATT</i>	<i>VMAX</i>	<i>VMIN</i>
1	34007	-42280
2	55354	-16003
3	14390	-60935
4	11287	-16250
5	9329	-12947
6	13249	-14428
7	13221	-13460

2.4.4. Potential in Region 3 (Middle and Low Latitudes).

2.4.4.0. Introductory Comments

A full and realistic model of the subauroral electric field would include two components: the quiet-time field and the disturbance field. The standard representation of the quiet-time field is an observational model developed by *Richmond et al.* [1980], based on quiet-time-average incoherent-backscatter-radar data. We have not included this quiet-time electric-field distribution, because, being a static field, it has essentially no effect on the transport of magnetospheric particles, which is our primary objective.

2.4.4.1. General Expression for the Low-Latitude Potential.

The disturbance field, on the other hand, has an important effect on the transport of magnetospheric particles, and must be included in the MSM. Unfortunately, the disturbance field is not really very well determined or understood at this point, and we expect this to be a major focus of research in the next few years, research involving collaborations between thermosphere and ionosphere modelers and our group. At the present time, we think that we probably have a reasonable idea of the electric-field patterns corresponding to prompt penetration of magnetospheric effects to low latitudes [Spiro *et al.*, 1988]. Those patterns can be roughly parametrized as follows:

$$V_{p3}(\theta, \phi) = \langle V(t) \rangle + F(t) \sin^{-p}(\theta) \sum_{m=0}^{\infty} [a_m \sin(m\phi) + b_m \cos(m\phi)] \quad (2.4-17)$$

where $F(t)$ represents the overall strength of the electric-field penetration at time t .

To estimate the a_m 's and b_m 's, we utilized a least-squares-fit procedure to match the equatorial electric fields from a run carried out with the Rice Convection Model, specifically run 3 from the paper of Spiro *et al.* [1988]. The result was

$$E_{\phi}\left(\frac{\pi}{2}, \phi\right) = 0.5249 \cos(\phi) - 0.0265 \cos(2\phi) - 0.0541 \cos(3\phi) + \\ + 0.0939 \sin(\phi) - 0.2883 \sin(2\phi) + 0.0810 \sin(3\phi) \quad (2.4-18)$$

where the eastward electric field E_{ϕ} is in mV/m, and ϕ is our usual local-time angle, 0 at noon, etc. The maximum westward electric field implied by (2.4-18) is 0.86 mV/m. Pulling the maximum westward electric field out of the formula gives

$$E_{\phi} = E_{west,max} [0.6103 \cos(\phi) - 0.0308 \cos(2\phi) - 0.0629 \cos(3\phi) + \\ + 0.1092 \sin(\phi) - 0.3352 \sin(2\phi) + 0.0942 \sin(3\phi)] \quad (2.4-19)$$

Figure 2.4-2 shows $E_{\phi} / E_{west,max}$ as a function of ϕ , along with the integral

$$\frac{\int_0^{\pi} E_{\phi} d\phi}{E_{west,max}} = 0.6103 \sin(\phi) - 0.0154 \sin(2\phi) - 0.0210 \sin(3\phi) - 0.1092 \cos(\phi) + \\ + 0.1676 \cos(2\phi) - 0.0314 \cos(3\phi) \quad (2.4-20)$$

Note that the normalized electric field is strongest in the region between midnight and dawn, where it is negative (westward). The total variation of the normalized integral, the difference between its maximum and minimum values, is given by

$$\frac{\Delta \left[\int E_{\phi} d\phi \right]}{E_{west,max}} = 1.28 \quad (2.4-21)$$

Expressions (2.4-20) and (2.4-21) are assumed to hold at any latitude equatorward of the shielding layer, because we are assuming separability of the θ and ϕ dependences. Our computed RCM patterns exhibited a rough separability.

The potential along the shielding layer is then given approximately by

$$V_{shield}(\phi) \approx -\sin(\theta_{shield}) R_I \int d\phi' E_{\phi}(\phi') \quad (2.4-22)$$

where θ_{shield} is the colatitude of the shielding layer and R_I is the geocentric distance of the ionosphere (≈ 6500 km).

Substituting (2.4-20) in (2.4-22), and assuming the same power-law dependence on $\sin(\theta)$ as before, we obtain

$$\begin{aligned} V_{low}^k V(\theta_{shield}, \phi) = & -2.75 E_{west,max}^{mV/m}(\theta_{shield}) \left[\frac{\sin(\theta_{shield})}{\sin(25^\circ)} \right] \left[\frac{\sin(\theta_{shield})}{\sin(\theta)} \right]^p \times \\ & \times [0.6103 \sin(\phi) - 0.0154 \sin(2\phi) - 0.0210 \sin(3\phi) - 0.1092 \cos(\phi) + \\ & + 0.1676 \cos(2\phi) - 0.0314 \cos(3\phi)] + VBAR \end{aligned} \quad (2.4-23)$$

Setting $p = 1.38$ gave the best fit to the computed penetration computed in the SUNDIAL RCM runs. In the program, we have neglected the dependence of θ_{shield} on ϕ and let $\theta_{shield} = A(3)-DX(3)$, which is actually appropriate for local midnight.

2.4.4.2. Estimation of $E_{west,max}(\theta_{shield})$.

We use the motion of the equatorward boundary of auroral-zone electron precipitation as an indicator of the direct electrostatic penetration of magnetospheric electric fields through the shielding layer.

Assume that the equatorward edge of the auroral electrons is a convection boundary -- the inner boundary of the plasma-sheet electrons that have recently come in from the tail. Now consider the motion of the ionospheric mapping point of electrons that lie on that boundary. The motion of these boundary-electrons is a combination of gradient/curvature drift (mostly eastward) and $E \times B$ -drift. The latitudinal motion of the ionospheric map of these boundary electrons is, we assume, due predominantly to $E \times B$ -drift that results from the east-west component of the ionospheric electric field:

$$R_I \frac{d\Lambda}{dt} = - \frac{E_{west}}{B_{ir}} \quad (2.4-24)$$

where R_I is the geocentric radius of the ionosphere (6500 km, say), Λ = latitude in radians of the northern-ionosphere crossing point of the boundary, and B_{ir} is the absolute value of the radial component of the magnetic field, also at ionospheric altitude. Setting $B_{ir} = .5 \times 10^{-4}$ T, (2.4-24) can be rewritten as

$$E_{west}^{mV/m} = -1.576 \frac{d\Lambda^\circ}{dt_{hr}} \quad (2.4-25)$$

where Λ° is now latitude in degrees.

If we use (2.4-25) to estimate of the maximum westward electric field at the shielding layer -- specifically, the equatorward edge of the shielding-layer region, we are being sloppy in several respects, notably the following:

1. The electron inner edge is not necessarily at the equatorward edge of the shielding-layer region. On the dusk side, there is frequently a gap between the equatorward edge of the electrons and the equatorward edge of the shielding; this is region of the SAID (Subauroral Ion Drift) events [Spiro *et al.*, 1978]. By equating the electron inner edge with the shielding layer, we are effectively neglecting the potential drop across the rapid-trough-flow region compared to the potential drop along the shielding layer. This error will tend to make us overestimate the penetration effect.
2. If precipitation becomes so strong that the electron equatorward edge is essentially a precipitation boundary, rather than a convection boundary, then (2.4-25) will probably tend to underestimate the penetration electric field.
3. Our procedure assumes implicitly that the meridional motion of the inner edge can be equated to the meridional motion of an individual inner-edge particle; this is valid if the meridional motion occurs on a time scale that is small compared to the particle drift time; otherwise, the particle's equatorward motion, for example, may be limited by the length of time that it is subjected to the nightside westward electric field. In this respect, our simple approximation is best when the plasma-sheet inner edge is moving fast, and penetration is strong. Of course, those are the conditions under which it is important to get a good estimate of the penetration.

Substituting (2.4-26) in (2.4-23) gives an explicit expression for the low-latitude potential. Using the fact that the square-bracketed quantity in (2.4-23) has a total range of 1.28, we find that the total potential drop across the shielding layer (the "penetration potential") is given approximately by

$$V_{wpenet}^{kV} = -13.1 g \frac{d\Lambda^o}{dt_{hr}} \sin(\theta_{shield}) \quad (2.4-26)$$

where θ_{shield} , which is an effective shielding-layer colatitude, is taken to be A(3)-DX(3). Note that V_{penet} is defined to be positive in times of increasing convection, i.e., auroral zone moving equatorward.

2.4.4.3. Estimation of VBAR.

It is well established that there is more sunward flow on the duskside auroral zone, on the average, than on the dawn side. This flow occurs in what we call region 2, plus the sunward-flow part of region 1. Recent work by Lu *et al.* [1989] suggests that ratio

$$\frac{\text{Potential drop across duskside sunward-flow region}}{\text{Potential drop across dawnside sunward-flow region}}$$

is about 1.5, on the average. We choose the value of VBAR, the average potential at low latitudes, such that the ratio of the potential drops, in the auroral zone, is held at a value of 1.5. The potential drop across the auroral zone is approximately $VBAR - 0.38 V_{penet} - V_{min}$ on the dusk side and approximately $V_{max} - VBAR - 0.62 V_{penet}$ on the dawn side. Requiring that the ratio of these two potential drops be 1.5 yields the following expression for VBAR:

$$VBAR = 0.6 V_{max} + 0.4 V_{min} - 0.22 V_{penet} \quad (2.4-27)$$

2.4.5. Potential in Region 2 (Main Sunward Flow Region of the Auroral Ionosphere).

Because the low-latitude field is normally rather weak, but it is crucial to keep appropriate continuity across the shielding layer, we simply add an extra (usually large) auroral-zone field to a smooth extrapolation of the potential used for region 3:

$$V_2(\theta, \phi) = V_{low,x}(\theta, \phi) + V_{az}(\theta, \phi) \quad (2.4-28a)$$

where $V_{low,x}$ is the extrapolation into the auroral zone of the low-latitude potential, and V_{az} is the main potential of the auroral zone. We carry out the smooth extrapolation in the following simple way:

$$V_{low,x}(\theta, \phi) = V_{low}(\theta_c(\phi), \phi) + (\theta - \theta_c) \frac{\partial V_{low}(\theta_c, \phi)}{\partial \theta_c} \quad (2.4-28b)$$

For the main auroral-zone potential, we use the formula

$$V_{az}(\theta, \phi) = V_{b,az}(\phi) \frac{\left[1 - \left\{ 1 + \frac{(\theta_c - \theta)^2}{\Delta \theta^2} \right\}^{-r} \right]}{\left[1 - \left\{ 1 + \frac{(\theta_c - \theta_b)^2}{\Delta \theta^2} \right\}^{-r} \right]} + F_{corr}(\theta, \phi) \quad (2.4-29a)$$

where, in the first term on the right side, $V_{b,az}$ is the auroral-zone contribution to the potential at boundary b , and we choose the exponent r to be equal to unity. In the second term, which is intended to represent the rotation of equipotentials in the Harang-discontinuity region,

$$F_{corr}(\theta, \phi) = -6.75 \frac{dV_{b,az}(\phi)}{d\phi} \phi' \Delta \phi_{amp} \frac{(\theta_c - \theta)^2 (\theta - \theta_b)}{(\theta_c - \theta_b)^3} \quad (2.4-29b)$$

where

$$\begin{aligned} \phi' &= \cos\left(\frac{\pi(\phi - \pi)}{\Delta \phi_{width}}\right) \quad \text{if } \left| \frac{2(\pi - \phi)}{\Delta \phi_{width}} \right| < 1 \\ \phi' &= 0 \quad \text{otherwise} \end{aligned} \quad (2.4-29c)$$

and our present choice for the $\Delta \phi$ coefficients is as follows:

$$\begin{aligned} \Delta \phi_{width} &= 1.0 \\ \Delta \phi_{amp} &= 2.0 \end{aligned} \quad (2.4-29d)$$

We take $r = 1$ and

$$\Delta \theta = (\theta_c - \theta_b) \left[1.25 - 0.75 \cos\left(\phi - \frac{3\pi}{4}\right) \right] \quad (2.4-30)$$

which means that $\Delta \theta = (\theta_c - \theta_b)/2$ for $\phi = .75\pi$ and $\Delta \theta = 2(\theta_c - \theta_b)$ for $\phi = 1.75\pi$.

Figure 2.4-2 shows some typical electric-field curves produced by this functional form. Specifically, the curves shown give meridional electric fields, with the fV_{bmax} factor set equal to unity. Also, ϕ' is set to zero.

2.4.6. Potential in Region 1 (The Electric-Field-Reversal Region).

We treat region 1 as a kind of transition region: we design the potential function for region 1 so that it fits smoothly onto both region 0 and region 2. The procedure is the following:

- (i) Find $\theta_a(\phi)$ and $\theta_b(\phi)$ for the ϕ -value in question;
- (ii) Find $v_0 \equiv V_0[\theta_a(\phi), \phi]$, $v_0' \equiv \partial V_0[\theta, \phi] / \partial \theta |_{\theta_a(\phi)}$, $v_2 \equiv V_2[\theta_b(\phi), \phi]$, and $v_2' \equiv \partial V_2[\theta, \phi] / \partial \theta |_{\theta_b(\phi)}$ using the analytic formulas described for regions 0 and 2;
- (iii) Set

$$V(\theta, \phi) = v_0 + v_0'(\theta - \theta_a) + [3(v_2 - v_0) - (2v_0' + v_2')\delta\theta] \frac{(\theta - \theta_a)^2}{\delta\theta^2} + [2(v_0 - v_2) + (v_0' + v_2')\delta\theta] \frac{(\theta - \theta_a)^3}{\delta\theta^3} \quad (2.4-31)$$

where $\delta\theta \equiv \theta_b(\phi) - \theta_a(\phi)$. This formula makes both V and its derivative continuous at both $\theta_a(\phi)$ and $\theta_b(\phi)$.

2.4.7. Potentials and Electric Fields on the Boundaries.

It is useful to start the potential-calculation procedure by calculating the potentials and their normal derivatives on boundaries a , b , and c , and storing those values, before performing the main potential calculations.

For boundary a , the poleward edge of the electric-field-reversal region, we calculate the potential directly by calling *EPOT*, the subroutine that calculates V in region 0, for latitudes and longitudes on the boundary. To calculate the normal derivative we call the same subroutine a second time, this time for points a latitudinal distance ϵ inside the boundary. The normal derivative is computed by subtracting the two potentials ϵ apart, and dividing by ϵ .

For boundary b , equatorward edge of the electric-field-reversal region, we calculate V by calling *EPOT* again, this time for colatitude θ_b .

For boundary c , the equatorward edge of the shielding layer, we calculate both V and its normal derivative by calling the low-latitude routine, for points on the boundary and also for points a distance ϵ equatorward of boundary c .

This provides sufficient information to completely define the potential in region 2. That procedure guarantees continuity of the potential and its derivative at boundary c , and of the potential at boundary b . By remembering the previously calculated potential on the boundary and calling the region-2 routine for a point ϵ equatorward of boundary b , we establish the normal derivative of V at that boundary.

Since the potential and its normal derivative are now defined at both boundaries a and b , there is sufficient information available for complete determination of the coefficients in the latitude expansion of the expansion in region 1 (equation (2.4-31)).

2.4.8. Numerical Illustrations.

Figures 2.4-3 to 2.4-5 show equipotential diagrams for several cases, one in which the equatorward edge of the auroral zone is not moving and there is thus no penetration to low latitudes (Figure 2.4-3), one in which the equatorward edge is moving equatorward (Figure 2.4-4) and there is consequently a westward electric field across the night side at low latitudes, and one in which the equatorward edge is moving poleward (Figure 2.4-5) and there is an eastward electric field at low latitudes.

2.5. Initial-Condition, Boundary-Condition, and Reference Fluxes

2.5.0. Introductory Comments.

For the purpose of setting boundary and initial conditions for the MSM, and for setting upper and lower limits on the fluxes, we have calculated a flux matrix called *FLXMAT*, which is based loosely on statistical studies and previously published observational data. We first discuss the construction of the *FLXMAT* matrix, then discuss the way in which we use it for initial conditions, etc.

There is a *FLXMAT* matrix for each of three chemical species (electrons, H^+ , O^+). Each of these matrices specifies values of the differential flux ($\text{cm}^{-2} \text{s}^{-1} \text{sr}^{-1} \text{eV}^{-1}$) for seven Kp values (0 to 6), for 29 energy values from 10^1 eV to 10^8 eV in steps of $10^{0.25}$, and for the following four geocentric distances:

- (i) $r = 13$, which is supposed to represent a full-strength plasma sheet.
- (ii) $r = 6.6$, which represents the synchronous-orbit region.
- (iii) $r = 4$, which represents (roughly) the peak of the outer radiation belt.
- (iv) $r = 3$, which represents (roughly) the slot region between the inner and outer belts.

In all cases, the energy dependence of *FLXMAT* is assumed to take the form of a kappa distribution. We begin the discussion by reviewing the properties of the kappa function. The coefficient values assumed for *FLXMAT* for each of the four values of r will then be presented in later sub-sections.

2.5.1. Properties of the Kappa Distribution.

The basic properties of the kappa distribution are as follows (from *Vasyliunas* [1968]):

$$f(v) = \frac{N}{w_o^3} \frac{\Gamma(\kappa+1)}{(\pi\kappa)^{3/2} \Gamma(\kappa-\frac{1}{2})} \frac{1}{\left[1 + \frac{v^2}{\kappa w_o^2}\right]^{\kappa+1}} \quad (2.5-1)$$

where N = number density. The differential flux (particles/area/time/energy/solid angle) is given by

$$j(E) = \frac{N w_o}{2 E_o} \frac{\Gamma(\kappa+1)}{(\pi\kappa)^{3/2} \Gamma(\kappa-\frac{1}{2})} \frac{\left[\frac{E}{E_o}\right]}{\left[1 + \frac{E}{\kappa E_o}\right]^{\kappa+1}} \quad (2.5-2a)$$

where, of course, $E_o = m w_o^2/2$ and $E = m v^2/2$. In program units, the same equation becomes

$$j(E) = (1.68 \times 10^8 \text{ keV}^{-1} \text{ cm}^{-2} \text{ s}^{-1} \text{ ster}^{-1}) F(\kappa) \left[\frac{1 \text{ keV}}{E_o}\right]^{1/2} \left[\frac{N}{1 \text{ cm}^{-3}}\right] \frac{\left[\frac{E}{E_o}\right]}{\left[1 + \frac{E}{\kappa E_o}\right]^{\kappa+1}} \quad (2.5-$$

where

$$F(\kappa) = \frac{\Gamma(\kappa+1)}{\kappa^{3/2} \Gamma(\kappa-\frac{1}{2})} \quad (2.5-2c)$$

The function $F(\kappa)$ is a very slowly varying function of κ ; some values are given in Table 2.5-1 below.

Table 2.5-1. The function $F(\kappa)$.

κ	$F(\kappa)$
2	0.7978846
3	0.86862694
4	0.9027036
5	0.92274588
6	0.9359421
7	0.94528801
8	0.95225411
9	0.95764671

The energy density is given by

$$u = NE_o \frac{3}{2} \frac{\kappa}{\kappa - \frac{3}{2}} \quad (2.5-3a)$$

and, correspondingly,

$$E_o = \frac{2}{3} E^{avg} \frac{\kappa - \frac{3}{2}}{\kappa} \quad (2.5-3b)$$

where E^{avg} is the average energy of a single particle.

2.5.2. Calculation of *FLXMAT* for Electrons.

2.5.2.1. *FLXMAT* for Electrons at $r = 13$.

Our number density and temperature estimates are based on Figure 5 of the paper by *Huang and Frank* [1986]. We choose values consistent with $z = 0$, i.e., as close as possible to the center of the central plasma sheet. We associate $AE < 200$ with $Kp = 1$ and $500 < AE < 1000$ with $Kp = 5$. On this basis, we choose the number density and ion temperature as follows:

$$N_e^{plasma\ sheet} = \frac{0.4(Kp-1) + 0.5(5-Kp)}{4} \quad (2.5-4)$$

$$T_i = \frac{(12\text{ keV})(Kp-1) + (6.5\text{ keV})(5-Kp)}{4} \quad (2.5-5a)$$

According to *Baumjohann et al.* [1989], the ion and electron temperatures are highly correlated, with

$$\frac{T_i}{T_e} \approx 7.8 \quad (2.5-5b)$$

Combining (2.5-5a) and (2.5-5b) and multiplying by 1.5 to convert to average electron energy, we obtain

$$E_e^{avg. plasma sheet} \approx \frac{(2.31 \text{ keV})(Kp-1) + (1.25 \text{ keV})(5-Kp)}{4} \quad (2.5-5c)$$

For the plasma sheet, we use a kappa distribution, with $\kappa = 6$. That distribution uses the energy parameter E_o , which, according to (2.5-3b), is half the average energy. We therefore obtain

$$E_o = (0.2885 \text{ keV})(Kp-1) + (.15625 \text{ keV})(5-Kp) \quad (2.5-5d)$$

The flux is given, in our program units, by substituting (2.5-4) and (2.5-5d) in (2.5-2b). I suggest that we make a general conservative practice of using $Kp = 6$ values for $Kp \geq 6$.

2.5.2.2. FLXMAT for Electrons at $r=6.6$.

We use the sum of two $\kappa = 6$ distributions to represent the situation at synchronous orbit, one for Garrett's low-energy electrons and a second for his high-energy electrons. The values of E_o and number density N are given in the following table. These are local-time averages derived from Garrett's latest model [Garrett and Gaudet, 1989]. The standard reference on this line of research is Garrett et al. [1981].

Table 2.5-2. Garrett-Model Electron Fluxes at Synchronous Orbit

Kp	$N_{e1}(\text{cm}^{-3})$	$T_{e1}(\text{eV})$	$E_{o1}(\text{eV})$	$N_{e2}(\text{cm}^{-3})$	$T_{e2}(\text{eV})$	$E_{o2}(\text{eV})$
0	0.5697	41.382	31.036	0.1826*	6502.9	4877.2*
1	0.6034	54.404	40.803	0.2261	6443.2	4832.4
2	0.6292	64.893	48.670	0.2583	6418.6	4814.0
3	0.7002	95.573	71.680	0.3418	6397.1	4797.8
4	0.8135	148.159	111.119	0.4602	6421.3	4816.0
5	1.0347	256.939	192.704	0.6446	6525.7	4894.3
6	1.4468	456.949	342.712	0.8505	6767.0	5075.2

* These should be overridden by other values. (See following text.)

However, based on the tendency of the Garrett-model to overestimate the >30 keV electron fluxes during quiet times in the April 1988 event, we need to override Garrett's $Kp = 0$ values for N_{e2} , T_{e2} , and E_{o2} . For this purpose, we found, in the literature, seven cases where D. N. Baker and collaborators had published spectral information on 30-300 keV electrons for a well-defined substorm period, including a quiet period before the substorm. The dates and references are given in Table 2.5-3.

Table 2.5-3. Sources of Quiet-Time Data on > 40 keV Geosynchronous Electrons

Date	Figure	Reference
3/22/79	14	[McPherron and Manka, 1985]
9/8/77	1	[Baker et al., 1978]
10/20/82	4	[Baker et al., 1984]
1/26/83	7	[Baker et al., 1984]

2/1/83	7(sp.019)	[Baker et al, 1984]
2/1/83	7(sp.025)	[Baker et al, 1984]
7/29/77	3	[Baker et al, 1982]

(The notations "sp.019" and "sp.025" refer to two different geosynchronous spacecraft, at different local times, observing the same event. The results from the two spacecraft measuring the same event from different locations differed by about as much as the dispersion among the different events, so we counted them as independent measurements.)

Since we seek an observation-based representation of quiet-time fluxes at synchronous orbit, we checked the *Dst* index for each of these times to make sure that none of them occurred during a magnetic storm. Only the last listed event, the CDAW-2 event of 7/29/77, occurred during a magnetic storm. We therefore eliminated the 7/29/77 event from consideration.

In each case, we scaled the flux values from the beginning of the substorm interval plotted, representing the quiet time before the arrival of the substorm fluxes. In some cases, there was a dramatic dropout of fluxes within an hour of the substorm expansion phase: our measured values were always taken well before that dropout. We then averaged the six measured quiet-time log(flux) values and fitted the average to a $\kappa=6$ distribution. The comparison of the averaged data points and the kappa function are displayed in Figure 2.5-1.

The resulting kappa-function parameters, which we use to override the tabulated hot-plasma Garrett values, are as follows:

$$N_{e2}(\text{cm}^{-3}) = 4.926 \times 10^{-3} \quad (2.5-6a)$$

$$E_{o2}(\text{eV}) = 21,000 \quad (2.5-6b)$$

The rationale for overriding Garrett's values with these values, which are derived from >30 keV electron data for pre-substorm conditions, is as follows. We are going to use $Kp=0$ values as a base (equilibrium) level for the trapped radiation. We suspect that Garrett's $Kp=0$ values may have been contaminated somewhat by substorm effects. I should also comment that Garrett's older classic paper on the statistics of geosynchronous electrons [Garrett et al., 1981] indicated a much lower value of N_{e2} for $Kp = 0$ than is indicated in the first line of the preceding Table. However, in overriding the straight Garrett values, we may be sacrificing accuracy in the representation of electrons in the 1-30 keV range to improve accuracy in the > 30 keV range.

2.5.2.3. FLXMAT for Electrons at $r = 3$ and 4.

Fluxes for $r = 3$ and 4 were scaled from Figures 5-45 and 5-46 of *Spjeldvik and Rothwell* [1985], representing the AE7-HI and AE7-LO NASA Radiation Belt Models. We considered four energy channels (40-100 keV, 100-250 keV, 250-500 keV, and 500-750 keV) and averaged the values from the two plots, and then fit the result with a kappa function. Figure 2.5-2 compares the kappa-function fit with the scaled data for both $L = 3$ and 4.

The analytic form of the kappa-function fits are as follows:

$$j^{r=3}(E) = (4.795 \times 10^3 \text{ cm}^{-2} \text{ s}^{-1} \text{ sr}^{-1} \text{ keV}^{-1}) \frac{E_{\text{keV}}}{\left[1 + \frac{E_{\text{keV}}}{65.8}\right]^{3.8}} 10^{[(Kp-2)/6]} \quad (2.5-7a)$$

$$j^{r=4}(E) = (1.106 \times 10^4 \text{ cm}^{-2} \text{ s}^{-1} \text{ sr}^{-1} \text{ keV}^{-1}) \frac{E_{\text{keV}}}{\left[1 + \frac{E_{\text{keV}}}{32}\right]^3} 10^{[(Kp-2)/6]} \quad (2.5-7b)$$

For $L = 3$, this corresponds to $\kappa = 2.8$ and $E_o = 23.5$ keV. For $L = 4$, it corresponds to $\kappa = 2$ and $E_o = 16$ keV.

A remark is needed concerning the assumed Kp -dependence. The NASA Radiation-Belt Models do not contain information on the dependence of the fluxes on the level of magnetic-activity, and, as a result, we have to do something arbitrary. Scanning plots in two old references [Owens and Frank, 1968; VanAllen, 1968], we found that the range of flux variations caused by hour-to-hour variations in magnetic activity is about a factor of 10. Since the average Kp is about 2, the average values that were read off the graphs from the NASA models were taken to correspond to $Kp=2$.

2.5.3. Calculation of *FLXMAT* for H^+ and O^+ Ions.

2.5.3.0. Introductory Comments.

The MSM keeps track of two ion species, H^+ and O^+ , separately, because the two species have substantially different loss rates. We construct two ion *FLXMAT* matrices, one for H^+ and one for O^+ . As in the case of the electron *FLXMAT* matrices, each matrix has elements for seven different Kp -values, 29 different energies, and four different radial distances. However, in the case of ions, we must also seek composition information.

In some cases, we will assume that the two ion species have the same E_o but different densities. We define the ratios

$$r_n = \frac{n_{O^+}}{n_{H^+}} \quad (2.5-8)$$

We thus have

$$n_{H^+} = \frac{N}{1 + r_n} \quad (2.5-9)$$

$$n_{O^+} = \frac{N r_n}{1 + r_n} \quad (2.5-10)$$

2.5.3.1. Calculation of *FLXMAT* for $r = 13$ for Ions.

Our number density and temperature estimates are based on Figure 5 of the paper by Huang and Frank [1986]. We choose values consistent with $z = 0$, i.e., as close as possible to the center of the central plasma sheet. We associate $AE < 200$ with $Kp = 1$ and $500 < AE < 1000$ with $Kp = 5$. On this basis, we choose the number density and ion temperature according to equations (2.5.4) and (2.5.5a). Multiplying by 1.5 to convert to average electron energy, we obtain

$$E^{avg. plasma sheet} \approx \frac{(18 \text{ keV})(Kp-1) + (9.75 \text{ keV})(5-Kp)}{4} \quad (2.5-11)$$

For the plasma sheet, we use a kappa distribution, with $\kappa = 6$. That distribution uses the energy parameter E_o , which, according to (2.5-3b), is half the average energy. We therefore obtain

$$E_o \approx (2.25 \text{ keV})(Kp-1) + (1.21875 \text{ keV})(5-Kp) \quad (2.5-12)$$

From Figure 5 of *Lennartsson and Sharp* [1982], we estimate

$$r_n = \frac{0.6(Kp-1) + 0.06(5-Kp)}{4} \quad \text{for } Kp \geq 1$$

$$r_n = 0.06 \quad \text{for } Kp < 1 \quad (2.5.13)$$

(The low- Kp cutoff is to prevent r_n from going negative.) Figure 6 of *Lennartsson and Sharp* [1984] implies that the average energies for O^+ and H^+ in the plasma sheet are nearly equal, so we can associate $E_o^{H^+}$ and $E_o^{O^+}$ with the E_o value derived in equation (2.5-12).

Figure 2.5-3 shows plasma-sheet H^+ and O^+ fluxes computed according the prescription given in this section.

2.5.3.2. Calculation of FLXMAT for $r = 6.6$ for Ions.

We use the sum of two $\kappa = 6$ distributions to represent the situation at synchronous orbit, one for Garrett's low-energy electrons and a second for his high-energy electrons. The values of E_o and number density N are given in the following table. These are local-time averages derived from the model of *Garrett and Gaudet* [1989].

Table 2.5-3. Garrett-Model Ion-Flux Parameters at Synchronous Orbit

Kp	$N_{i1}(\text{cm}^{-3})$	$T_{i1}(\text{eV})$	$E_{o1}(\text{eV})$	$N_{i2}(\text{cm}^{-3})$	$T_{i2}(\text{eV})$	$E_{o2}(\text{eV})$
0	0.491	120.1	180.2	0.414	16938.5	25408
1	0.519	172.3	258.4	0.411	17891.6	26837
2	0.540	223.6	335.4	0.408	18601.3	27902
3	0.597	403.2	604.8	0.400	20482.0	30723
4	0.687	762.8	1144.2	0.385	23314.8	34972
5	0.853	1543.6	2315.4	0.349	28539.4	42809
6	1.111	2788.3	4182.4	0.290	38108.6	57163

For the low-energy ions (component 1), we base our composition estimates on Figure 5 of *Lennartsson and Sharp* [1982], obtaining

$$r_{n1} = \frac{0.7(Kp-1) + 0.4(5-Kp)}{4} \quad (2.5-14)$$

Since Garrett models fit to a Maxwellian, we take a large value of κ_1 , namely

$$\kappa_1 = 10 \quad (2.5-15)$$

For the high-energy ions (Garrett's component 2), we use the paper by *Gloeckler and Hamilton* [1987]. Table VI of that paper gives values of r_n for "Quiet" and "Disturbed" times, which we associate with $Kp=1$ and 5, respectively. This assumption, combined with the assumption that r_n is linear in Kp , leads to the formula

$$r_n = \frac{0.154 (5-Kp) + 0.767 (Kp-1)}{4} \text{ for } Kp \geq 1$$

$$r_n = 0.154 \text{ for } Kp < 1 \quad (2.5-16)$$

Figure 9 of *Gloeckler and Hamilton* [1987] suggests some noticeable differences between the energy spectra of the H^+ and O^+ ions at $L = 6.6$. However, the differences are fairly subtle, and, for the sake of simplicity, we use the same E_{o2} and κ_2 for both species, specifically the E_{o2} values listed in Table 2.5-3 and

$$\kappa_2 = 4 \quad (2.5-17)$$

The Garrett-model analysis was based on the assumption that all of the observed ions were H^+ . His instrument basically measures energy and flux. The energy measurement is independent of mass, but interpreting the flux in terms of number density and energy involves an assumption about the mass. Interpreting O^+ as being H^+ causes a factor-of-four underestimate in the number density:

$$N_{Garrett} = n_{H^+} + \frac{n_{O^+}}{4} \quad (2.5-18)$$

The actual total number density is then given by

$$N_{total} = N_{Garrett} \left(\frac{1+r_n}{1+\frac{r_n}{4}} \right) \quad (2.5-19)$$

Table 2.5-4. Corrected Garrett Number Densities

Kp	N_1 Garrett	r_{n1}	N_1 corrected	N_2 Garrett	r_{n2}	N_2 corrected
0	0.491	0.325	0.602	0.414	0.154	0.460
1	0.519	0.4	0.661	0.411	0.154	0.457
2	0.54	0.475	0.712	0.408	0.30725	0.495
3	0.597	0.55	0.813	0.4	0.4605	0.524
4	0.687	0.625	0.966	0.385	0.61375	0.539
5	0.853	0.7	1.234	0.349	0.767	0.517
6	1.111	0.775	1.652	0.29	0.92025	0.453

2.5.3.3. Calculation of FLXMAT for $r = 4$ for Ions.

For the radiation belts, we know of no Kp -based statistical study analogous to those of *Garrett and Gaudet* [1989] or *Huang and Frank* [1986]. Our *FLXMAT* consequently has to be based on some individual cases. In each case, we performed a rough digitization of an observed $j(E)$ curve, measuring the fluxes at intervals of $10^{0.25}$. We then fitted a bi-kappa distribution to the resulting curve. Table 4 gives the resulting bi-kappa parameters. Figures 2.5-5 to 2.5-7 compare our fitted curves with the digitized observational ones, for the three Kp levels considered (0, 5+, and 9-). The source for the $Kp=0$ curves was Figure 9 of *Gloeckler and Hamilton* [1987]: that figure represented an average over 12 quiet periods, for $L = 3-5$. The source for the $Kp = 5+$ curve was Figure 12a of *Gloeckler and Hamilton* [1987], which pertained to $L=3.7-4.7$ for a pass during a magnetic storm on September 5, 1984. The Kp value for the time of the pass was 5+. The source for the $Kp = 9-$ period was Figure 8a of *Hamilton et al.* [1988], which pertained to a pass during the very large magnetic storm of February 1986. The pass in question occurred just after the minimum in Dst , and Kp for the interval was 9-.

Table 2.5-5. Bi-kappa Parameters for $r = 4$.

Kp	Species	κ_1	$N_1(\text{cm}^{-3})$	$E_{o1}(\text{keV})$	κ_2	$N_2(\text{cm}^{-3})$	$E_{o2}(\text{keV})$
0	H ⁺	6	0.1	3	10	0.375	200
0	O ⁺	4	0.43	5	-	0	-
5+	H ⁺	10	0.2	15	6	1.9	40
5+	O ⁺	10	0.18	5	6	1.5	20
9-	H ⁺	-	0	-	10	2.3	60
9-	O ⁺	-	0	-	10	5.0	30

Several comments are needed:

1. These curves are all based on data from the CHEM instrument on AMPTE, which apparently had a lower-energy threshold of about 30 keV. O⁺ fluxes were usually not shown even down to 30 keV. One should not place much confidence on *FLXMAT* below 30 keV, since those values are based essentially on extrapolation using the kappa functions.
2. *Gloeckler and Hamilton* [1987] did not show O⁺ fluxes below about 50 keV, although the H⁺ fluxes were shown down to about 5 keV. The "data" shown for O⁺ Figure 3 at for low energies are simply the H⁺ fluxes: I just guessed that the O⁺ and H⁺ fluxes would be about the same.
3. In general, there was considerable non-uniqueness in these fits. Only in the case of the quiet-time H⁺ flux was the fit improved in a major way by the use of two kappa functions rather than one. In a few cases, the fit didn't seem to be improved at all by the second kappa function, and I set the density of one or the other equal to zero. Because of all this arbitrariness in the use of the second kappa function, it would be unwise to do a Kp -interpolation on individual parameters like N_1 , E_{o2} , etc. It would be better to interpolate the $\log(\text{flux})$ values themselves.
4. *Gloeckler and Hamilton* [1987] and *Hamilton et al.* [1988] displayed total energy density vs. r for quiet times and for the specific events that we are using as benchmarks. These observed total particle energy densities covered the energy range from 30-315 keV. We integrated our kappa functions over the same range, and found discrepancies of less than 0.13 in the $\log(\text{base } 10)$, except for the quiet-time fluxes, where the accuracy was lower. The discrepancy in the \log was about 0.23 for quiet-time O⁺ and 0.45 in the case of

quiet-time O^+ , which was the case where a large fraction of their measured data points seemed to represent only a small fraction of the total flux in the range from 30 to 315 keV.

I suggest that *FLXMAT* for $r = 4$ be computed by summing the two kappa functions, for $Kp = 0, 5+$, and $9-$. Values of *FLXMAT* for other values of Kp should be computed by linear interpolation of the logarithms.

2.5.3.4. Calculation of *FLXMAT* for $r = 3$ for Ions.

We could find no published spectra from AMPTE for $r \approx 3$, so that a detailed fitting exercise like that carried out above for $r \approx 4$ is not possible. However, the AMPTE investigators have published curves specifying the r -dependence of the total ion energy density, curves that extend to $r < 3$. Therefore, we use the same table of bi-kappa parameters as was employed for $r = 4$, but with all of the densities scaled to change the energy and number density by the factors suggested by the observational plots. For the $Kp = 0$ and $Kp = 5+$ cases, we checked the corresponding ratios for the number densities; the resulting ratios were nearly the same as the ones derived from the energy-density curves, which implies that the changes in spectral form must not be major. Table 2.5-6 gives those factors.

Table 2.5-6. Ratios of Ion Number Densities at $r = 3$ and 4

Kp	Species	$N(r=3)/N(r=4)$	Source
0	H^+	0.32	Fig. 10, Gloeckler and Hamilton [1987]
0	O^+	0.15	Fig. 10, Gloeckler and Hamilton [1987]
5+	H^+	0.32	Fig. 11, Gloeckler and Hamilton [1987]
5+	O^+	0.10	Fig. 11, Gloeckler and Hamilton [1987]
9-	H^+	2.7	Fig. 7d, Hamilton et al. [1988]
9-	O^+	2.4	Fig. 7d, Hamilton et al. [1988]

Normally, the ion fluxes drop off sharply with decreasing r , inside $r = 4$, as is evident in the first four rows of the table. However, in the case of the great storm of February 1986, the fresh injection of particles extended inside $L = 3$. In most of the main phase, the peak energy density occurred between $L = 2$ and 3. Of course, we are committed to having *FLXMAT* based on $L = 3, 4, 6.6$, and 13, which means that fluxes for $L \leq 3$ are computed by linear extrapolation using the values at 3 and 4. Thus for very large Kp our model would imply that ion fluxes increase all the way in to the Earth, were it not for our policy of using the $Kp = 6$ values for all Kp higher than 6. A consequence of that convention will be that our *FLXMAT* will never represent the fact that, in a very large storm, fresh ring-current ions typically penetrate to $L < 3$.

The following table gives the bi-kappa parameters for $r = 3$.

Table 2.5-7. Bi-kappa Parameters for $r = 3$.

Kp	Species	κ_1	$N_1(\text{cm}^{-3})$	$E_{o1}(\text{keV})$	κ_2	$N_2(\text{cm}^{-3})$	$E_{o2}(\text{keV})$
0	H ⁺	6	0.032	1	10	0.12	200
0	O ⁺	4	0.06	5	-	0	-
5+	H ⁺	10	0.06	15	6	0.6	40
5+	O ⁺	10	0.018	5	6	0.15	20
9-	H ⁺	-	0	-	10	6.3	60
9-	O ⁺	-	0	-	10	11.8	30

2.5.4. Initial-Condition Fluxes

2.5.4.1. Calculation of the value of $FLXMAT$ at grid points.

A primary use of the $FLXMAT(Kp, r, E)$ matrix is in establishing the initial-condition flux at each grid point. Define the symbol $j_{Kp}(I, J, IE)$ to represent the value of $FLXMAT$ that is assigned to a given grid point (I, J) and a given invariant-energy level IE . We calculate $j_{Kp}(I, J, IE)$ using a three-dimensional interpolation, the three dimensions being Kp , r , and E . In each case, a basically linear interpolation is used, but there are a few special features of the interpolation routine that require brief discussion:

- (i) The interpolation on Kp is simple and linear in the log of the flux. $Kp = 2+$ is indicated, in the code, by 2.3333333, 2- by 1.6666667. Also, we use the $Kp = 6$ flux-values for conditions in which the real Kp exceeds 6.
- (ii) The interpolation on r is carried out in log-linear fashion. For $r \leq 4$, we use

$$\log_{10}(j_{Kp}(I, J, IE)) =$$

$$= \frac{\log_{10}\left(\frac{r_u}{3}\right) \times \log_{10}(FLXMAT(Kp, 4, E)) + \log_{10}\left(\frac{4}{r_u}\right) \times \log_{10}(FLXMAT(Kp, 3, E))}{\log_{10}\left(\frac{4}{3}\right)}$$

(2.5-20a)

For $4 < r \leq 6.6$, we use

$$\log_{10}(j_{Kp}(I, J, IE)) =$$

$$= \frac{\log_{10}\left(\frac{r_u}{4}\right) \times \log_{10}(FLXMAT(Kp, 6.6, E)) + \log_{10}\left(\frac{6.6}{r_u}\right) \times \log_{10}(FLXMAT(Kp, 4, E))}{\log_{10}\left(\frac{6.6}{4}\right)}$$

(2.5-20b)

For $6.6 \leq r < 13$, we use

$$\log_{10}(j_{Kp}(I, J, IE)) =$$

$$= \frac{\log_{10}\left(\frac{r_U}{6.6}\right) \times \log_{10}(FLXMAT(Kp, 13, E)) + \log_{10}\left(\frac{13}{r_U}\right) \times \log_{10}(FLXMAT(Kp, 6.6, E))}{\log_{10}\left(\frac{13}{6.6}\right)} \quad (2.5-20c)$$

And for $r \geq 13$, we use

$$\log_{10}(j_{Kp}(I, J, IE)) = \log_{10}(FLXMAT(Kp, 13, E)) + \log_{10}\left(\frac{13}{r_U}\right) \quad (2.5-20d)$$

The latter condition just ensures a reasonable decline of pressure with distance out into the plasma sheet. Specifically, it has the density and pressure declining as $1/r$, with the temperature remaining constant. Considering the present confusion about the variation of temperature with density in the plasma sheet, this seems like a reasonable simple choice.

(iii) Interpolation in energy. The kinetic energy of a particle of species IE at grid point (I, J) is given by

$$E(I, J, IE) = |ALAM(IE)| \times VM(I, J) \quad (2.5-21)$$

where $ALAM$ is called the "energy invariant"; it is defined to be positive for positive ions, negative for electrons. For an isotropic but mono-energetic particle distribution, this energy invariant remains constant as the particles drift along. The energy invariant $ALAM$ is the analogy, for the case of an isotropic plasma distribution, to the magnetic moment μ for the case of a distribution of particles that all have 90° equatorial pitch angle and thus mirror in the equatorial plane. In (2.5-21), VM is the $-2/3$ power of the flux tube volume (equation (2.3-4)). In the MSM, VM has units of $(R_E/nT)^{-2/3}$ and $ALAM$ has units of $eV (R_E/nT)^{2/3}$. For a proof that $ALAM$ is the appropriate invariant for the case of an isotropic plasma, see Harel *et al.* [1981] or Wolf [1983]. The interpolation in energy required to find the flux at energy $E(I, J, IE)$ is done by straightforward linear interpolation using the log of the energy and the log of the flux.

2.5.4.2. Calculation of the Initial Condition Flux

Let $j_o(I, J, IE)$ represent the initial-condition flux at grid point (I, J) and energy channel IE . In general, we calculate this flux from a combination of $FLXMAT$ and a previously calculated set of fluxes for the same time, which we label $j_{old}(I, J, IE)$. Specifically, we write

$$j_o(I, J, IE) = \frac{a_o j_{Kp}(I, J, IE) + b_o j_{old}(I, J, IE)}{a_o f[j_{Kp}(I, J, IE)] + b_o f[j_{old}(I, J, IE)]} \quad (2.5-22)$$

where $f(j) = 1$ if $j > 0$, 0 if $j \leq 0$.

The basic logical structure of the MSM allows use of a general admixture of $FLXMAT$ and j_{old} in setting the initial-condition plasma distribution. However, in its current configuration, the program automatically sets $a_o = 0$ if it has an initial distribution to start from, and $b_o = 0$ when it has no initial distribution to start from.

2.5.4.3. Conversion of Fluxes to Number Invariant η .

It can be shown that, if charged particles $E \times B$ -drift and gradient/curvature drift adiabatically and losslessly, then the number of particles per unit magnetic flux of a given

"species" IE , specifically a given chemical species and given energy invariant $ALAM$, is conserved [Harel *et al.*, 1981; Wolf, 1983]. Therefore, we define $\eta(IE, I, J)$ to be the number of particles per unit magnetic flux of species IE , and do the particle-trace calculations in terms of η rather than the flux j . The expression relating differential flux and η is the following:

$$j_{electron}(I, J, IE) = 7.392 \times 10^{-16} \frac{|ALAM(IE)|^{1/2} \times VM(I, J) \times \eta(IE, I, J)}{|\lambda_{max, IE}| - |\lambda_{min, IE}|} \quad (2.5-23)$$

$$j_{ion}(I, J, IE) = 1.731 \times 10^{-17} \frac{|ALAM(IE)|^{1/2} \times VM(I, J) \times \eta(IE, I, J)}{A^{1/2} [|\lambda_{max, IE}| - |\lambda_{min, IE}|]} \quad (2.5-24)$$

where

$$\lambda_{min, IE} = 0 \text{ for the lowest-energy channel for a given chemical species} \quad (2.5-25a)$$

$$\lambda_{min, IE} = \frac{\lambda_{IE-1} + \lambda_{IE}}{2} \text{ otherwise.} \quad (2.5-25b)$$

Similarly, define

$$\lambda_{max, IE} = 2 \lambda_{IE} - \lambda_{IE-1} \quad (2.5-26a)$$

if K is the highest-energy channel for either electrons or ions, and

$$\lambda_{max, IE} = \frac{\lambda_{IE} + \lambda_{IE+1}}{2} \text{ otherwise.} \quad (2.5-26b)$$

2.5.5. The Boundary-Condition on η .

It is easiest to discuss the boundary condition in terms of the number invariant η rather than the differential flux j . We define $ETABND(J, IE, UT)$ to be the boundary value of η for local-time grid point J , invariant energy channel IE , and time UT . As testing of the MSM progressed, we found that the system performed best if we chose $ETABND$ to be independent of J . In other words, we are assuming that η is constant everywhere on the boundary. Bear in mind that the boundary-condition value of η influences the calculation only for boundary points on which the particles are flowing into the modeling region from the boundary. Assuming η to be a constant on the boundary is a conventional assumption in the modeling of magnetospheric convection. The effects of allowing η to vary on the boundary is a topic of current research interest, but the research results are not yet sufficiently clear to warrant varying η in an operational model like the MSM.

We choose the value of $ETABND$ by the requirement that it correspond to $FLXMAT$ at a point in the equatorial plane that is at local midnight and $13 R_E$ geocentric distance. In choosing $ETABND$ to match $FLXMAT$, we use (2.5-23) or (2.5-24) for the real-time Kp , but for an average value of VM for a $13 R_E$ and local midnight, namely 2.182. We chose to match $ETABND$ at $13 R_E$, rather than a boundary point, because the major observational statistical studies, like that of Huang and Frank [1986], apply to the inner plasma sheet.

This procedure for choosing $ETABND$ has worked well, but the user of the MSM should be aware of a peculiar characteristic of this choice: $ETABND$ remains independent of time for each three-hour Kp interval, then shifts abruptly whenever Kp changes. It

should further be remarked that changes in the boundary value of η do not usually have dramatic effects on fluxes inside synchronous orbit, because of our use of a reference flux, as discussed in the following section.

2.5.6. The Reference Flux.

One of the puzzles of present-day magnetospheric physics is the apparent violation of the adiabatic-convection condition in the inner plasma sheet [Erickson and Wolf, 1980]. The quantity $pV^{5/3}$, which we would expect to be approximate adiabatic invariant, typically increases strongly with increasing distance down the tail. We do not know what physical mechanisms are responsible for the non-constancy of $pV^{5/3}$. (For a discussion of this general topic, see, e.g., Pontius and Wolf [1990].)

For the MSM, which is an operational model, we had to find a way to parametrize around this point on which the physics is not understood. If we assume adiabatic convection from the inner plasma sheet ($\sim 13 R_E$), we obtain fluxes at geosynchronous orbit that are about an order of magnitude larger than indicated by observations. (See Appendix g.)

We take care of the problem by placing a ceiling on the flux values. The computed flux values $j(IE, I, J)$ at all grid points and energy channels are compared with a reference flux $j_{ref}(r(I, J), E(I, J))$. If the computed $j(IE, I, J) > j_{ref}(r(I, J), E(I, J))$, then $j(IE, I, J)$ is set equal to $j_{ref}(r(I, J), E(I, J))$.

To compute the reference flux, we first compute a matrix $j_{max}(r, E)$, defined by

$$j_{max}(r, E) = \max\{FLXMAT(Kp, r, E), Kp=0, 1, \dots, 6\} \quad (2.5-27)$$

The reference flux $j_{ref}(r(I, J), E(I, J))$ is simply set equal to $j_{max}(r(I, J), E(I, J))$, for $r(I, J) \geq 6.6$. For $r < 6.6$, gradient/curvature drift prevents direct earthward transport of plasma-sheet particles, and there is no clear need to invoke a "mystery mechanism" for particle loss inside geosynchronous orbit. Therefore, for $r < 6.6$, we set j_{ref} at a level that would correspond to adiabatic compression of the geosynchronous flux. Since $ds/B \propto r^4$ in a dipole field, and $VM \propto r^{-8/3}$, we write

$$j_{ref}(r, E) = \left(\frac{6.6}{r}\right)^{8/3} j_{max}\left(6.6, E\left(\frac{r}{6.6}\right)^{8/3}\right) \quad (2.5-28)$$

2.5.7. The Minimum Flux.

The loss algorithms employed by the MSM, which are discussed in Section 2.6.3 and 2.6.4, all set the loss rate equal to zero for a given species when the flux level for that species falls below a specified minimum level, which we will call $j_{min}(r, E)$. This minimum flux is defined simply by

$$j_{min}(r, E) = \min\{FLXMAT(Kp, r, E), Kp = 0, 1, \dots, 6\} \quad (2.5-29)$$

2.5.8. The Threshold Flux.

An additional flux matrix, called *THRMAT*, is of the same general form as *FLXMAT* and is calculated along with it. *THRMAT* represents the threshold-flux level for the onset

of strong pitch-angle scattering for electrons. The logic for the calculation of *THRMAT* is described in Section 2.6.3, along with other aspects of the electron loss algorithm.

2.6. Particle Tracer and Loss Algorithms

2.6.1. The Equations of Adiabatic Drift

2.6.1.1. The Differential Equations.

As in most modern efforts at modeling magnetospheric convection, we allow particles to drift perpendicular to \mathbf{B} by $\mathbf{E} \times \mathbf{B}$ drift and gradient/curvature drift. We further assume that particles of a given species IE (i.e., given chemical species and given invariant-energy level), are isotropically distributed with regard to pitch angle. In this case, the formula for bounce-averaged $\mathbf{E} \times \mathbf{B}$ and gradient/curvature drift is

$$\mathbf{v}_{IE} = \frac{\mathbf{E} \times \mathbf{B}}{B^2} + ALAM \frac{\mathbf{B} \times \nabla VM}{B^2} \quad (2.6-1)$$

where $ALAM$ is the energy invariant for an isotropic distribution of particles in adiabatic convection. Our use of $ALAM$ was defined in Section 2.5.4.1 and is discussed in detail by *Harel et al.* [1981] and *Wolf* [1983]. The symbol VM represents the $-2/3$ power of the flux-tube volume, as defined in Section 2.5.4.1.

The assumption that the particle distribution in a collisionless plasma remains isotropic, combined with the assumption that $ALAM$ is conserved, implies that the particles undergo frequent wave-particle interactions that result in pitch-angle scattering, but not in any change in particle energy. It is the best simple theoretical description of the Earth's plasma sheet, which is generally observed to be highly isotropic.

The electric field \mathbf{E} in equation (2.6-1) in general includes both a potential field and an induction field. It can be applied at any point on a field line. Out in the magnetosphere, the magnetic field changes substantially in time, and the induction electric field is generally important. In the ionosphere, however, the changes in \mathbf{B} are small enough to be unimportant from our point of view, and we can write $\mathbf{E} = -\nabla V$, where V is the electrostatic potential. We can then rewrite equation (2.6-1) as

$$\mathbf{v}_{IE} = \frac{\mathbf{B} \times \nabla V_{eff}}{B^2} \quad (2.6-2a)$$

where

$$V_{eff} = V + ALAM \times VM \quad (2.6-2b)$$

It can be shown that, if the particles conserve $ALAM$ and suffer no loss, then η_{IE} , the number of particles of species IE per unit magnetic flux, is conserved along a drift path. We therefore write

$$\frac{D\eta_{IE}}{Dt} \equiv \left(\frac{\partial}{\partial t} + \mathbf{v}_{IE} \cdot \nabla \right) \eta_{IE} = -\text{Loss} \quad (2.6-3)$$

The form of the loss term will be discussed in Sections 2.6.3 and 2.6.4. Equations (2.6-2) and (2.6-3) are the basic equations that the particle tracer solves numerically.

The particle-trace procedure, which is the central part of the MSM, is a useful method of following electrons in the geosynchronous-orbit region, for particle energies below about

100 keV. Electrons below about 100 keV are strongly affected by substorm injections, whereas most variations in the flux above ~ 100 keV are not obviously substorm related. There is an analagous effect in the ions near geosynchronous orbit. The top panel of Figure 2.5-4 suggests that H^+ fluxes below about 30 keV vary considerably with Kp , but more energetic H^+ does not. Oxygen fluxes vary significantly with Kp , but O^+ tends to exhibit considerably smaller flux levels than H^+ for energies above ~ 50 keV.

As delivered, the MSM is set not to perform detailed particle traces for electrons with geosynchronous energies above about 100 keV or for ions with geosynchronous energies above about 50 keV. For energies above those levels, the fluxes outputted by the MSM are computed simply by scaling the appropriate j_{Kp} to agree with the observed geosynchronous fluxes for the previous fifteen minutes.

The decision that the MSM makes on whether it is worthwhile to perform detailed particle traces for particles of a given invariant energy is easy to adjust within the MSM. However, the choice that is presently programmed into the code represents our present best judgement as to the optimum cutoff point for the tracing.

2.6.1.2. The MSM Coordinate Grid.

The MSM's ionospheric grid is equally spaced in local time. The local-time spacing is 7.5° , which corresponds to 0.5 hr of local time. There is a wraparound of 3 grid points, so that $JMAX$, the total number of local-time grid points, is 51.

The latitudinal grid spacing is non-uniform, with the closest spacing in the latitude region that is normally the auroral zone and wider spacing in the polar cap and the low-latitude region. We used the following formula for the latitudinal grid spacing:

$$\frac{d\theta}{dI} = \left[\frac{d\theta}{dI} \right]_{max} + \frac{1}{\pi} \left\{ \left[\frac{d\theta}{dI} \right]_{max} - \left[\frac{d\theta}{dI} \right]_{min} \right\} \left\{ \tan^{-1} \left[\frac{I_{pc}-I}{\Delta I} \right] + \tan^{-1} \left[\frac{I-I_{pp}}{\Delta I} \right] \right\} \quad (2.6-3)$$

where θ is colatitude, I is the latitudinal grid index (lowest near the pole, highest near the equator); $(d\theta/dI)_{max}$, $(d\theta/dI)_{min}$, ΔI , I_{pc} , and I_{pp} are adjustable parameters that represent the approximate maximum and minimum grid spacing, the width of the transition region between dense and undense spacings, and the I -locations of the boundaries of the dense-grid region. (Here "pc" means "polar cap", "pp" means "plasma pause".) Equation (2.6-3) integrates to the form

$$\begin{aligned} \theta(I) = & \theta(1) + (I-1) \left[\frac{d\theta}{dI} \right]_{max} + \\ & + \frac{\Delta I}{\pi} \left\{ \left[\frac{d\theta}{dI} \right]_{max} - \left[\frac{d\theta}{dI} \right]_{min} \right\} \left\{ -F \left(\frac{I_{pc}-I}{\Delta I} \right) + F \left(\frac{I-I_{pp}}{\Delta I} \right) + F \left(\frac{I_{pc}-1}{\Delta I} \right) - F \left(\frac{1-I_{pp}}{\Delta I} \right) \right\} \end{aligned} \quad (2.6-4a)$$

where

$$F(x) = x \tan^{-1}(x) - \frac{1}{2} \ln(x^2+1) \quad (2.6-4b)$$

The present MSM uses the following numerical values:

$$(d\theta/dI)_{max} = 2.0^\circ \quad (2.6-5a)$$

$$(d\theta/dI)_{min} = 0.4^\circ \quad (2.6-5b)$$

$$\Delta I = 2 \quad (2.6-5c)$$

$$I_{pc} = 6 \quad (2.6-5d)$$

$$I_{pp} = 55 \quad (2.6-5e)$$

Figure 2.6-1 shows a plot of colatitude vs. I for the coordinate system that is being delivered with the MSM. The I coordinate runs from 1 up to $IMAX$, which we have chosen to be 62 in the present case; the maximum colatitude is 49.10° .

In the program, we use the following conventions with regard to grid-spacing:

$$\left[\frac{d\theta}{dI} \right] = ALPHA \times DLAM \quad (2.6-6)$$

where $[d\theta/dI]$ is in radians, and the constant $DLAM$ is equal to $1/(IMAX-1)$, which is $1/61$ in the present case. The distance between local-time grid points

$$BETA \times DPSI \times RI$$

where $DPSI = 2\pi/(JMAX-3)$ and RI is the geocentric distance of the ionosphere, which is set equal to 6500 km. It follows that $BETA = \sin(\theta)$.

The RCM's coordinate grid is assumed to rotate with the Earth. At midnight Universal Time, $J = 3$ is at local noon in the ionosphere, $J = 15$ is at local dusk, $J = 27$ is at local midnight, and $J = 39$ is at local dawn.

The colatitude θ for grid point (I, J) is called $COLAT(I, J)$ in the program, while the local time of the same grid point is called $ALOCT(I, J)$. The general structure of the program allows both $COLAT$ and $ALOCT$ to vary with both I and J . However, we have not taken advantage of that flexibility in the present version of the MSM: at present, $COLAT$ really depends only on I and $ALOCT$ depends only on J .

The present version of the MSM does not include the effects of dipole tilt, as discussed in Section 2.3. The code implicitly assumes that the Earth's magnetic dipole is aligned with the rotation axis. Also, the magnetic-field strength at ionospheric height is assumed to be purely dipolar. For a planet whose magnetic field is purely dipolar and whose dipole axis is aligned with the rotation axis, geographic coordinates, geomagnetic-dipole coordinates, corrected geomagnetic coordinates, and invariant latitude all become coincident. When applying model predictions to the real Earth, it is best to interpret the model's $COLAT$ as either invariant colatitude or corrected geomagnetic colatitude and the model's $ALOCT$ as magnetic local time.

2.6.1.3. Equation of Motion in Terms of the MSM Grid.

The drift equation (2.6-2a), written in terms of motion of a particle in the MSM's grid system, takes the following form:

$$\frac{di}{dt} = \frac{1}{ALPHA \times BETA \times DLAM \times DPSI \times BIR \times RI^2} \left(\frac{\partial V_{eff}}{\partial J} \right)_I \quad (2.6-7a)$$

$$\frac{dj}{dt} = \frac{1}{ALPHA \times BETA \times DLAM \times DPSI \times BIR \times RI^2} \left(\frac{\partial V_{eff}}{\partial I} \right)_J \quad (2.6-7b)$$

where BIR is the strength of the radial component of the magnetic field at ionospheric altitude (taken to be positive).

2.6.2. Operation of the Particle Tracer.

2.6.2.1. Walking Test Particles Backwards in Time.

Suppose that we know the flux levels at all grid points (I, J) and for all invariant-energy levels IE , for time t , and we wish to step along to time $t + \Delta t$. (The basic time step Δt of the model is set in the code to be 15 minutes; our choice of Δt was arbitrary, and could easily be changed.)

To calculate the plasma distribution at time t to calculate the known distribution at $t + \Delta t$, the particle-trace program utilizes the electric- and magnetic-field configurations, which were computed for all times through the run before the particle tracer was first called. Using this known fields, the particle tracer starts a test particle of each species IE from each grid point (I, J) and walks backward in time from $t + \Delta t$ to t . The objective of the backward walk is to determine the location (i_t, j_t) of the test particle at time t .

The backward walk is accomplished numerically by means of a fourth-order Runge-Kutta procedure, with a fifth-order correction. The Runge-Kutta time step is adjusted automatically by a standard error-check algorithm. When it needs to calculate the velocities (equation (2.6-7)) at an arbitrary point (i', j') and time t' , the program calculates $ALPHA$, $BETA$, and BIR by straightforward linear interpolation amongst the neighboring grid points. To calculate $\partial V_{eff}/\partial I$ and $\partial V_{eff}/\partial J$, the program linearly interpolates in time and uses central differences to calculate $\partial V_{eff}/\partial I$ and $\partial V_{eff}/\partial J$ at the four grid points nearest (i', j') . It then calculates the derivatives at (i', j') by straightforward 2d linear interpolation.

2.6.2.2. The Loss Equation and its Integration.

The algorithm described here divides the loss into two types, one that involves strong pitch-angle scattering above a threshold, another that involves a lower level of loss due to some kind of background noise.

We assume that loss is governed by the following differential equation:

$$\frac{D\eta}{Dt} = - \text{Max} \left[\frac{\text{Max}[0, (\eta - \eta_{eq})]}{\tau_{weak}}, \frac{\text{Max}[0, (\eta - \eta_{thresh})]}{\tau_{strong}} \right] \quad (2.6-8)$$

where $\text{Max}(x,y)$ is the larger of x and y , $(\tau_{\text{weak}})^{-1}$ is a background-noise-related loss rate that is far below the strong-pitch-angle scattering rate (discussed in Section 2.6.3.1), and $(\tau_{\text{strong}})^{-1}$ is a rate that is close to the strong-pitch-angle-scattering limit (discussed in Section 2.6.3.2). The parameter η_{thresh} is a threshold density for the onset of strong pitch-angle scattering (discussed in Section 2.6.3.1). It is additionally assumed that there is a threshold for weak pitch-angle scattering: it is assumed that weak scattering drives the invariant density down to a low level η_{eq} , which corresponds to j_{min} , as defined in equation (2.5-29). Imposition of the loss cutoff η_{eq} , prevents the invariant density from dropping to unphysically low values.

The loss calculation is carried out after the traceback for a given test particle from $t+\Delta t$ to time t has been completed. Specifically, we assume that the program remembers, for each step m of the traceback, the values of the weak loss rate $(\tau_{\text{weak}})^{-1}$ and the strong loss rate $(\tau_{\text{strong}})^{-1}$ at the beginning/end of each time step. The program also remembers the density levels η_{eq} and η_{thresh} at the interval end time $t+\Delta t$.

Consider now the decrease in η during the time step from t_{m-1} to t_m , which is between mark time t and the next mark time $t+\Delta t$. We first check to see which of the two terms on the right side of (2.6-8) is to be taken as larger for this step. We do this using

$$\frac{\text{Max}[0, (\eta(m-1) - \eta_{\text{eq}}(f))]}{\tau_{\text{weak}}(m-.5)}$$

for the first term and

$$\frac{\text{Max}[0, (\eta(m-1) - \eta_{\text{thresh}}(f))]}{\tau_{\text{strong}}(m-.5)}$$

for the second; here we take

$$\tau_i(m-.5) = \frac{1}{2} [\tau_i(m-1) + \tau_i(m)]$$

where i is either "weak" or "strong". If both of these terms are zero, then, of course, η remains constant from t_{m-1} to t_m . If at least one is positive, then the differential equation (2.6-8) takes the form

$$\frac{D\eta}{Dt} = - \frac{(\eta - \eta_{i,m})}{\tau_m} \quad (2.6-9)$$

The parameters $\eta_{i,m}$ and τ_m are taken to be either $\eta_{\text{eq}}(t+\Delta t)$ and $\tau_{\text{weak}}(m-.5)$, or $\eta_{\text{thresh}}(t+\Delta t)$ and $\tau_{\text{strong}}(m-.5)$, whichever is appropriate. In either case, we take $\eta_{i,m}$ and τ_m to be constants through the time step, which means that (2.6-9) can be immediately integrated to give

$$\eta(m) - \eta_i(m) = [\eta(m-1) - \eta_i(m)] \exp\left(-\frac{(t_m - t_{m-1})}{\tau_m}\right) \quad (2.6-10)$$

We walk forwards in time through the interval from t to $t+\Delta t$ by repeated use of (3).

2.6.3. Electron Loss

2.6.3.1. The Electron Strong-Pitch-Angle-Scattering Rate

The strong-pitch-angle-scattering loss rate is defined by

$$\frac{1}{\tau_{full}} = \frac{v}{2B_i \int \frac{ds}{B}} \quad (2.6-11)$$

where v is the velocity of the particle's gyro- and bounce motion, and B_i is the magnetic-field strength at the ionosphere. Assuming loss at the rate given by (2.6-11) corresponds to assuming that the pitch angle is everywhere isotropic, so that the loss cone is completely full. Rewriting (2.6-11) in the terminology and units of the MSM gives

$$\frac{1}{\tau_{full}[x(t)]} = (4.45 \times 10^{-17}) \frac{|\lambda|^{1/2} VM^2 \sin(I)}{m^{1/2} B_{ir}} \quad (2.6-12)$$

If λ , VM , and B_{ir} are in our usual program units [eV $(R_E/nT)^{2/3}$, $(R_E/nT)^{-2/3}$, and nT, respectively] and m is in kg, then this loss rate comes out in sec^{-1} . The base loss rate is given by this full strong-pitch-angle-scattering rate, multiplied by an additional factor that we estimate on the basis of results obtained by *Schumaker et al.* [1989]. Specifically, we set

$$\frac{1}{\tau_{strong}} = \frac{f_o}{\tau_{full}} \quad (2.6-13)$$

where

$$f_o = 0.333 \text{ for } Kp \leq 1.5 \quad (2.6-14a)$$

$$f_o = 0.333 (2.5 - Kp) + 0.667 (Kp - 1.5) \text{ for } 1.5 \leq Kp \leq 2.5 \quad (2.6-14b)$$

$$f_o = 0.667 \text{ for } Kp \geq 2.5 \quad (2.6-14c)$$

2.6.3.2. $j_{threshold}$ for Electron Strong Pitch-Angle Scattering.

The classic paper of *Kennel and Petschek* [1966] predicted that there would be a threshold flux for the onset of electron strong pitch-angle scattering by whistlers, and that that threshold would be approximately proportional to L^{-4} . On the other hand, the paper by *Baker et al.* [1979] found observational evidence for such a threshold, but set it at $\sim 5 \times 10^7 \text{ cm}^{-2} \text{ s}^{-1} \text{ sr}^{-1}$ for $E > 40 \text{ keV}$, which is about 10 times the level originally suggested by Kennel and Petschek. We thus write

$$J_{KP \text{ thresh}}(>40 \text{ keV}) = (5 \times 10^7 \text{ cm}^{-2} \text{ s}^{-1} \text{ sr}^{-1}) \left[\frac{6.6}{r} \right]^4 \quad (2.6-15)$$

Equation (2.6-15) can be related to differential flux for a kappa-type distribution function, using equation (2.5-2). Integrating the resulting expression over energy from 40 keV to infinity gives

$$J(>40 \text{ keV}) = (1.68 \times 10^8 \text{ cm}^{-2} \text{ s}^{-1} \text{ ster}^{-1}) F(\kappa) \left(\frac{\kappa-1}{\kappa} \right) \left[\frac{E_o}{1 \text{ keV}} \right]^{1/2} \left[\frac{N}{1 \text{ cm}^{-3}} \right] \left[\frac{1 + \frac{40 \text{ keV}}{E_o}}{1 + \frac{40 \text{ keV}}{\kappa E_o}} \right]^\kappa \quad (2.6-16)$$

We thus define an energy ratio E_R as follows:

$$E_R = \frac{j(E)}{J(>40 \text{ keV})} = \left(\frac{1}{E_o}\right)^{\left(\frac{\kappa-1}{\kappa}\right)} \frac{\left(\frac{E}{E_o}\right)^{\left(1+\frac{40 \text{ keV}}{\kappa E_o}\right)^{\kappa}}}{\left(1+\frac{E}{\kappa E_o}\right)^{\kappa+1} \left(1+\frac{40 \text{ keV}}{E_o}\right)} \quad (2.6-17)$$

Note that, if $j(E)$ is to come out in $\text{cm}^{-2} \text{s}^{-1} \text{eV}^{-1} \text{sr}^{-1}$, as is our usual convention, then, in the initial multiplying factor $1/E_o$ on the right side of (14), E_o should be in eV.

For $r = 3, 4, 6.6$, and 13 , we can use the values of κ and E_o that were adopted in the calculation of *FLXMAT*, as described in Section 2.5.2. They are summarized in the following table:

r	Kp	κ	$E_o(\text{keV})$
3	all	2.8	23.5
4	all	2.0	16
6.6	0	6	21
6.6	1	6	4.8324
6.6	2	6	4.8140
6.6	3	6	4.7978
6.6	4	6	4.8160
6.6	5	6	4.8943
6.6	≥ 6	6	5.0752
13	all	6	$.2885(Kp-1)+.15625(5-Kp)$

To calculate the threshold flux, then, we use

$$j_{\text{thresh}}(r, E) = (5 \times 10^7 \text{ cm}^{-2} \text{s}^{-1} \text{sr}^{-1}) E_R(r, E) \left[\frac{6.6}{r}\right]^4 \quad (2.6-18)$$

Equation (2.6-18) is designed to give the threshold flux for energies above about 40 keV. Below 20 keV, the results of *Schumaker et al.* [1989] indicate that the scattering rate is close to the strong limit, as indicated in (2.6-13) and (2.6-14), but they do not suggest evidence of a clear threshold. However, to prevent fluxes from dropping to unphysical low values, we continue in the MSM to use a threshold value of η_{eq} that represents a quiet-time minimum flux level.

To span our required energy range, I propose that we use a mixed algorithm. For energies below 20 keV or below 40 keV, we make the obvious choices:

$$j_{\text{thresh}} = j_{eq} \text{ for } E \leq 20 \text{ keV} \quad (2.6-19a)$$

$$j_{\text{thresh}} = \text{value from (2.6-18) for } E \geq 40 \text{ keV} \quad (2.6-19b)$$

Between 20 and 40 keV, we do a log-linear interpolation in energy:

$$\log(j_{\text{thresh}}(E)) = \left[\frac{(40-E) \log(j_{\text{thresh}}(20)) + (E-20) \log(j_{\text{thresh}}(40))}{20} \right] \quad (2.6-20)$$

for $20 \text{ keV} < E < 40 \text{ keV}$.

Near the beginning of each run, the MSM computes a matrix of values of $\log_{10}(j_{\text{thresh}})$, in analogy with the matrix *FLXMAT*. This provides values of $\log_{10}(j_{\text{thresh}})$ for $Kp=0, 1, 2, 3, 4, 5$, and 6 , for $r = 3, 4, 6.6$, and 13 , and for appropriate logarithmically spaced energy levels. As usual, we can convert j_{thresh} to η_{thresh} using equation (2.5-23).

2.6.3.3. Weak Loss Rate

Calculation of the weak loss rate depends on whether we are inside or outside of the plasmopause. Although we don't keep track of the plasmopause in the model, we can estimate its equatorial geocentric distance as follows:

$$r_{pp} = \frac{1}{\cos^2(\Lambda_{eq.edge,mid.})} \quad (2.6-21)$$

τ_{weak} inside the plasmopause. If $r < r_{pp}$, then we directly use Lyons' classic calculation of the loss lifetimes of electrons due to pitch-angle scattering from plasmaspheric hiss *Lyons et al.* [1972]. We found log-parabolic analytic approximations to the published curves. The results for 20, 50, 200, and 500 keV are as follows:

$$\log_{10}(\tau_{\text{weak}}(20 \text{ keV})) = (4.9365 + 15.8621) - 6.06897 r + 0.551724 r^2 \quad (2.6-22a)$$

$$\log_{10}(\tau_{\text{weak}}(50 \text{ keV})) = (4.9365 + 13.5172) - 5.58621 r + 0.551724 r^2 \quad (2.6-22b)$$

$$\log_{10}(\tau_{\text{weak}}(200 \text{ keV})) = (4.9365 + 1.15517) - 0.42069 r + 0.0275862 r^2 \quad (2.6-22c)$$

$$\log_{10}(\tau_{\text{weak}}(500 \text{ keV})) = (4.9365 + 3.89655) - 1.75862 r + 0.206897 r^2 \quad (2.6-22d)$$

For energies below 50 keV, use a linear interpolation between (2.6-22a) and (2.6-22b); for energies between 50 and 200 keV, use linear interpolation between (2.6-22b) and (2.6-22c), etc. Of course, we shouldn't really calculate fluxes for energies above about 300 keV, since we aren't even using relativistic drift formulas. Figure 2.6.2 shows a plot of lifetimes computed from these algorithms.

Estimation of τ_{weak} outside the plasmopause. We have very little solid information concerning τ_{weak} outside the plasmopause, but we have to make a reasonable estimate. It is known that a substantial fraction of the $\sim 50 \text{ keV}$ electrons are lost as they traverse the day side of the magnetosphere, which takes \sim an hour. We therefore assume that, for synchronous particles with 50-300 keV, the peak dayside loss lifetime is $\sim 0.5 \text{ hr}$. Based on the plots in the paper by *Frank et al.* [1964], we estimate that the peak dayside precipitation rate is ~ 10 times the nightside rate. Therefore, we assume that

$$(\tau_{weak}(6.6))^{-1} = \text{Min}\left(\frac{E}{20 \text{ keV}} - 1, 1\right) \left(\frac{1}{3600 \text{ s}}\right) \left[1 + \left(\frac{9}{11}\right) \cos(\phi)\right] \text{ for } E > 20 \text{ keV} \quad (2.6-23a)$$

$$(\tau_{weak}(6.6))^{-1} = 0 \text{ for } E \leq 20 \text{ keV} \quad (2.6-23b)$$

There is no need for this extra term for electrons below 20 keV, because the strong-pitch-angle-scattering threshold is low there anyway.

For geocentric distances between r_{pp} and 6.6, we use a linear interpolation between Lyons' results for the plasmopause and (2.6-23), as follows:

$$(\tau_{weak}(r))^{-1} = \left(\frac{6.6 - r}{6.6 - r_{pp}}\right) (\tau_{weak}^{(8)}(r_{pp}))^{-1} + \left(\frac{r - r_{pp}}{6.6 - r_{pp}}\right) (\tau_{weak}^{(9)}(6.6))^{-1} \quad (2.6-24a)$$

Of course, if $r_{pp} > 6.6$, we shouldn't use (2.6-24a). For $r > 6.6$, assume that

$$(\tau_{weak}(r))^{-1} = (\tau_{weak}^{(10)}(6.6))^{-1} \quad (2.6-24b)$$

2.6.4. Ion Loss

2.6.4.0. Introductory Comments.

Loss of magnetospheric ions takes place by two physically different mechanisms: precipitation and charge exchange. Because charge exchange is more significant overall and can be estimated much more reliably, we have simply neglected ion loss by precipitation. In applying equation (2.6-8), charge exchange is treated as "weak loss". The strong-loss rate is set equal to zero for ions.

The main technical discussion of charge-exchange loss, Section 2.6.4.1, was written by Dr. James Bishop (Department of Atmospheric and Oceanic Science, University of Michigan, Ann Arbor, MI 48109), who performed the calculations. Technical questions about the calculations should be directed to him. His phone number is (313)936-0516.

Section 2.6.4.2 describes the tabular form in which the charge-exchange calculations are included in the MSM.

2.6.4.1. Charge Exchange Theory.

We consider a stationary situation, in which ion energy (speed) remains constant along the bounce path. The degree of erosion is determined solely by the amount of geocoronal atomic hydrogen "experienced" by the ring current ions -- i.e., the column depth along the helical path executed by the mirroring ions. Note that charge exchange (CE) collisions act strictly as a loss mechanism. (We will neglect the thermal atom speeds.)

We will focus on H^+ and O^+ ions with energies 1-200 keV.

First consider the ideal case where the initial equatorial kinetic distribution function (KDF) for ring current (RC) ions of species i is isotropic and mono-energetic:

$$f_i(v, \alpha, 0, 0) = \frac{n_i(0, 0)}{4\pi v^2} \delta(v - v') \quad (2.6-25)$$

where $n_i(s, t)$ is the density of species i at location s (arclength along the field line from the equator, sometimes we will use magnetic latitude Λ) and at time t , and $f_i(v, \alpha, s, t)$ is the underlying KDF at speed v and pitch angle α . Further, we assume that initially $f_i(v, \alpha, s, 0)$ is equivalent to $f_i(v, \alpha, 0, 0)$ in the sense of Liouville's equation – i.e., f_i is constant along the bounce path – and that no "injection" occurs for $t > 0$. Then we can write for the subsequent evolution

$$f_i(v, \alpha, 0, t) = f_i(v, \alpha, 0, 0) e^{-\tau_i(\alpha, t)} \quad (2.6-26)$$

where $\tau_i(\alpha, t)$ is the "depth" of geocoronal H traversed. $\tau_i(\alpha, t)$ is a trajectory-dependent quantity, conveyed in the notation by the dependence on pitch angle α :

$$\tau_i(\alpha, t) = \int dl n_H \sigma_i(v) = \int_0^t dt' v(t') n_H(r(t')) \sigma_i(v(t')) = v \sigma_i(v) \int_0^t dt' n_H(r(t')) \quad (2.6-27)$$

where dl is an element of path length along the ion trajectory. We have used the constancy of v and the fact that σ_i (the charge exchange cross section for ion species i) is a function of speed alone. The equatorial density is

$$\begin{aligned} n_i(0, t) &= \int d^3 v f_i(v, \alpha, 0, t) \\ &= \int_0^{2\pi} d\phi \int_0^\pi d\alpha \sin \alpha \int_0^\infty dv' v'^2 \frac{n_i(0, 0)}{4\pi v'^2} \delta(v - v') e^{-\tau_i(\alpha, t)} \\ &= n_i(0, 0) \int_0^{\pi/2} d\alpha \sin \alpha e^{-\tau_i(\alpha, t)} \end{aligned} \quad (2.6-28)$$

Several comments are required:

(i) In equation (2.6-27), we have used the assumption of Liouville equivalence along the bounce path at time $t = 0$ and time reversal symmetry: An assemblage of ions with speeds in the range $(v, v+dv)$ and pitch angles in the range $(\alpha, \alpha+d\alpha)$ passing the equator at time $t = 0$ will all be located at time t' at a position s' with speeds $(v', v'+dv')$ and pitch angles $(\alpha', \alpha'+d\alpha')$ in the absence of CE erosion. An assemblage initially at s' with speeds $(v', v'+dv')$ and pitch angles $(\pi-\alpha', \pi-(\alpha'+d\alpha'))$ will at time t' be located at the equator. Each assemblage traverses the same helical column of geocoronal H, so each will experience the same erosion.

(ii) The quarter-bounce time (the time for an ion of speed v' and pitch angle α to go from equator to mirror point) is

$$\tau_B(r_{eq}, v, \alpha_{eq}) = \int_0^{s_B} \frac{ds}{v_{||}(s)} = \frac{r_{eq}}{v} \int_0^{\Lambda_B} \frac{\cos \Lambda [4 - 3 \cos^2 \Lambda]^{1/2}}{\left[1 - \frac{B(\Lambda)}{B_{eq}} \sin^2 \alpha_{eq}\right]^{1/2}} d\Lambda \quad (2.6-29)$$

for a dipole magnetic field; here B is the magnetic field strength, r_{eq} is the equatorial radius of the field line, s_B is the arclength along the field line to the mirror point, and Λ_B is the magnetic latitude of the mirror point (the subscript B denotes mirror point quantities). The integral is speed and species independent. The helical quarter-bounce column density of geocoronal H is

$$\mathcal{N}_B(r_{eq}, \alpha_{eq}) = r_{eq} \int_0^{\Lambda_B} \frac{\cos \Lambda [4 - 3 \cos^2 \Lambda]^{1/2}}{\left[1 - \frac{B(\Lambda)}{B_{eq}} \sin^2 \alpha_{eq}\right]^{1/2}} n_H(r_o, \Lambda) d\Lambda \quad (2.6-30)$$

The total column of geocoronal H traversed by an ion of speed v in a duration t can be written

$$\begin{aligned} \int_0^t dt' n_H(r(t')) &= m \mathcal{N}_B(r_{eq}, \alpha_{eq}) + \int_0^{s(t)} ds' \frac{n(s')}{v_{||}(s')/v}, \quad m \text{ even} \\ &= (m+1) \mathcal{N}_B - \int_0^{s(t)} ds' \frac{n(s')}{v_{||}(s')/v}, \quad m \text{ odd} \end{aligned} \quad (2.6-31)$$

where m is the number of full quarter-bounces executed in the duration t and $s(t)$ denotes the location along the field line at the time t . If $t \gg \tau_B$, then to good approximation we can drop the "remainder" terms and work entirely in terms of quarter-bounce quantities. In particular, we can evaluate $v\tau_B(r_{eq}, \alpha_{eq})$ and $\mathcal{N}_B(r_{eq}, \alpha_{eq})$ at the outset. The evolution is then readily followed using

$$\tau_i(\alpha, t) \approx m \sigma_i(v) \mathcal{N}_B(r_{eq}, \alpha_{eq}) \quad (2.6-32)$$

where $m = \text{INT}(t/\tau_B)$; note that m is a function of v , α_{eq} , and r_{eq} .

(iii) In practice, pitch angles are limited by the loss cone α_{LOSS} : ions with pitch angles $\alpha < \alpha_{LOSS}$ have mirror points so deep in the atmosphere that they are effectively removed on the first quarter-bounce. Thus, when the α -integral is evaluated, the summation

algorithm will generate quadrature points dependent on α_{LOSS} , which in turn is dependent on r_{eq} .

(iv) The equatorial density should track with the flux tube content as long as $\tau_B \ll \tau_{eff}$, where the effective decay time for equatorial pitch angle α_{eq} is

$$(\tau_{eff})^{-1} \equiv \frac{-1}{f_i} \frac{df_i}{dt} = \frac{d\tau_i(\alpha, t)}{dt} = v \sigma_i(v) n_H(r(t)) \quad (2.6-33)$$

where $r(t)$ is a function of α_{eq} (and r_{eq}). Recognizing $v\tau_B$ to be the helical quarter-bounce path length, a mean n_H -value is $N_B/v\tau_B$, so a mean τ_{eff} -value for the bounce motion is $\sigma_i(v)N_B/\tau_B$. Thus, as long as $1 \gg \sigma_i(v)N_B$ we can use the equatorial density as a measure of flux tube content. For typical geocoronal conditions, $N_B < 10^{-14} \text{ cm}^2$, so we require $\sigma \ll 10^{-14} \text{ cm}^2$, which is generally the case. (Note that another problem arises if the durations of evaluation t are comparable to τ_B , since then we cannot neglect the remainder terms in (2.6-31).)

Now we consider the case where f_i has a binned speed distribution, but is still initially isotropic:

$$f_i(v, \alpha, 0, 0) = \frac{n(0,0)}{4\pi} \sum_{i=1}^{N-1} H(v_i, v_{i+1}) h_i \quad (2.6-34)$$

where $v_i, i = 1, 2, \dots, N$ are the speeds defining the $N-1$ bins, $H(v_i, v_{i+1}) = 1$ for $v_i \leq v_{i+1}$ and 0 otherwise, and the weights h_i for each bin are normalized so that

$$\sum_{i=1}^{N-1} \left[h_i \frac{(v_{i+1}^3 - v_i^3)}{3} \right] = 1$$

Thus we consider a discrete, finite set of speeds representative of each bin: $c_j, j = 1, 2, \dots, N-1$. The equatorial density in this case is

$$n_i(0, t) = \int d^3v f_i(v, \alpha, 0, t) = n_i(0, 0) \sum_{i=1}^{N-1} h_i \int_0^{\pi/2} d\alpha \sin \alpha e^{-\tau_{ij}} \quad (2.6-35)$$

where

$$\tau_{ij} \approx m \sigma_i(c_j) N_B(r_{eq}, \alpha_{eq}) \quad (2.6-36)$$

Please refer to Figures 2.6-3 to 2.6-5 for sample numerical results of the calculation.

With regard to accuracy, the primary source of error in the basic charge-exchange calculation probably lies in the use of a very simple model exosphere and in using a crude approximation to the solar-cycle dependence of that atmosphere. For $L < 4$, where charge exchange is fast, we hope that the rates are accurate to a factor of two. For large L , the assumption of a dipole field in the calculation decreases accuracy somewhat further.

2.6.4.2. Incorporation of Charge-Exchange Calculations in the MSM.

In the basic charge-exchange calculations, each ion is assumed to drift on its original L -shell. However, the ion pitch-angle distribution changes in time, due to the rapid erosion of particles with small pitch angles, which experience higher average neutral densities than particles with pitch angles near 90° .

It is clear, however, from Figure 2.6-5 that, after a relatively brief interval, the overall density for given E and L decays approximately exponentially. Since the implementation of the charge-exchange calculation in the MSM has to execute extremely fast, we chose to take advantage of this approximate exponentiality, to avoid the necessity for having the MSM keep track of the time evolution of the pitch-angle distribution on each flux tube. Dr. Bishop provided us with a table of loss lifetimes for H^+ and O^+ for various energies and L -values, and also for both high and low solar activity. The MSM reads this table from disk near the beginning of each run. Charge-exchange rates are computed, time-step by time-step, by interpolation of the table in energy and L -value.

2.6.5. Calculation of the Fluxes of Precipitating Particles

2.6.5.0. Introductory Comments.

Ion precipitation in the MSM is treated simply in terms of the statistical model of *Hardy et al.* [1989], which is the most reliable model available at present. A subroutine embodying that model was kindly provided by D. A. Hardy of the USAF Geophysics Laboratory.

Within the region where we carry out detailed particle traces, we compute the energy flux in auroral-electron precipitation in terms of loss from our model plasma sheet. Electrons are assumed to precipitate at the rate calculated according to the algorithms described in Section 2.6.3, with no acceleration by field-aligned potential drops. The procedure for calculating the energy flux and average energy of the precipitating electrons is described in Section 2.6.5.1.

Poleward of our main modeling region, we use a procedure that is based indirectly on the statistical model of *Hardy et al.* [1985]. It is described in Section 2.6.5.2.

2.6.5.1. Calculation of Precipitating Electron Fluxes within our Main Modeling Region.

We compute the auroral precipitation from the invariant densities η that are computed by the main particle-trace procedure, subjected to loss as discussed in Section 2.6.3.

For each (IEJ, J) , it is useful to define a net rate (which is in sec^{-1} and is the inverse of the mean precipitation lifetime of the particles in question):

$$RATE = \frac{1}{\eta} \left\{ \text{Max} \left[\frac{\text{Max}[0, (\eta - \eta_{eq})]}{\tau_{weak}}, \frac{\text{Max}[0, (\eta - \eta_{thresh})]}{\tau_{strong}} \right] \right\} \quad (2.6-37)$$

The number of particles of species IE precipitating from a flux tube of unit magnetic flux into a unit area in the ionosphere (one hemisphere) is given by

$$\Phi_N = \frac{RATE * \eta * B_{ir}}{2 \times 10^{13}} \quad (2.6-38)$$

where the factor of 2 comes from the fact that Φ_N is a one-hemisphere rate, and the factor of 10^{13} comes from converting from nanoteslas to teslas and from m^{-2} to cm^{-2} . Φ_N comes out in particles/cm²/s. The precipitating energy flux per hemisphere in species IE is given by

$$\Phi_E = (0.8 \times 10^{-25}) RATE * \eta * B_{ir} * |\lambda| * VM \quad (2.6-39)$$

where the constant has been multiplied by 1.6×10^{-12} to convert from eV to ergs. The flux Φ_E is in ergs/cm²/s for one hemisphere and one species IE . The total hemispheric energy flux for one chemical species is given by

$$FLXSUM(I,J,K) = \sum_{IE} \Phi_E(IE,J) \quad (2.6-40)$$

where the sum over IE includes all IE -values that correspond to chemical species IK . The corresponding total number flux is given by

$$DENSUM(I,J,K) = \sum_{IE} \Phi_N(IE,J) \quad (2.6-41)$$

The average energy is given by

$$EAVG(I,J,K) = \frac{FLXSUM(I,J,K)}{DENSUM(I,J,K)} \quad (2.6-42)$$

2.6.5.2. Electron Precipitation Poleward of our Main Modeling Region.

Our formula for electron energy flux is expressed in terms of $P''(I,J)$, the power in precipitating electrons within the grid space (I,J) , in units of gigawatts. The relation between $P''(I,J)$ and E_{flux} , the precipitating energy flux in ergs/cm²/s, is

$$P''(I,J) = 10^{-6} E_{flux} \alpha(I) \beta(I) \Delta \lambda \Delta \psi R_f^2 \quad (2.6-43)$$

$P''(i,J)$ is assumed to be a cubic function of i , the floating-point version of the usual latitudinal grid index, and specifically to have the form

$$P''(i,J) = a [(i-i_l) + b (i-i_l)^2 + c (i-i_l)^3] \quad (2.6-44a)$$

for $i > i_l$, and

$$P''(i,J) = 0 \quad (2.6-44b)$$

for $i < i_l$. Here i_l is the i -location of the intersection of ellipse #1 with grid line J . Note that P'' is forced to go to zero at that ellipse. The three coefficients a , b , c are determined by the following requirements:

- (i) the cubic formula must agree with the results of the low-latitude computation for the first two grid points I that occur within the main modeling region, for local-time grid line J .
- (ii) it must give a designated amount of power (P_T) per unit J poleward of the main modeling boundary. For that power, we use the algorithm:

$$P_T = \int_{i_1}^{IMIN} di P''(I, J) = \left[\frac{F}{1-F} \right] \left(\frac{d(Power)}{dJ} \right)_{\text{in main modeling region}} \quad (2.6-45)$$

where

$$F = 0.5 + 0.3 \sin(\phi) \quad (2.6-46)$$

and ϕ is our local-time angle, (0 at noon, $\pi/2$ at dusk...). Formula (2.6-46) was originally derived by comparing the statistical electron-precipitation patterns of *Hardy et al.* [1985] with the Birkeland-current patterns of *Iijima and Potemra* [1978], associating the boundary of our main modeling region with the equatorward edge of the region-one currents. F. J. Rich of the USAF Geophysics Lab is carrying out a much more detailed study of the question of where the region-one current boundary falls with respect to the precipitation pattern; his preliminary results are reasonably consistent with (2.6-46).

Determination of i_1 : The size and shape of ellipse #1, which is the poleward edge of the electric-field reversal region of the ionosphere, is defined by the parameters $A(1)$ $B(1)$, $DX(1)$, and $DY(1)$. From the equation of the ellipse, we calculate the colatitude at which that ellipse crosses local-time grid line J . We then find the floating-point I -value at which the ellipse intersects local-time grid line J by simple linear interpolation on the *COLAT* matrix.

Determination of a , b , and c . Let P_1'' and P_2'' represent $P''(IMIN+1, J)$ and $P''(IMIN+2, J)$, respectively, where $IMIN$ is defined to be the largest I -value that lies poleward of our main modeling region. Also let $i_2 = IMIN - i_1$, $i_1 = IMIN + 1 - i_1$, $i_2 = IMIN+2 - i_1$. The formulas then are

$$a = \frac{P_T - \frac{i_2^3}{i_1^2 i_2} \left\{ \frac{1}{3} [P_1'' i_2^3 - P_2'' i_1^3] + \frac{1}{4} [P_2'' i_1^2 - P_1'' i_2^2] i_2 \right\}}{\frac{i_2^2}{2} \left[1 - \frac{2(i_1+i_2)}{3} \frac{i_2}{i_1 i_2} + \frac{1}{2} \frac{i_2^2}{i_1 i_2} \right]} \quad (2.6-47a)$$

$$b = \frac{P_1'' i_2^3 - P_2'' i_1^3 - a i_1 i_2 (i_1 + i_2)}{a i_1^2 i_2^2} \quad (2.6-47b)$$

$$c = \frac{i_1^2 P_2'' - i_2^2 P_1'' + a i_1 i_2}{a i_1^2 i_2^2} \quad (2.6-47c)$$

Determination of smoothed fluxes in region 1. The fluxes that we actually record for the grid points within region 1 should be related to the simple cubic formula (2.6-44a) (and (2.6-44b)) by a smoothing integration. We interpret $P''(I,J)$ as given in (2.6-44a) and (2.6-44b) as indicating the local precipitation rate at grid point (I,J) . Define $P_s''(I,J)$ to be the integral of the continuous function $P''(i,J)$ from $I - 0.5$ to $I + 0.5$. Assuming that $IMIN - i_l > 0.5$, which should normally be the case, then, for grid points in the range $i_l + 0.5 \leq I \leq IMIN$, we have

$$P_s'' = a \left\{ \frac{1}{2} [i_+^2 - i_-^2] + \frac{b}{3} [i_+^3 - i_-^3] + \frac{c}{4} [i_+^4 - i_-^4] \right\} \quad (2.6-48)$$

where $i_+ = I + 0.5 - i_l$ and $i_- = I - 0.5 - i_l$. For the I -value that is centered on the segment of the J -grid line that is cut by ellipse #1, i.e., the I -value that lies closest to ellipse #1, we have to cut off the integral at i_l rather than $I - 0.5$, and we get

$$P_s'' = a \left\{ \frac{1}{2} i_+^2 + \frac{b}{3} i_+^3 + \frac{c}{4} i_+^4 \right\} \quad (2.6-49)$$

In the unlikely event that $IMIN - i_l \leq 0.5$, then we should use formula (2.6-49) for $I = IMIN$, and $P_s'' = 0$ for smaller I -values. In any case, I propose that $P_s'' = 0$ for $I < i_l - 0.5$.

Emergency procedure in the case where $P_s'' < 0$ for some grid point. In this case, which should occur extremely rarely, we simply make P_s'' the same for all I in the range $i_l - 0.5 < I \leq IMIN$, and make the total satisfy

$$\sum_{i_l - 0.5 < I < IMIN} P_s''(I,J) + 0.5 P_s''(IMIN,J) = P_T(J)$$

2.7. Limitations of the Magnetospheric Specification Model.

The MSM is the first effort at a large-scale computational model of the Earth's magnetosphere for operational use. As indicated by the discussion of test results in Sections 3 and 4 of this report, this effort has been a success. With regard to its primary goal of specifying fluxes of < 100 keV electrons in the geostationary-orbit region, the MSM does a very good job. The MSM calculates these geostationary-orbit-region electrons within a comprehensive framework that also provides flux values throughout the middle magnetosphere, as well as magnetospheric inputs to the ionosphere and thermosphere.

At the same time, the MSM has not reached the ultimate goal of being capable of specifying all important physical parameters at all locations in the magnetosphere with high confidence of high accuracy for all conceivable conditions. The limitations result from three basic sources: (i) Our knowledge of the Earth's magnetosphere is far from complete; (ii) The input data that is expected to be available to the Space Forecast Center is far from ideal; (iii) Only a very limited amount of observational data has been available to test the model.

With regard to the MSM's primary goal of correctly specifying fluxes of 1-100 keV electrons in the geostationary-orbit region, the essential limitations are:

- A1. The MSM does not correctly represent flux dropouts in the > 40 keV electrons, and it sometimes specifies high fluxes when only average levels are observed. The operational impact of these deficiencies is reduced by the fact that the MSM automatically monitors and reports on its consistency with real-time observations from geostationary spacecraft.
- A2. Testing of the model has been limited by the available observational database. Although we expect the model to perform well for geostationary-orbit electrons below 35 keV, no spacecraft data have been available to test the MSM in this energy range.
- A3. The model has been tested for quiet periods and substorms, up through a moderately strong magnetic storm. It has not been possible yet to assemble a test data stream for a very large magnetic storm.
- A4. Although the MSM has been tested for two events that occurred nine years apart, it has not been tested for all phases of the solar cycle.

Two limitations that follow from the general formulation of the MSM are the following:

- B1. Its capabilities for forecasting are very limited unless an upstream solar-wind monitor is available.
- B2. It does not keep track of particle pitch-angle distributions.

With regard to the broader goal of specifying all important magnetospheric parameters throughout the middle magnetosphere, the capabilities of the MSM have generally not yet been as well tested as we would like. Nevertheless, we believe that the MSM makes useful estimates of electric fields, magnetic fields, and particle fluxes (up to ~ 300 keV) for the global ionosphere and for the region $3 < L < 10$ of the magnetosphere. The following specific limitations apply:

- C1. No flux estimates are currently made for electrons above about 300 keV at geostationary orbit (roughly $(300 \text{ keV})(L/6.6)^{-8/3}$ for other L -shells). H. C. Koons and D. J. Gorney have recently provided us with their algorithm for specifying and predicting > 3 MeV electrons for the geostationary-orbit region. However, that code was delivered after the April 1 end of the present contract, and we consequently have not yet been able to install and test the Koons-Gorney algorithm within the framework of the MSM. A new

version of the MSM that includes the Koons-Gorney algorithm will be delivered soon after July 1, 1990.

C2. For 100-300 keV electrons and 50-300 keV ions, the MSM calculates fluxes by scaling an internally computed set of base-level fluxes to fit the real-time-observed geostationary fluxes.

C3. The accuracy of the MSM for electrons < 100 keV $(6.6/L)^{8/3}$ becomes increasingly uncertain as L decreases far below 6.6, because our test data sets contained no spacecraft observations inside $L = 6.6$.

The present uncertainties concerning model performance should decrease rapidly over the next several years. A data stream is being collected for the great magnetic storm of March 1989, and MSM tests on that event will begin soon: this should eliminate limitation A3. For the period beginning in the Fall of 1989, additional particle detectors are being placed on DoD geostationary-orbit spacecraft: these new detectors, developed at Los Alamos, monitor fluxes of low-energy electrons and ions; we expect to assemble data sets to test the MSM, including those data, within the next year, thus eliminating limitation A2. The CRRES-SPACERAD spacecraft, scheduled for launch in July 1990, will provide a rich source of data for $L < 6.6$; thus within the next 1-2 years, limitation C3 will be eliminated. With this continued testing, limitation A4 will gradually be eliminated. The flexible, modular structure of the MSM will allow us to carry out simple "fixes" by changing very few lines of code, if the extended testing indicates the need for such changes.

2.8 MSM Output

The primary output of the MSM is the particle flux, for each energy, and species, on each grid point. The fluxes are labeled by the indices I, J, and K where I is the index specifying the geomagnetic colatitude and J specifies the magnetic local time of the grid point. K is the invariant energy index.

Fluxes are also specified on the model boundary.

The X, Y, and Z, position of each grid point on the equatorial reference surface is provided.

For the precipitating particles, the energy flux and average energy of the electrons and ions is given at each grid point.

A time tag is provided that gives the time of each output record.

Numerous other parameters are included in the output record. These include the input data parameters actually used by the model, as well as a large number of internal model parameters that can be used to restart the model or for diagnostic purposes.

Table 2.8 gives the entire list of output parameters together with their program names and units.

The parameter ERSHFT specifies the average difference between the model's prediction for the log of the geostationary flux and the average observed value for the last 15 minutes, for each MSM energy channel. This could, for example, provide a warning of an unexpected situation where the MSM is substantially underestimating the flux.

Table 2.8

MSM Output Parameters

PARAMETER	NAME	UNITS
PART. FLUX @ GRID POINTS I,J AND ENERGY K	FLUX (I,J,K)	$\#/Cm^2 S$
PART. FLUX ON BOUND. J & ENERGY K	FLXBND(J,K)	$\#/Cm^2 S$
(FLUX TUBE VOLUME) ^{-2/3} @ GRID POINT	VM(I,J)	$(Re/nT)^{-2/3}$
X POSITION OF GRID POINT I,J ON EQUAT. REF. SURF.	X(I,J)	Re
Y POSITION OF GRID POINT I,J ON EQUAT. REF. SURF.	Y(I,J)	Re
Z POSITION OF GRID POINT I,J ON EQUAT. REF. SURF.	Z(I,J)	Re
ENERGY FLUX OF ELECTRONS @ IONOSPHERE G.P. I,J	FLXSUM(I,J,1)	$ERG/Cm^2 S$
AVERAGE ENERGY OF ELECTRONS @ IONOSPHERE G.P. I,J	EAVG(I,J,1)	KEV
ENERGY FLUX OF IONS @ IONOSPHERE G.P. I,J	FLXSUM(I,J,2)	$ERG/Cm^2 S$
AVERAGE ENERGY OF IONS @ IONOSPHERE G.P. I,J	EAVG(I,J,2)	KEV
POTENTIAL @ IONOSPHERIC G.P. I,J	V(I,J)	VOLTS
MAGNETIC COLATITUDE OF IONOSPHERIC G.P. I,J	COLAT(I,J)	RADIANS
MAGNETIC LOCAL TIME OF IONOSPHERIC G.P. I,J	ALOCT(I,J)	RADIANS east from noon
MAGNETOPAUSE STANDOFF DISTANCE	STFD	Re
DIPOLE TILT ANGLE	TILT	DEGREES
TAIL CURRENT SHEET DENSITY	HJNEAR	N/A
RATIO TAIL I @ INFINITY TO TAIL I @ INNER EDGE	HJFRAC	N/A
Y VARIATION OF CROSS-TAIL CURRENT	DDY	Re
CURRENT SHEET THICKNESS PARAMETER	DD	Re
DEGREE OF COLLAPSE MIDNIGHT REGION TAIL	COLLAP	N/A
RANGE IN X AFFECTED BY TAIL COLLAPSE	DELXCL	Re
PARM. DETER. THE Y-DEP OF COLLAPSE CURRENT	DYC	Re
-B PERT. @ EARTH CENTER DUE TO WEST RING I	BRN	NANOTESLA
+B PERT. @ EARTH CENTER DUE TO EAST RING I	BRP	NANOTESLA
RADIUS OF THE WESTWARD RING CURRENT	RHRN	Re
RADIUS OF THE EASTWARD RING CURRENT	RHRP	Re
MAGNETIC FIELD STRENGTH ON EQUAT. REF SURFACE	BMIN(I,J)	NANOTESLA
POLAR CAP POTENTIAL DROP	PCP	KV
POLAR CAP PATTERN TYPE	IPATT	N/A
RATE OF MOTION OF THE LOW LAT. AURORAL BOUNDARY	DEQDT	DEGREES/HR
BOUNDARY 2 & 3 ELLIPSE SPECIFICATION PARAMETER	A(L)	DEGREES
BOUNDARY 2 & 3 ELLIPSE SPECIFICATION PARAMETER	B(L)	DEGREES
BOUNDARY 2 & 3 ELLIPSE SPECIFICATION PARAMETER	DX(L)	DEGREES
BOUNDARY 2 & 3 ELLIPSE SPECIFICATION PARAMETER	DY(L)	DEGREES
ELECTRIC POTENTIAL N. IONOSPHERE	VNORTH(I,J)	VOLTS
ELECTRIC POTENTIAL S. IONOSPHERE	VSOUTH(I,J)	VOLTS
BOUNDARY LOCATION IN OUR GRID	BNDLOC(J)	I GRID UNITS
LOGARITHMIC ERROR SHIFT	ERSHFT(K)	$LOG_{10} (\#/Cm^2 S)$
PROCESSED INPUT ARRAY	AUGPAR	VARIOUS UNITS
TIME TAG OF RECORD TIME	TIME	YR:DAY SEC

MSM SIMPLIFIED FLOW CHART

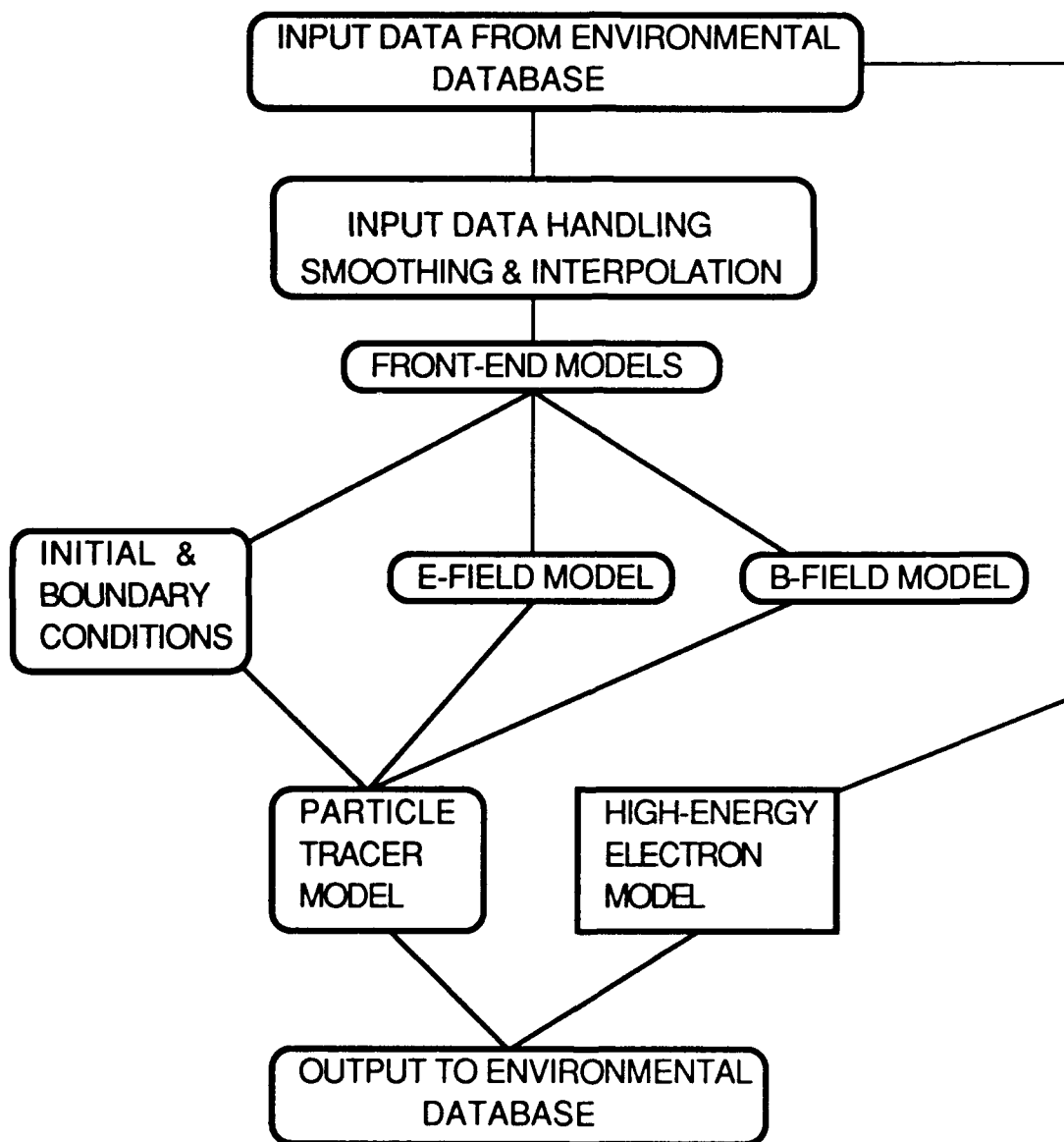


Figure 2.1

MSM Control & Data Flow Diagram

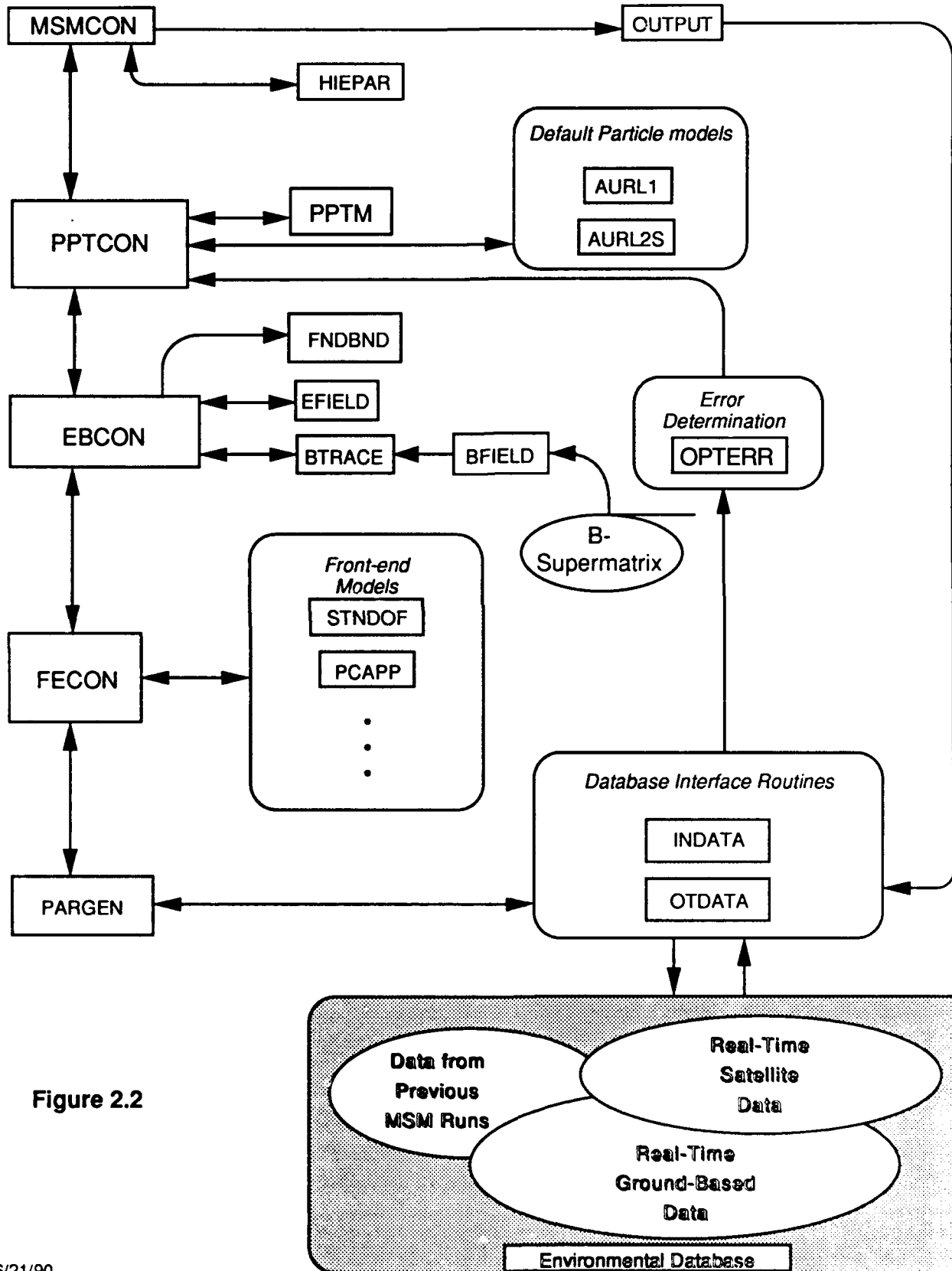


Figure 2.2

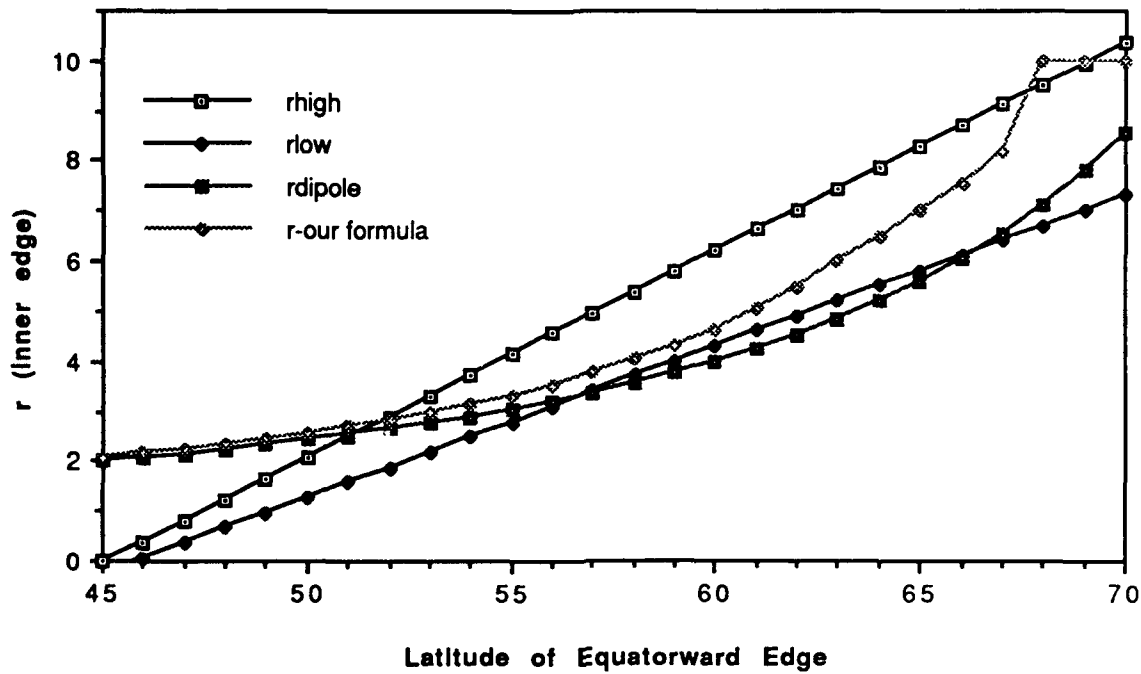


Figure 2.3-1. Formulas relating the equatorial distance of the inner edge of the plasma sheet at local midnight to the latitude of the equatorward edge of the aurora at local midnight. The curves marked r -high and r -low represent and upper lower envelope of a set of estimates derived from the papers by [Horwitz, 1986 #9; Kivelson, 1976 #8; Gussenhoven, 1983 #3]. The curve marked r_{dipole} represents mapping in a simple dipole field, and the curve marked r -our formula represents the result of applying equation (2.3.1).

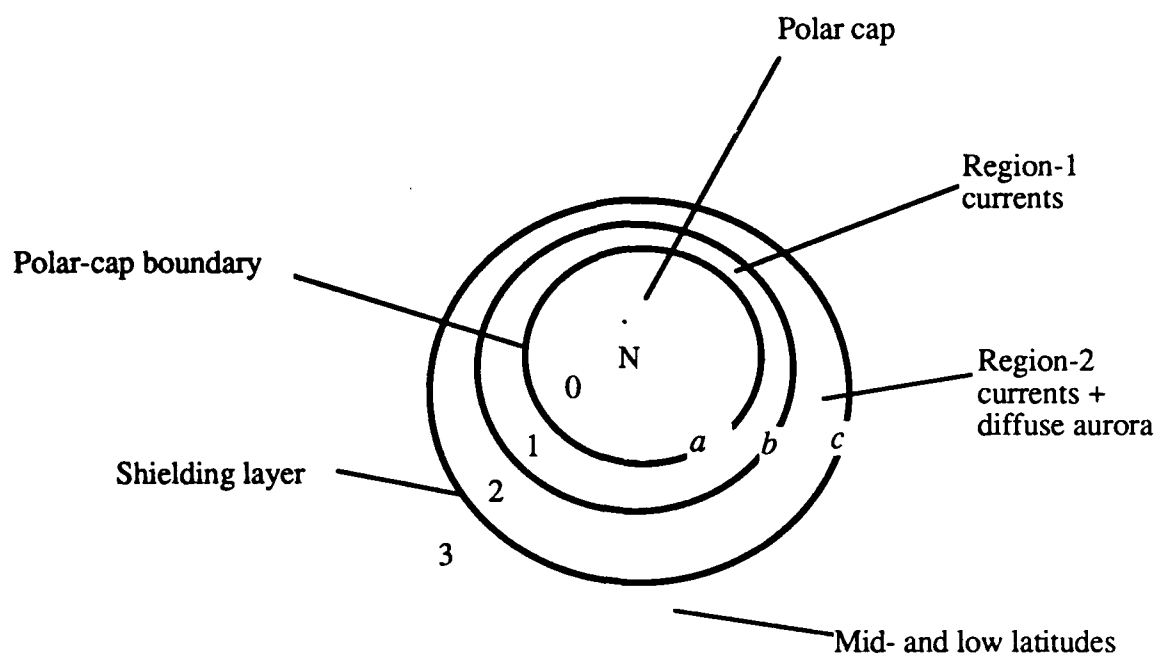


Figure 2.4-1. Division of the ionosphere into four regions for the electric-field model.

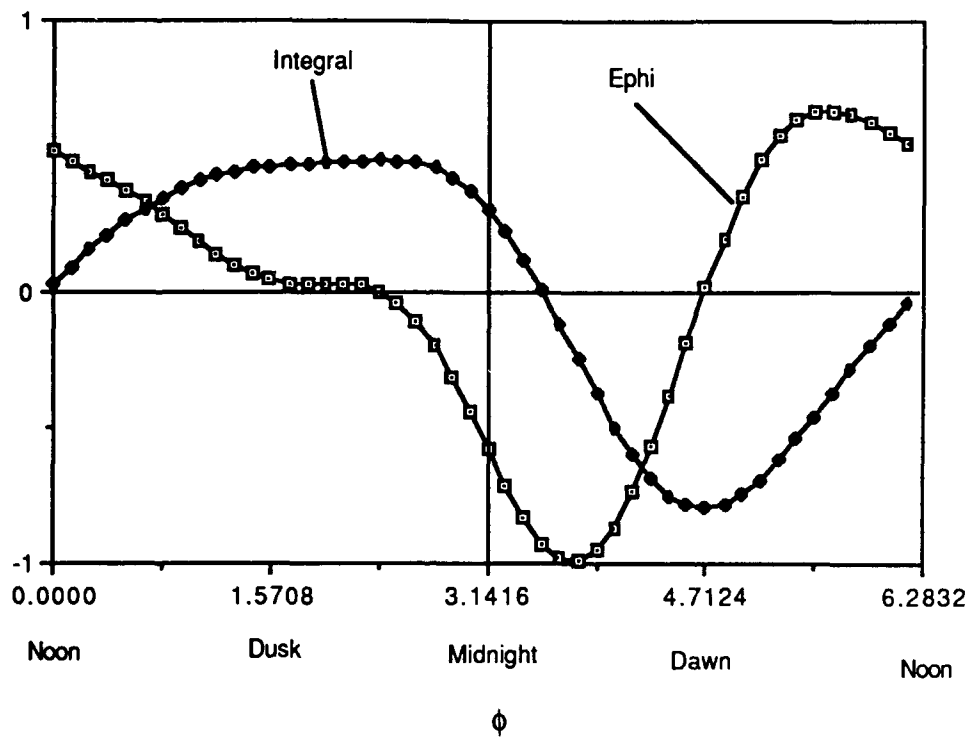


Figure 2.4-1. The assumed variation of E_ϕ with ϕ in the low-latitude region of the electric-field model, with the minimum value normalized to -1, and the normalized indefinite integral of E_ϕ , as indicated in equation (2.4-20).

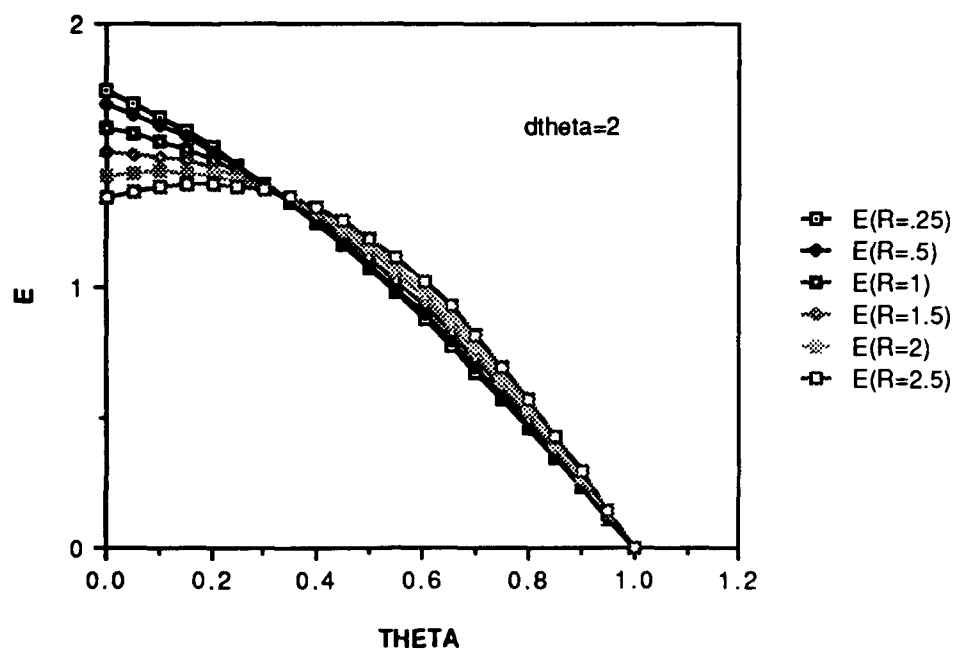


Figure 2.4-2. Plots of meridional electric fields based on equations (2.4-29)-(2.4-31). The top plot pertains to $\Delta\theta = 0.5$, the lower plot to $\Delta\theta = 2.0$.

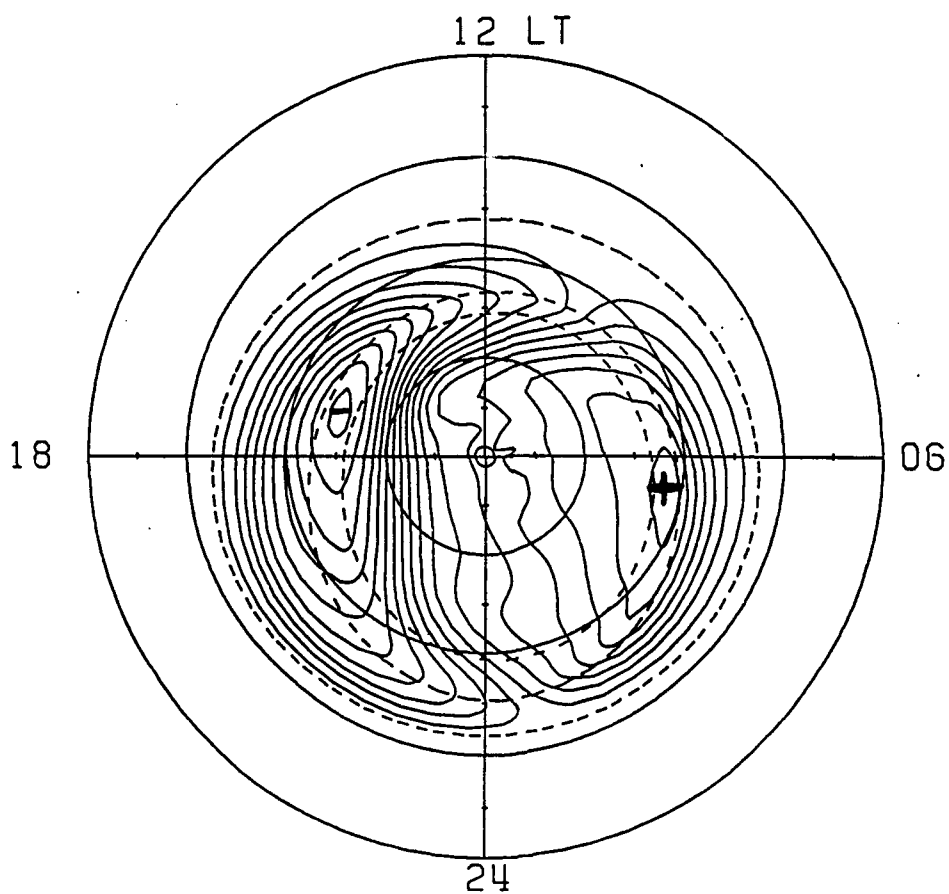


Figure 2.4-3. Equipotential diagram computed for 2345 UT on April 21, 1988. The view is of the northern ionosphere, with noon toward the top of the diagram. There is a 6 kV potential difference between adjacent equipotentials.

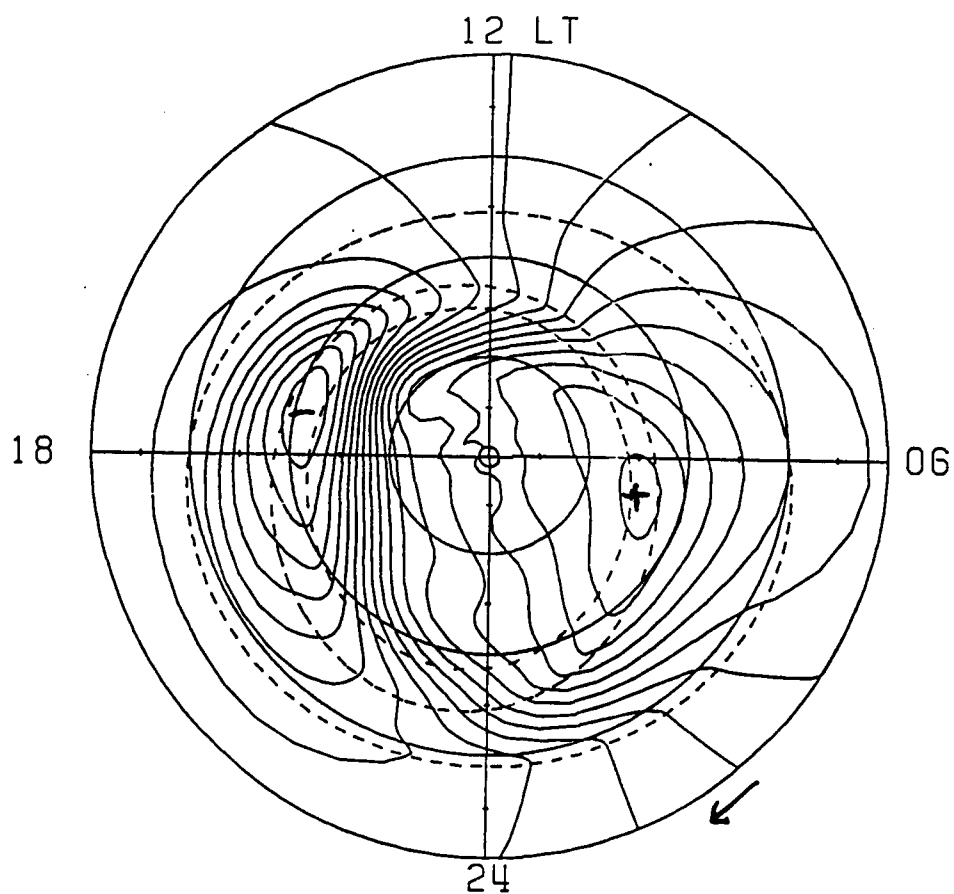


Figure 2.4-4. Equipotential diagram computed for 0045 UT on April 22, 1988. The view is of the northern ionosphere, with noon toward the top of the diagram. There is a 6 kV potential difference between adjacent equipotentials.

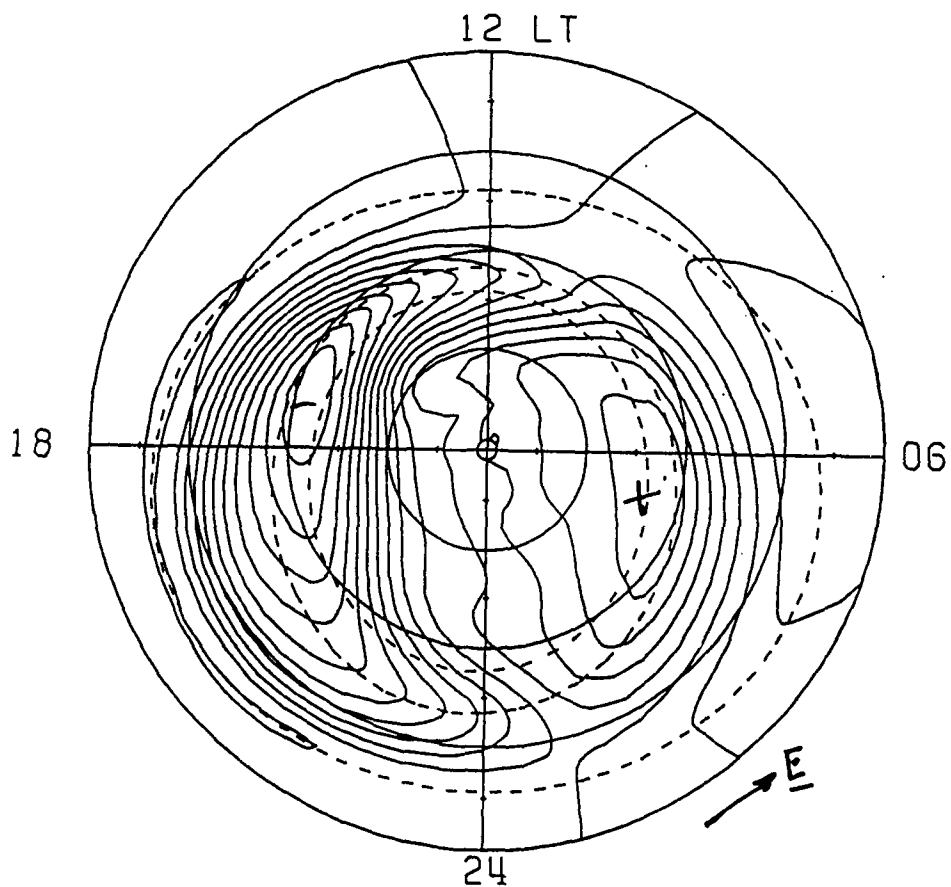


Figure 2.4-5. Equipotential diagram computed for 0300 UT on April 22, 1988. The view is of the northern ionosphere, with noon toward the top of the diagram. There is a 6 kV potential difference between adjacent equipotentials.

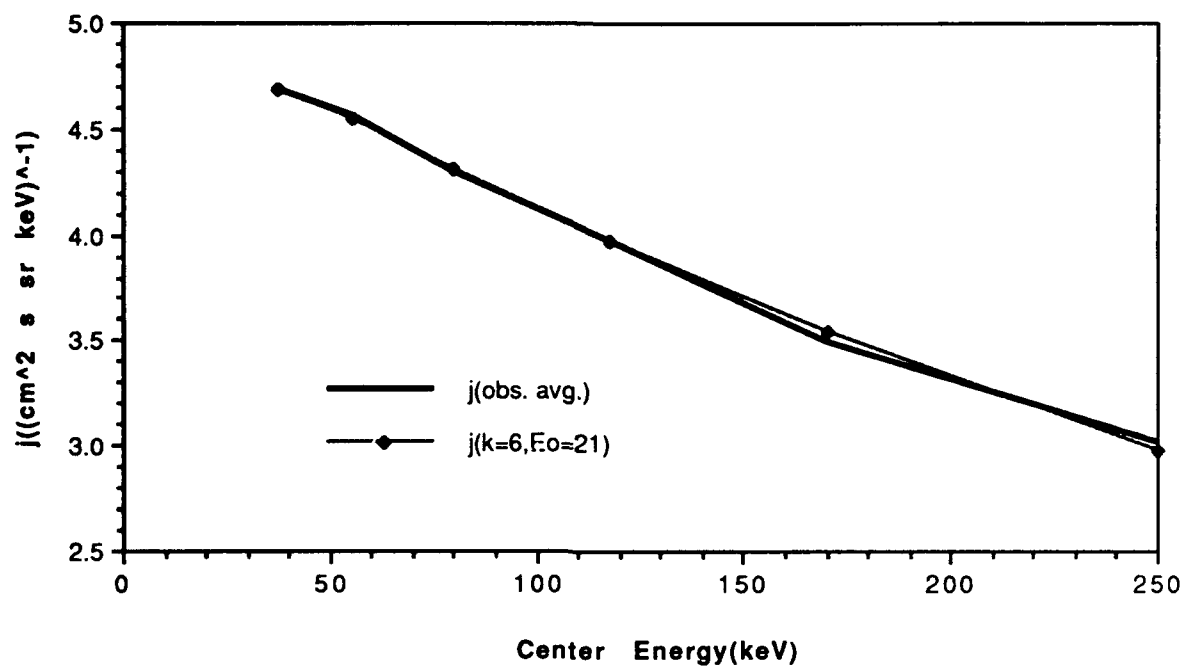


Figure 2.5-1. Observational-average and kappa-function geosynchronous-orbit electron fluxes for quiet, pre-substorm conditions. The sources of observational data are given in Table 2.5-3.

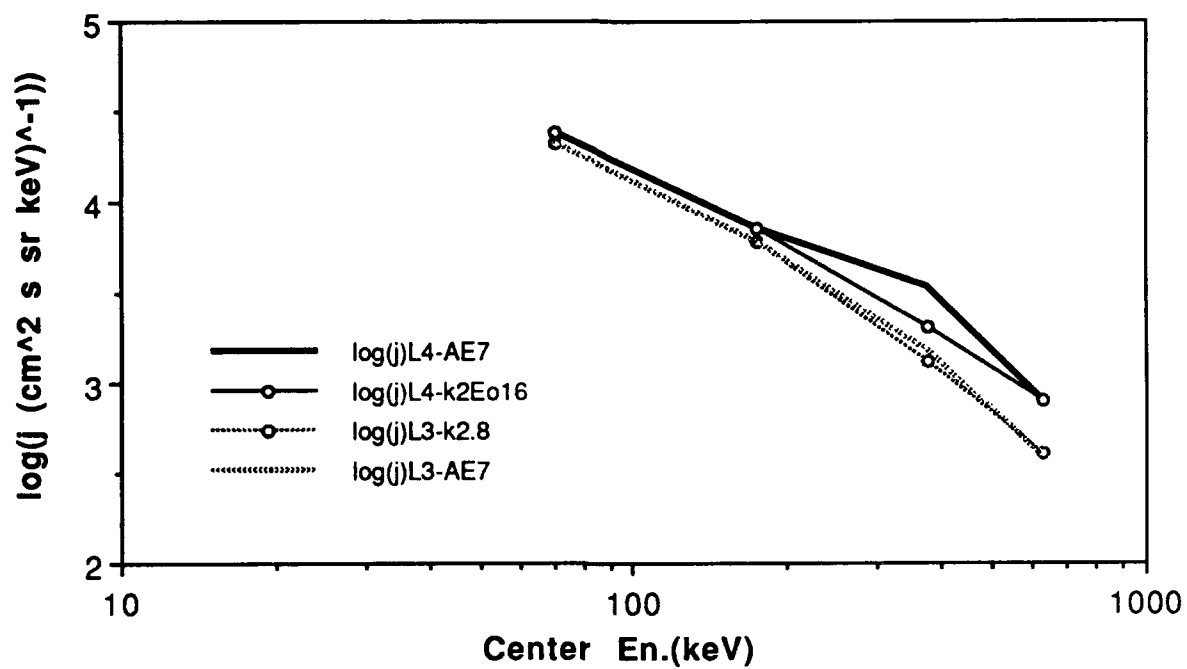


Figure 2.5-2. Flux values for $L = 3$ and 4 derived from NASA Model AE7, and our fitting kappa functions.

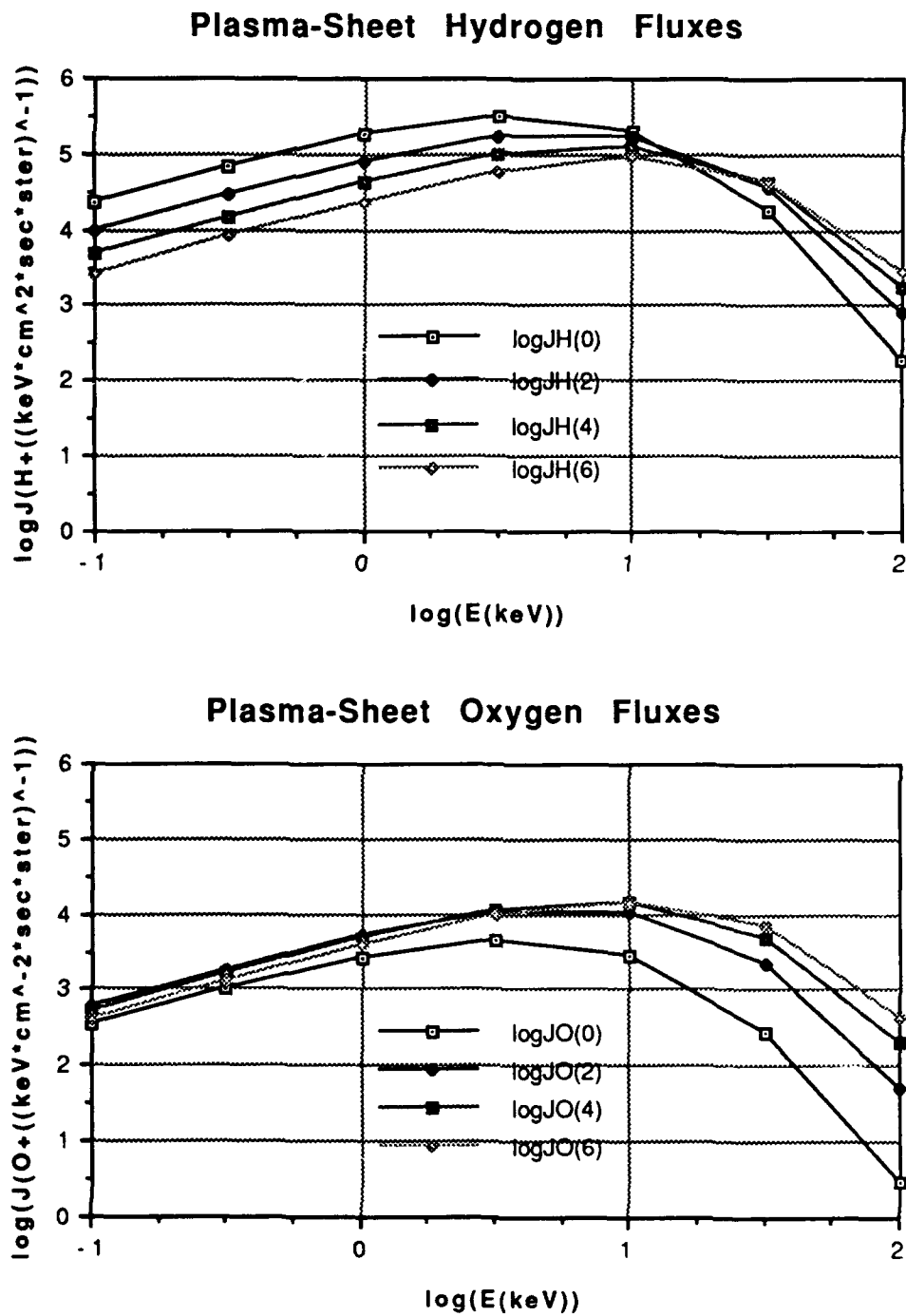


Figure 2.5-3. Fluxes j_{Kp} of plasma-sheet hydrogen and oxygen ions.

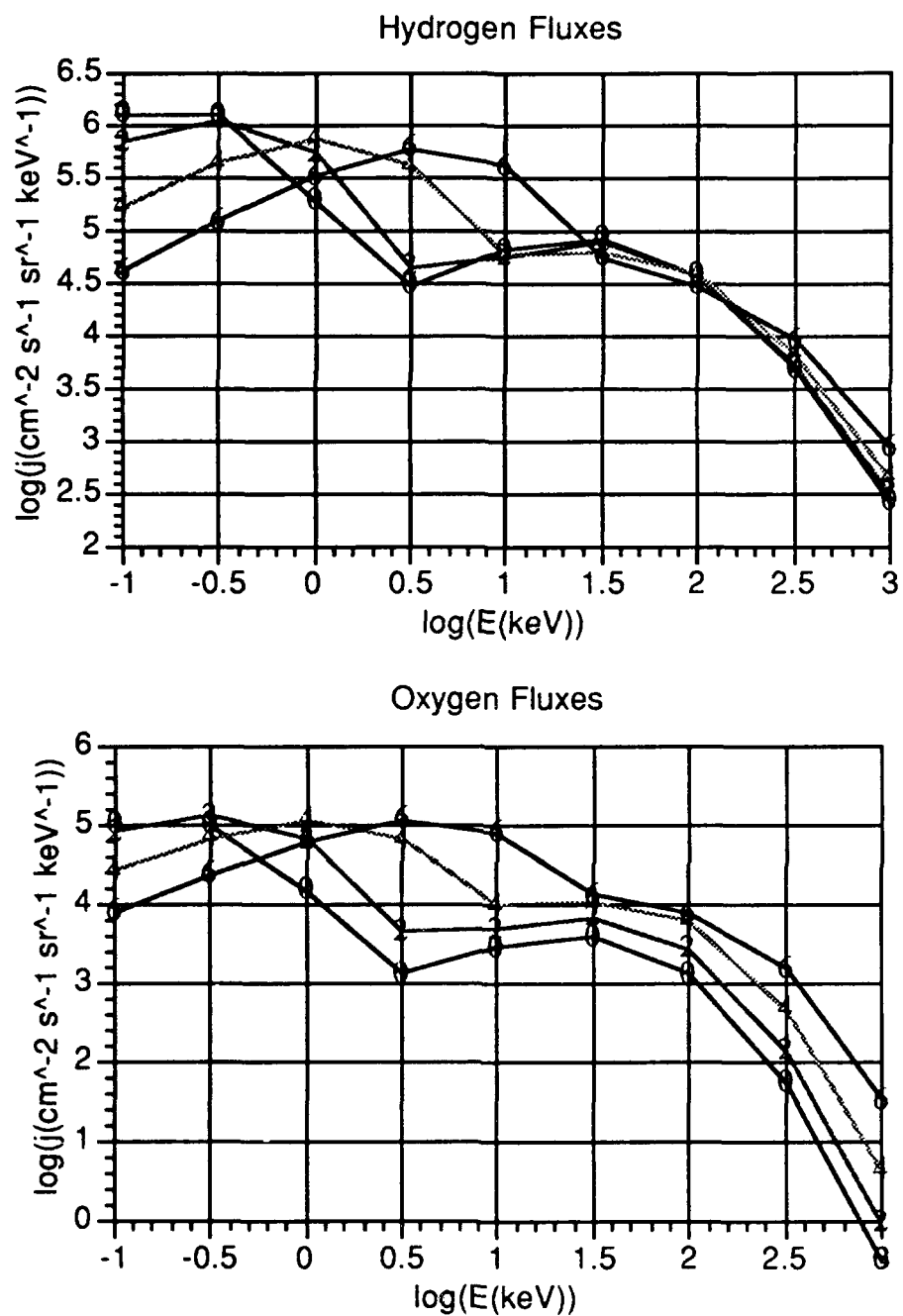


Figure 2.5-4. Hydrogen and oxygen fluxes, as represented in j_{Kp} , for geosynchronous orbit.

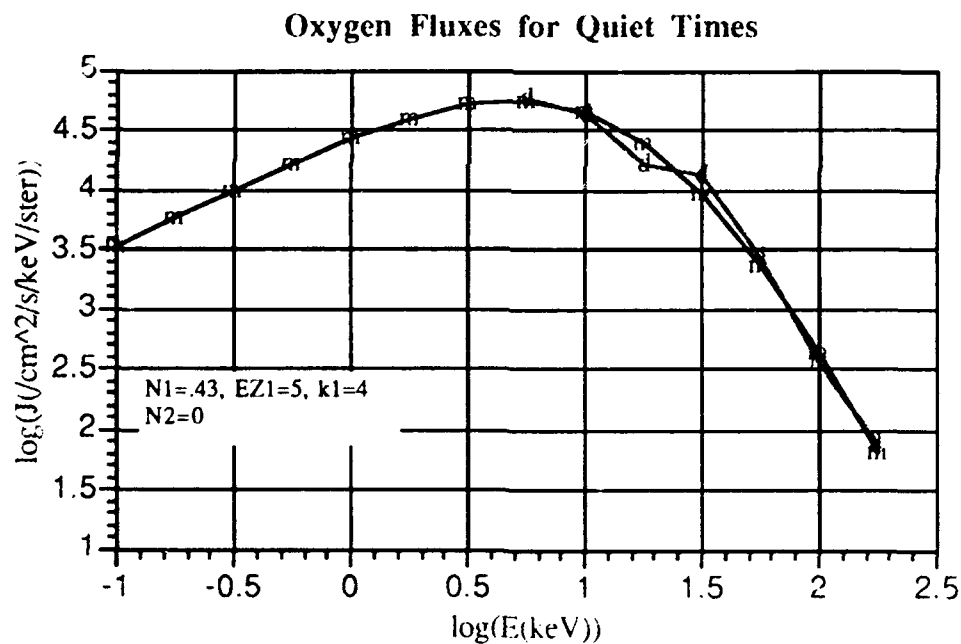
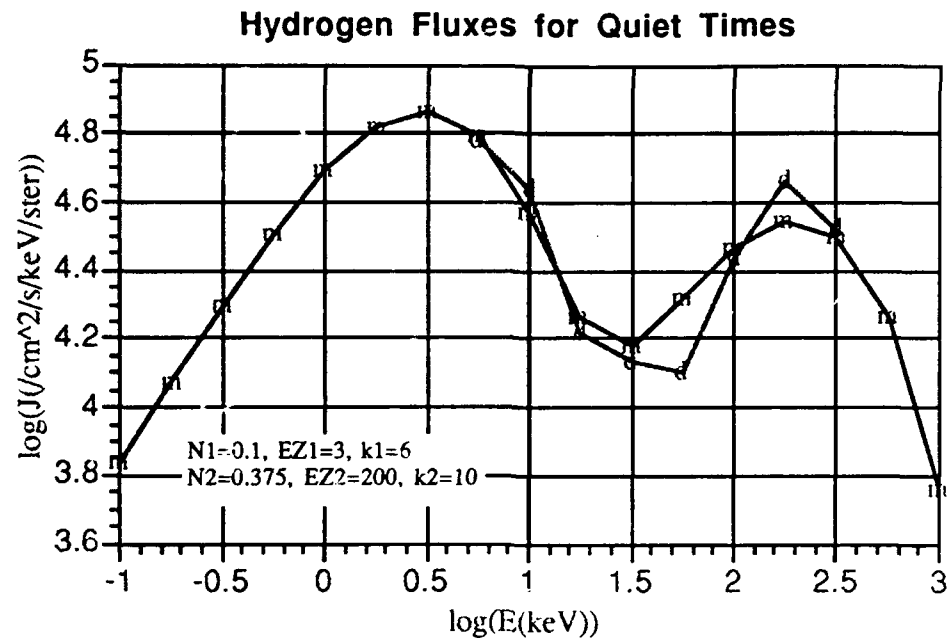


Figure 2.5-5. Fit of model fluxes (m) to observational data (d) for quiet times. The data was scaled from Figure 9a of [Gloeckler, 1987 #23].

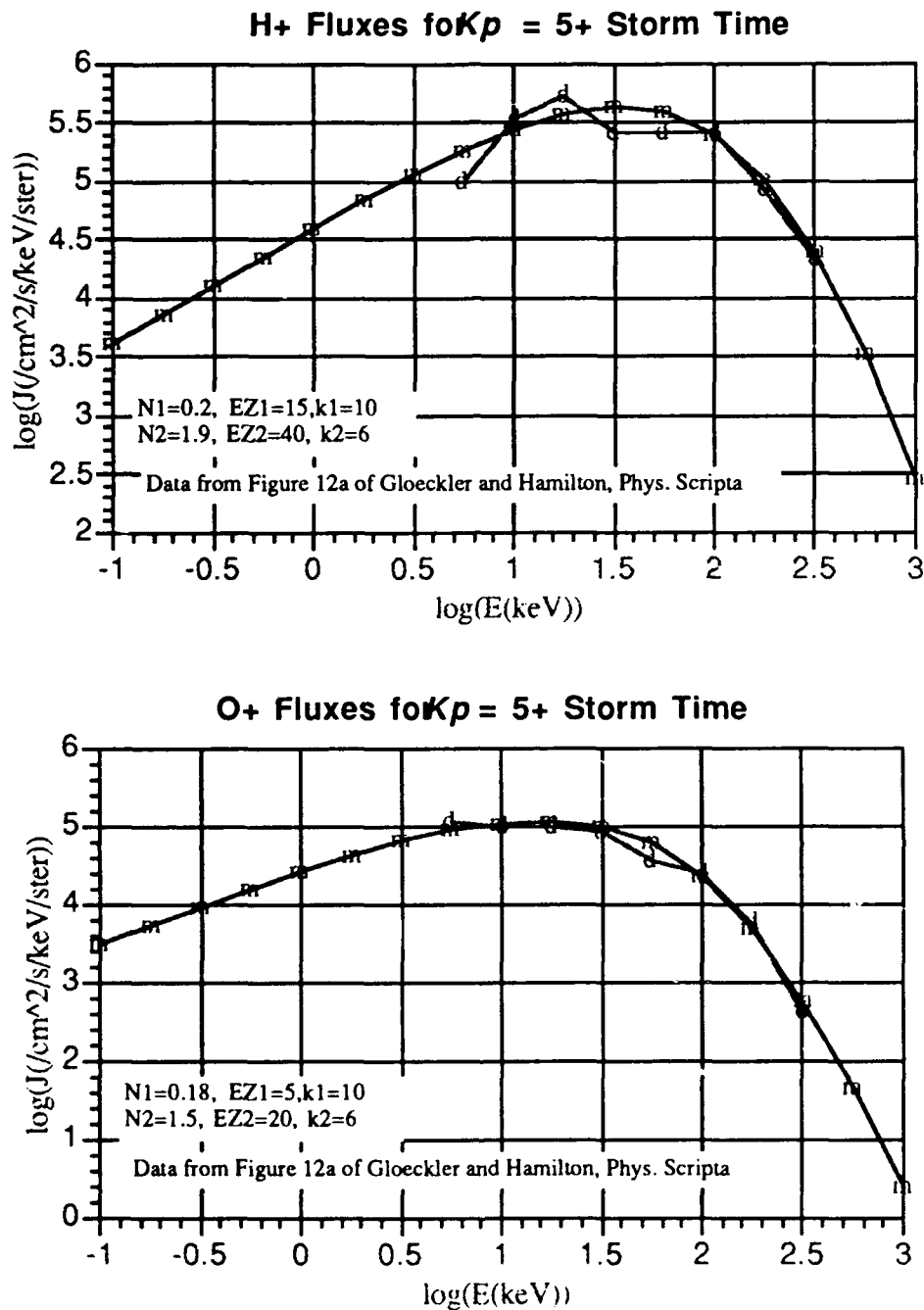


Figure 2.5-6. Fit of model fluxes (m) to observational data (d) for an inbound AMPTE pass that occurred early in the day September 5, 1984. The data source was Figure 12a of [Gloeckler, 1987 #23]. Kp at this time was 5+.

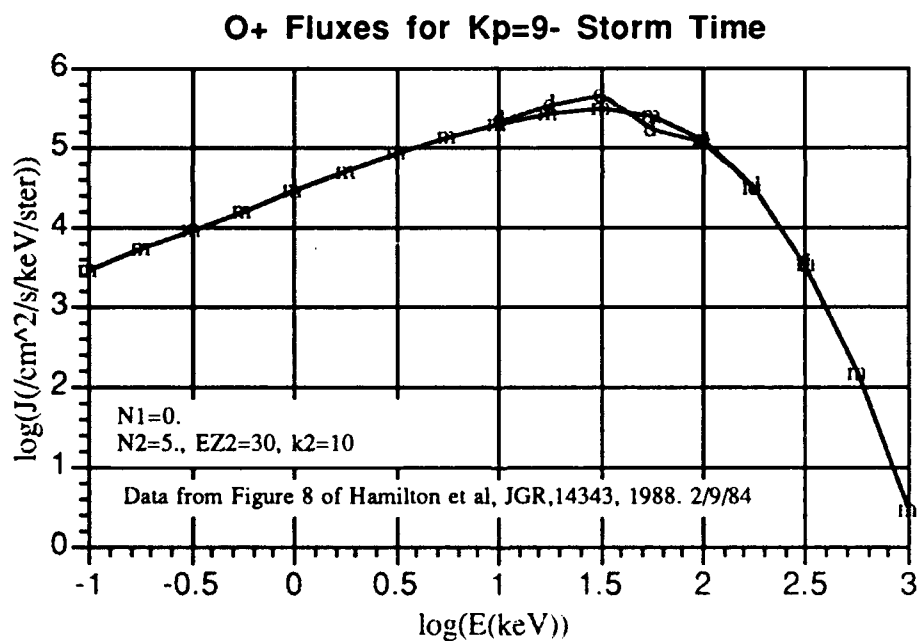
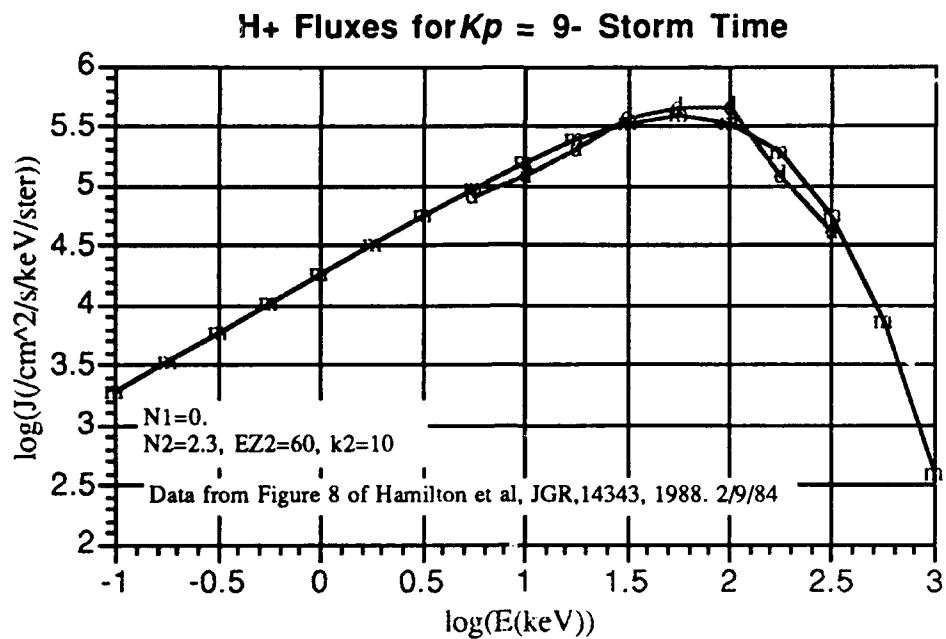


Figure 2.5-7. Fit of model fluxes (m) to observational data (d) for an inbound AMPTE pass that occurred early on February 9, 1986. The data source was Figure 8a of [Hamilton, 1988 #24]. K_p at this time was 9-.

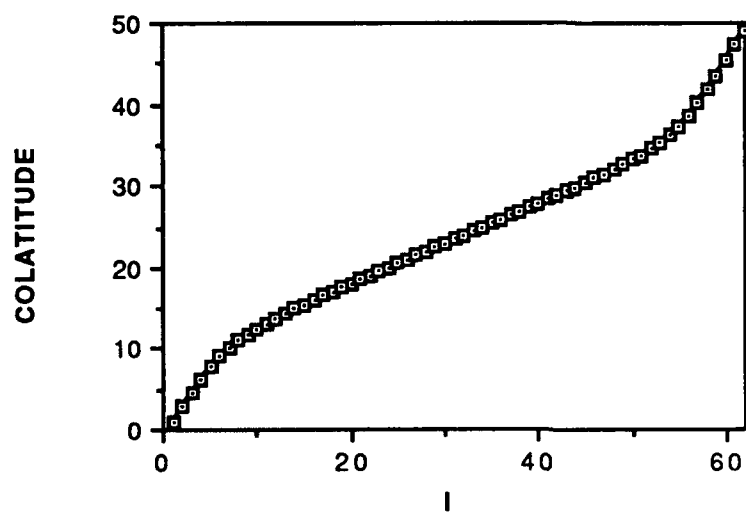


Figure 2.6-1. Grid colatitude vs. grid index I .

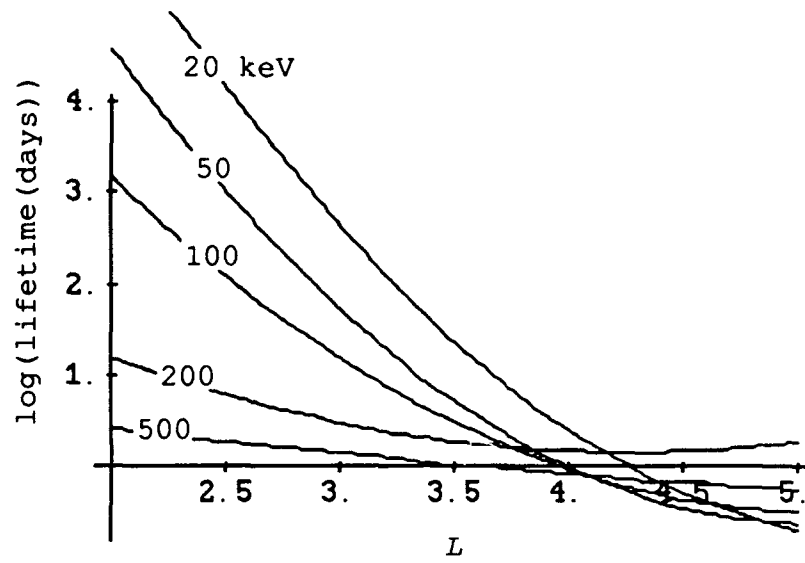


Figure 2.6-2. Lifetimes computed from our analytic representation of Lyons' results.

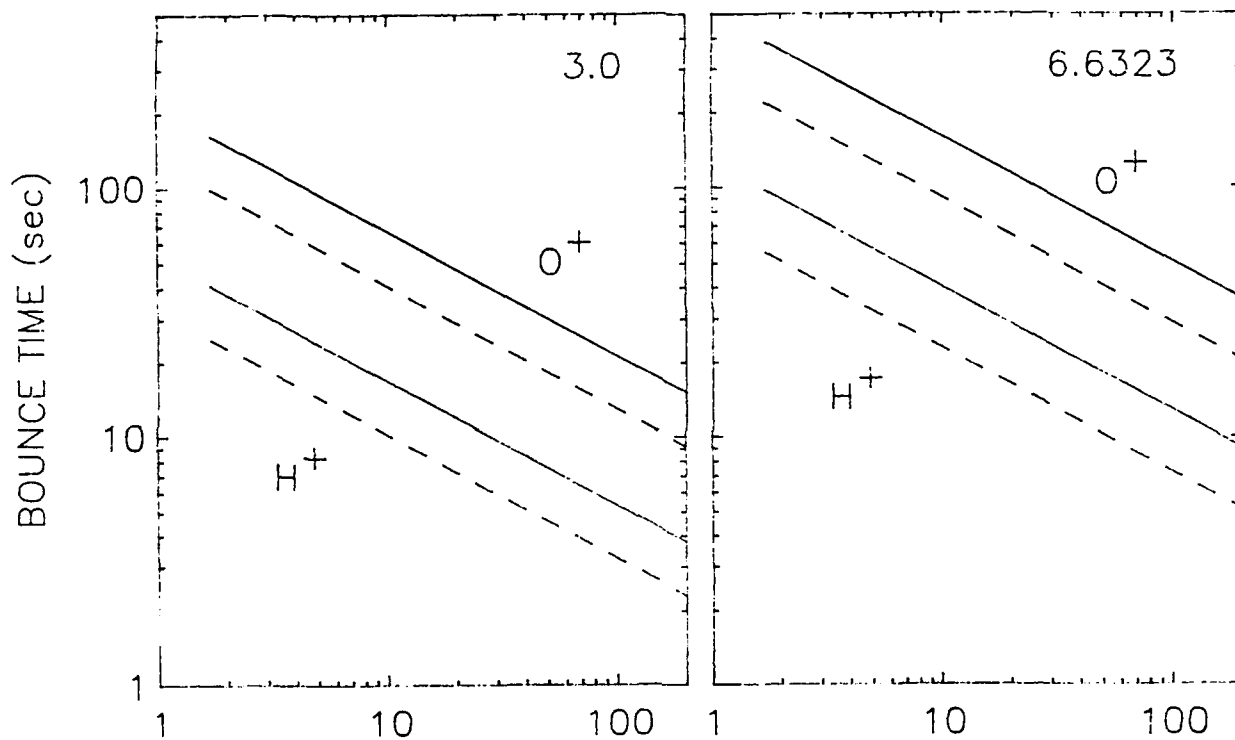


Figure 2.6-3. Quarter-bounce times for H^+ and O^+ as functions of energy for the indicated L -values (r_{eq}). Solid curves denote times for pitch angles very near the loss cone, while dashed curves are for particles mirroring very near the equatorial plane. The loss cone has been taken to be defined by the planet surface (dipole magnetic field).

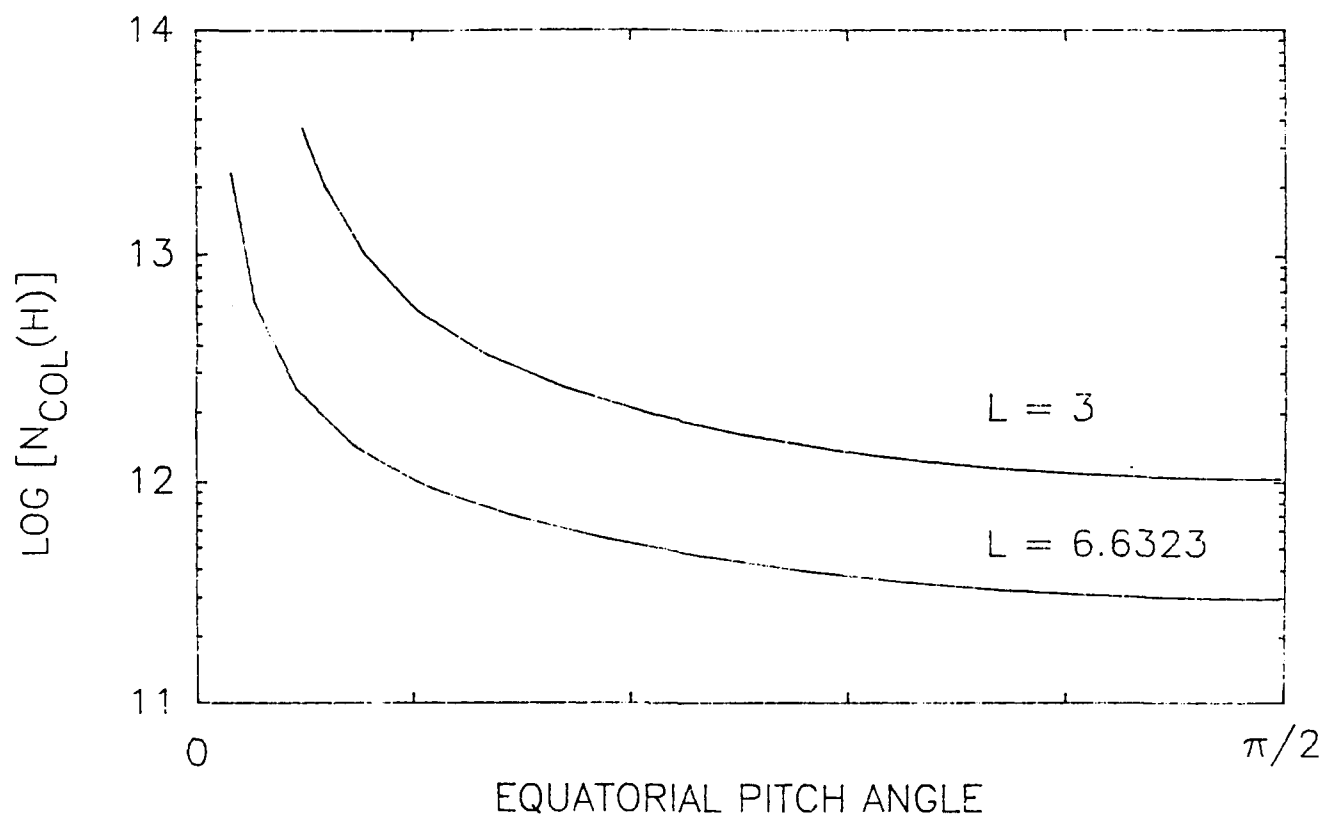


Figure 2.6-4. $N_B(r_{eq}, \alpha_{eq})$ results for $r_{eq} = 3.0 R_E$ and $6.6323 R_E$ as a function of equatorial pitch angle. The loss cone is defined by the planet surface. The exobase temperature in these calculations has been taken to be 1000°K and the exobase density $8.0 \times 10^4 \text{ cm}^{-3}$.

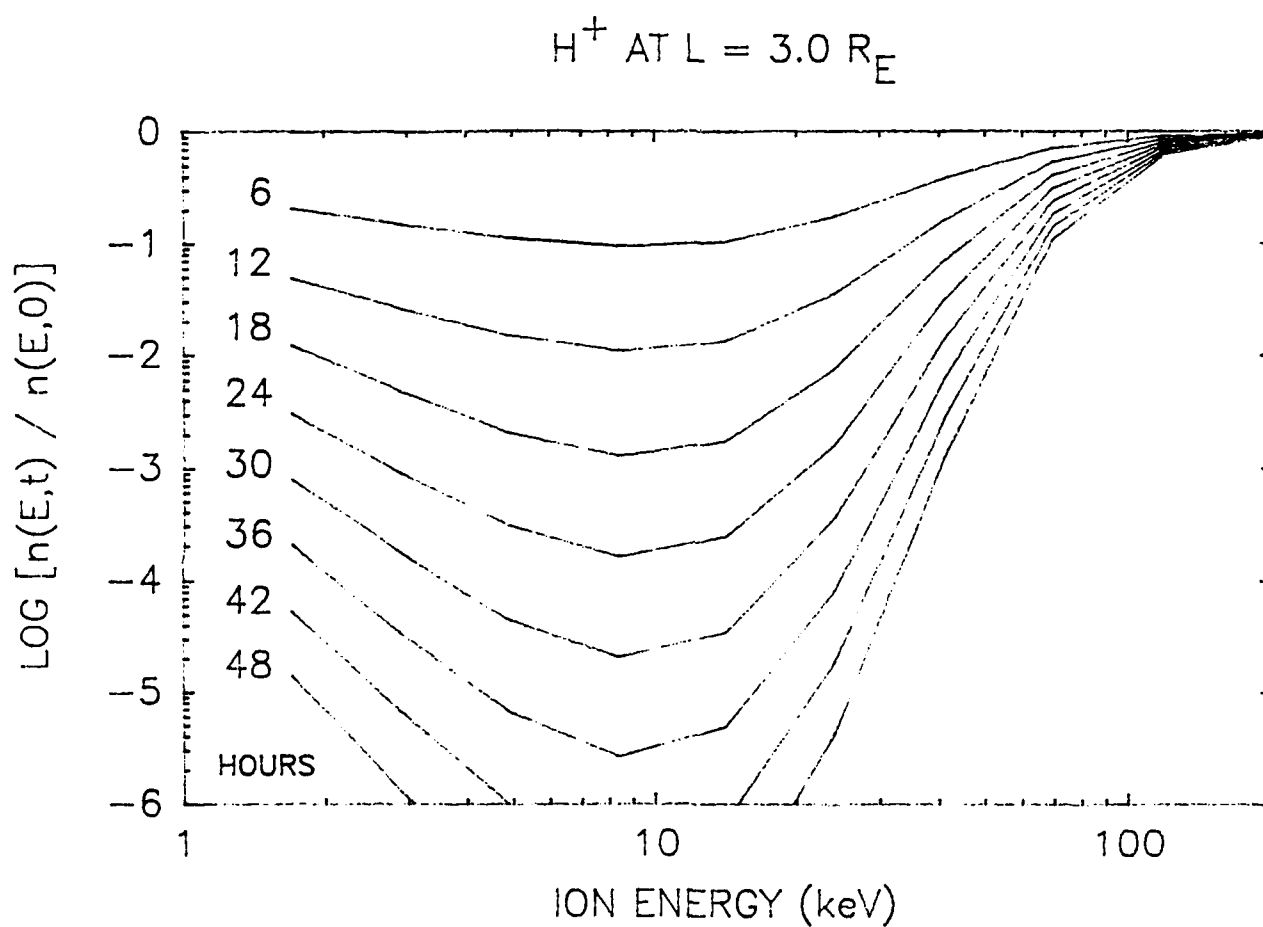


Figure 2.6-5. Stationary-case decay (erosion) of ring current ions is illustrated as a function of particle energy by plotting the pitch-angle integrated KDF -- denoted $n(E,t)$ -- at six-hour intervals, normalized by $n(E,0)$. The loss cone is defined by the planet surface, the exobase temperature is 1000°K , and the exobase density is $8.0 \times 10^4 \text{cm}^{-3}$. (a) H^+ at $3.0 R_E$.

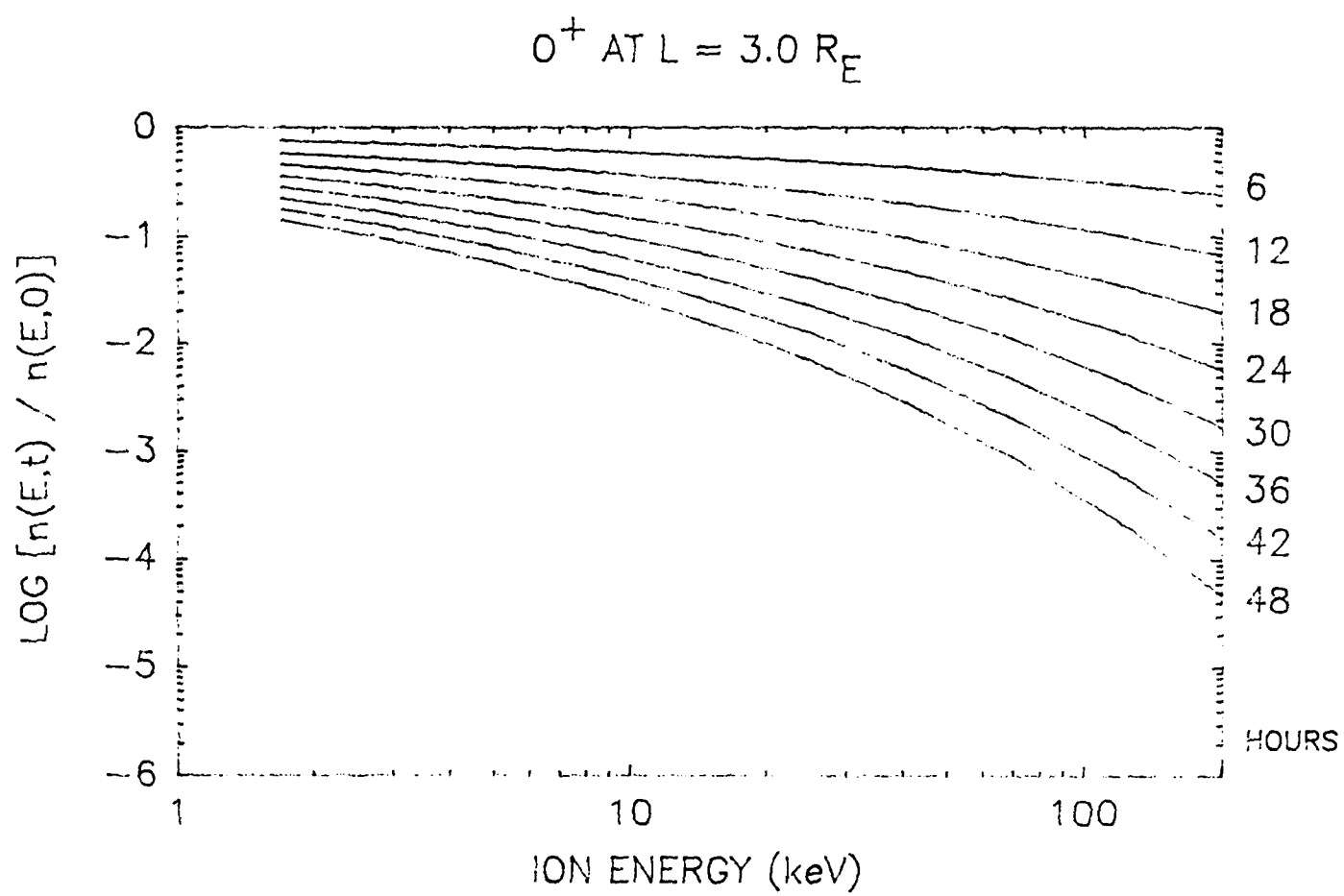


Figure 2.6-5b. O^+ at $3.0 R_E$.

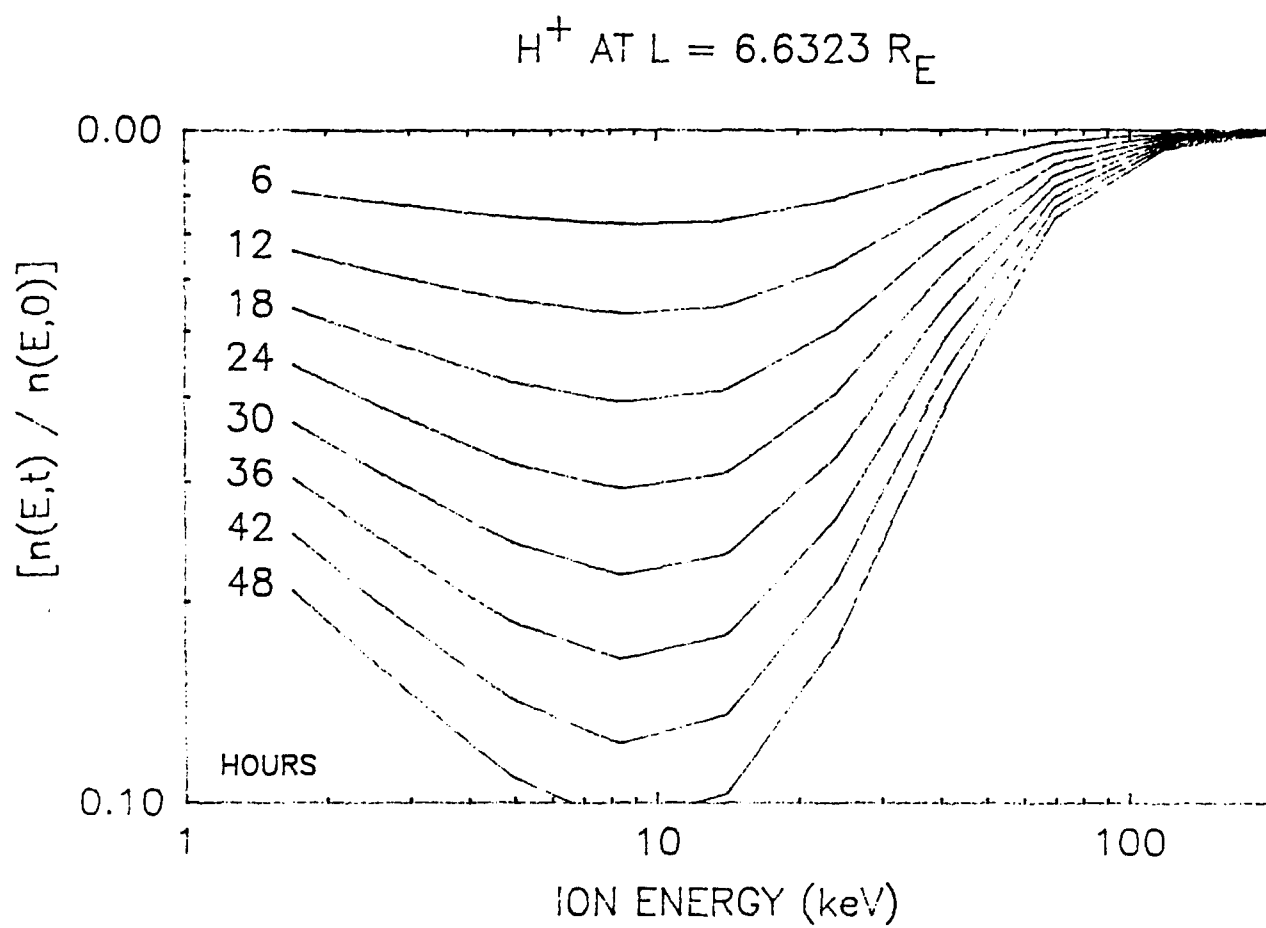


Figure 2.6-5c. H^+ at $6.6323 R_E$. (Note the change in vertical scale.)

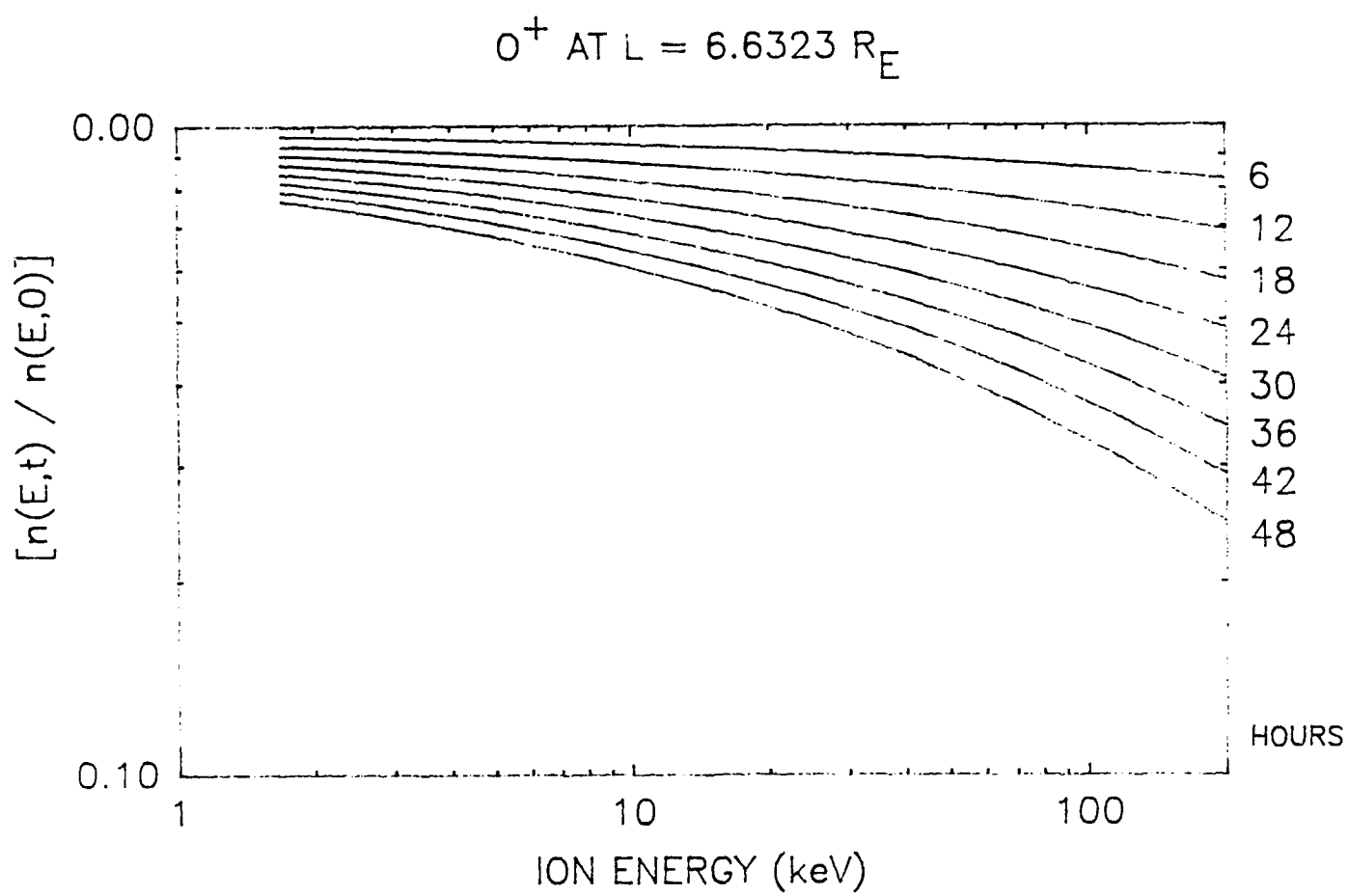


Figure 2.6-5d. O^+ at $6.6323 R_E$.

3. TEST EVENTS: MARCH 22, 1979 AND APRIL 21-23, 1988

3.0. Introduction

The Magnetospheric Specification Model has been tested against two major geomagnetic storm events separated in time by nine years. The first test event occurred on March 22, 1979, about 1 year before the peak of solar cycle 21. This event was chosen because it is a well-documented event (the CDAW 6 event) and a large body of data from a variety of sources was readily available to compare with the model output, however, DMSP ion drift meter data were not available for this event. The second event occurred April 21-23, 1988, about 2 years before the peak of solar cycle 22. The second event was chosen because GL had already begun an investigation of the event and DMSP data were available. In both cases, the choice of events was dictated by the availability of test data. Both events represent important geomagnetic storms.

3.1. The March 22, 1979 Event

The March 22, 1979 event was used about mid-way through the contract. This was before the MSM was developed to the point of fully automated operation. Model time steps and input data were hand tailored for the event. In this respect, it was not a test of the MSM in its delivered version. Moreover, the lack of DMSP ion drift meter data limited the electric field model. For these reasons we will not discuss this event further except to note that the success of the model with this event provided confidence that the basic design of the MSM was valid and formed the basis of the Critical Design Review.

The detailed results of the MSM using this event can be found in Quarterly Status Report nos. 6 and 7 and in Bonnie Hausman's M.S. thesis. This thesis, which contains a good description of the preliminary version of the MSM, is included in the Appendix of this report.

3.2. The April 21-23, 1988 Event

3.2.1 Geophysical Conditions for the Event

As can be seen from figure 3.1, which shows five of the geophysical parameters available as input to the MSM, the April 21-23, 1988 consisted of a large initial substorm, a period of strong but unsteady convection, a quiet period, and then a second large storm almost exactly one day after the start of the first substorm. The standoff distance shown in figure 3.1 was derived from solar wind parameters shown in figure 4.3 and 4.4. The frame labeled Equatorward Edge is the low-latitude boundary of the auroral zone at the midnight meridian as derived from the electron detectors on the DMSP satellites. These data were provided by Bill Denig of GL. Figure 3.2 shows the fluxes obtained by three geostationary spacecraft during the event. These data are from detectors designed and built by the Los Alamos National Laboratory. We had help interpreting the detector sensitivities and geometric factors from Tom Cayton and the staff at LANL.

From figures 3.1 and 3.2, we see that the onset of the first substorm begins shortly before the start of day 113 (April 22nd). It rises to a peak by 0200 hrs on 113 and remains intense until about 1200 hrs. Dst reached its most negative value of -120 nanotesla around 1000 hrs on day 113, indicating that the storm-time ring current peaked at that time. The second large substorm occurs part way into the recovery phase of this storm, at the start of day 114.

3.2.2. Comparison With the MSM Output

In order to study the MSM predicted fluxes in the equatorial plane and to compare these fluxes with the spacecraft data we have prepared an animated video of the MSM output for this event. In this video, the MSM fluxes are color coded and the model output after each 15 minute time step is speeded up under animation. The location of each satellite is superimposed on the magnetospheric equatorial plane in the model output display so it is easy to see where each satellite is throughout the storm.

In the video, as time progresses, the satellites advance around their orbits, and the storm front (the inner edge of the plasma sheet) is seen to intensify, move toward the Earth, and cross the orbit of the satellites. The format of a typical video frame is shown in figure 3.3. The MSM output is shown in the upper left-hand side of the frame. In the model frame, the sun is to the left and the dawn meridian is at the top. The fluxes plotted are 40 KeV electrons. The 30 -44 KeV electron fluxes reported by satellite 1 are shown beside the MSM output on the upper right, and four of the relevant model input parameters are shown at the bottom of the frame. In both the satellite flux frame and the parameter frame below, the time being portrayed by the model output is shown as a dashed vertical line.

The video illustrates very dramatically the success of the MSM at predicting the fluxes observed at satellite #1. Unfortunately it is not practical to include the video with this report so we will instead walk through a sequence of seven frames, consisting of figures 3.3 through 3.9, which illustrate interesting times in the event.

Figure 3.3 illustrates a point in the growth phase of the first substorm. Notice that satellite 1 is midway between the dusk and midnight meridians and, according to the model, and the observations, has not yet seen a flux enhancement. The storm front, as indicated by the orange region, has not yet advanced to the geostationary orbit. The model and the observations agree at this point.

Figure 3.4 shows the situation a short time later, at the substorm onset at the satellite. Note that the MSM now shows satellite 1 right at the edge of the storm front (large flux gradient) as indicated by the proximity of the orange and deep orange regions and the satellite flux graph shows a large flux enhancement about to begin.

Figure 3.5 now shows satellite 1 fully engulfed in the storm-enhanced plasma as seen in both the MSM output and the satellite observed fluxes.

Figure 3.6 shows the peak of the storm as seen by satellite 1 and as predicted perfectly for that satellite by the model.

In figure 3.7, the satellite has moved to the dawn meridian and is heading toward the region of decreasing flux values on the day side of the magnetosphere. The satellite observations already show a low flux value and so the model is somewhat behind.

In figure 3.8, nearly one day has elapsed since the start of the sequence, and we find satellite 1 about to enter a storm front again, this time for the second substorm. Again, the model agrees well with the observations.

Finally, in figure 3.9, we are in the recovery phase of the second substorm. The storm front has receded outside the geostationary orbit. Low fluxes are predicted by the model and observed by satellite 1.

We believe that this sequence of figures provides proof that the MSM does a good job in modeling the timing of flux enhancements. In section 4, we discuss the accuracy of the MSM from a statistical standpoint.

Comparison of the MSM with the other two satellites, for this event, is possible by examination of figures 4.9 through 4.14, in section 4. These figures show the detailed time comparison between the MSM output fluxes, interpolated to the three satellite orbit positions, for 40 KeV and 65 KeV electrons. These figures also have the Garrett model output displayed. Section 4 contains a discussion of these figures and conclusions on the overall accuracy of the MSM.

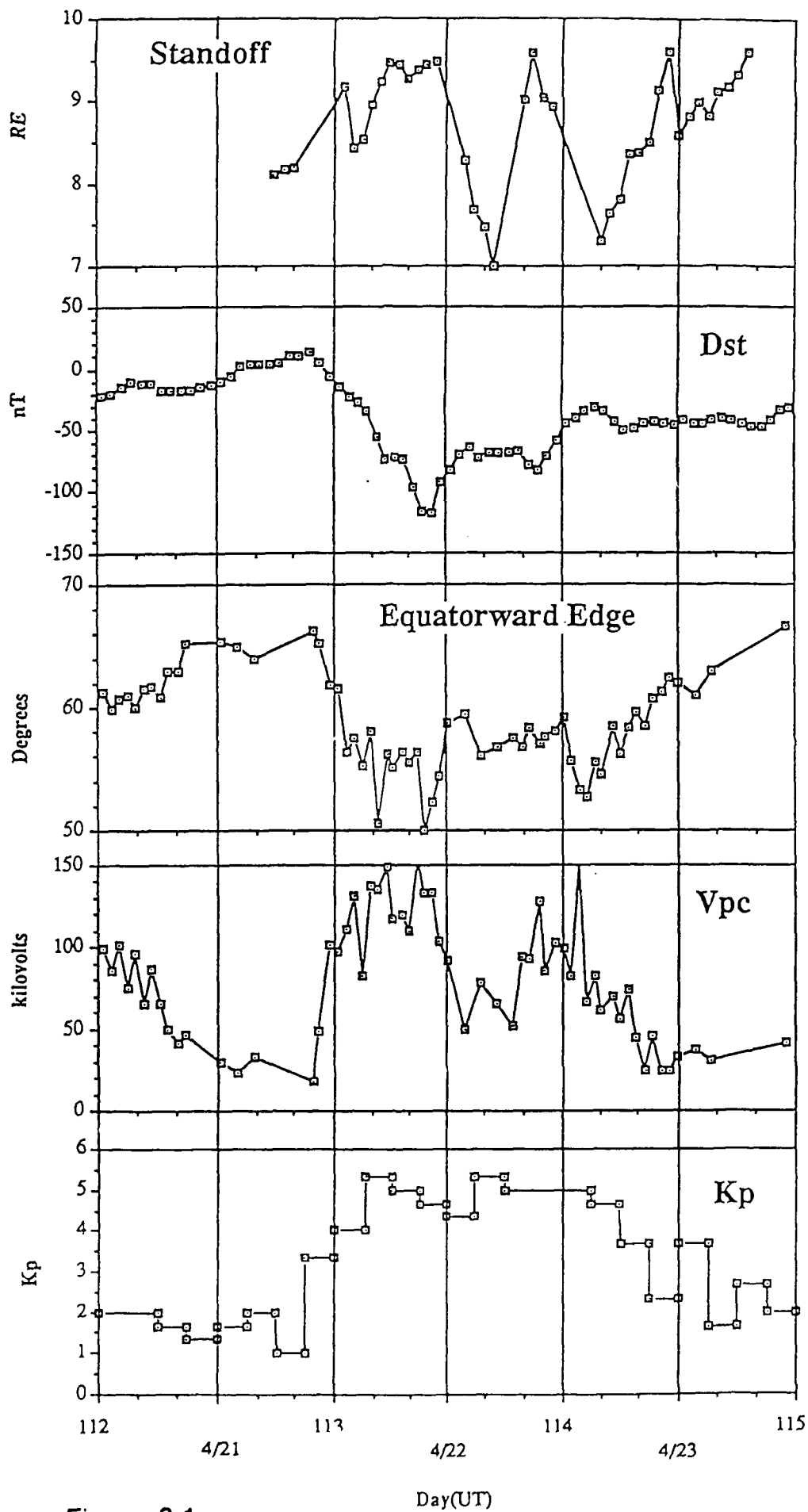


Figure 3.1

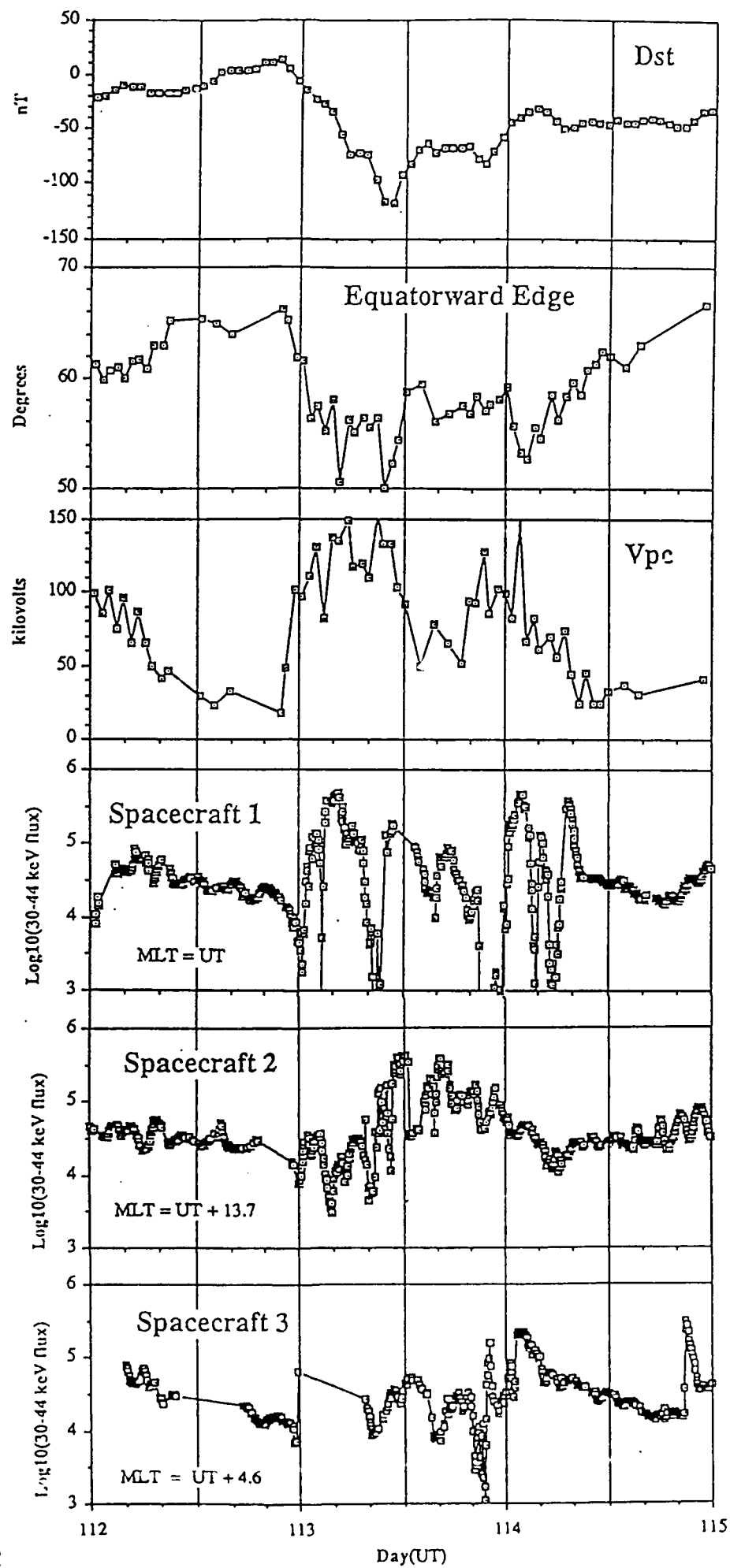


Figure 3.2

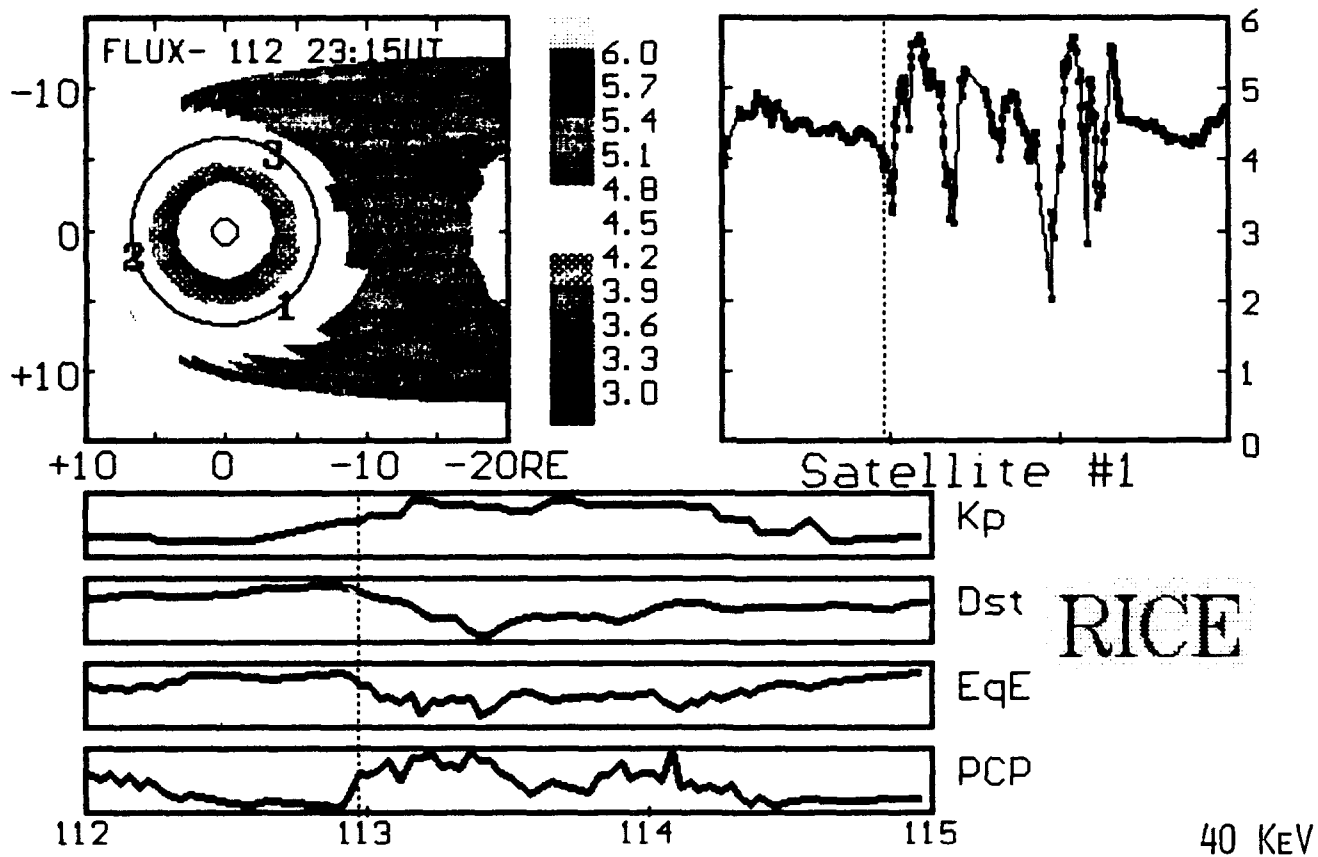


Figure 3.3

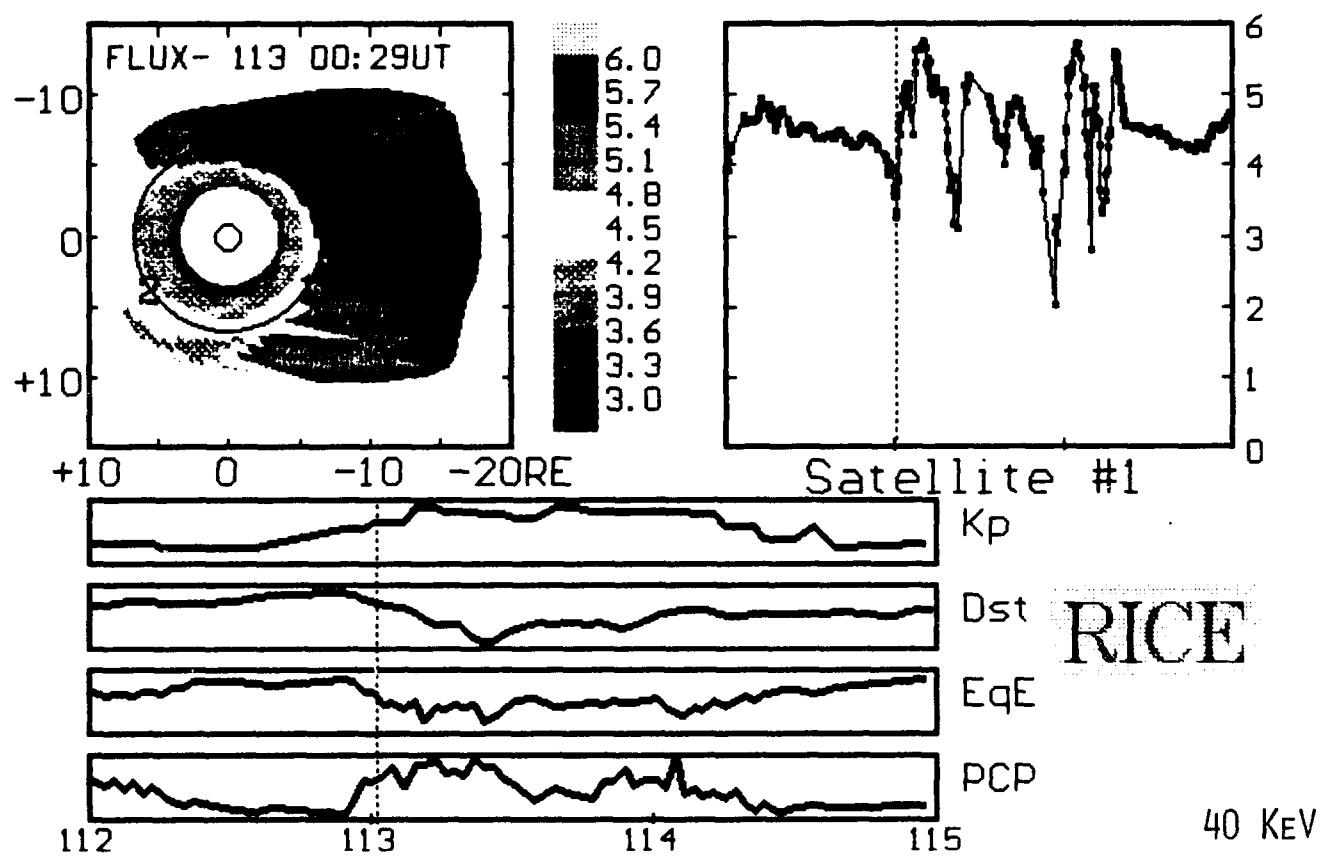


Figure 3.4

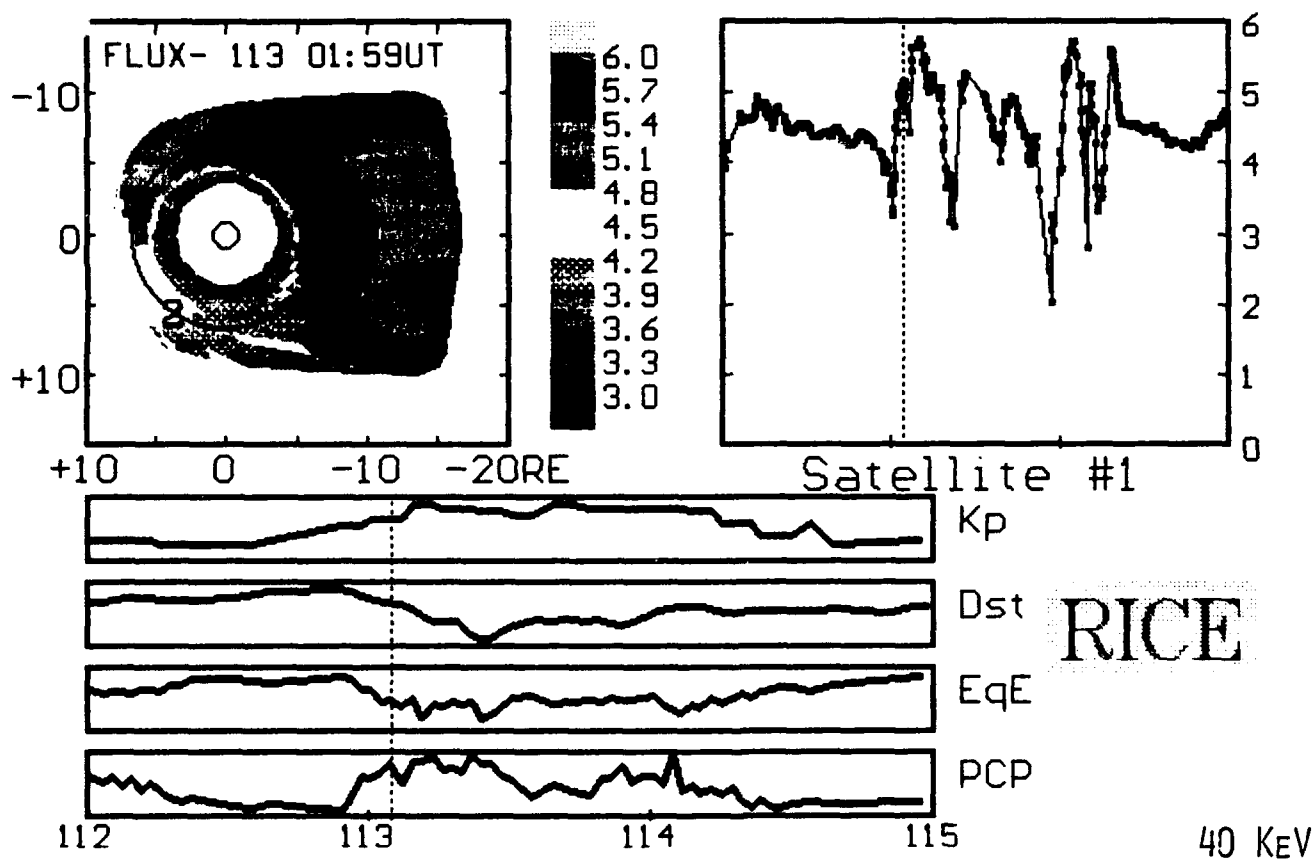


Figure 3.5

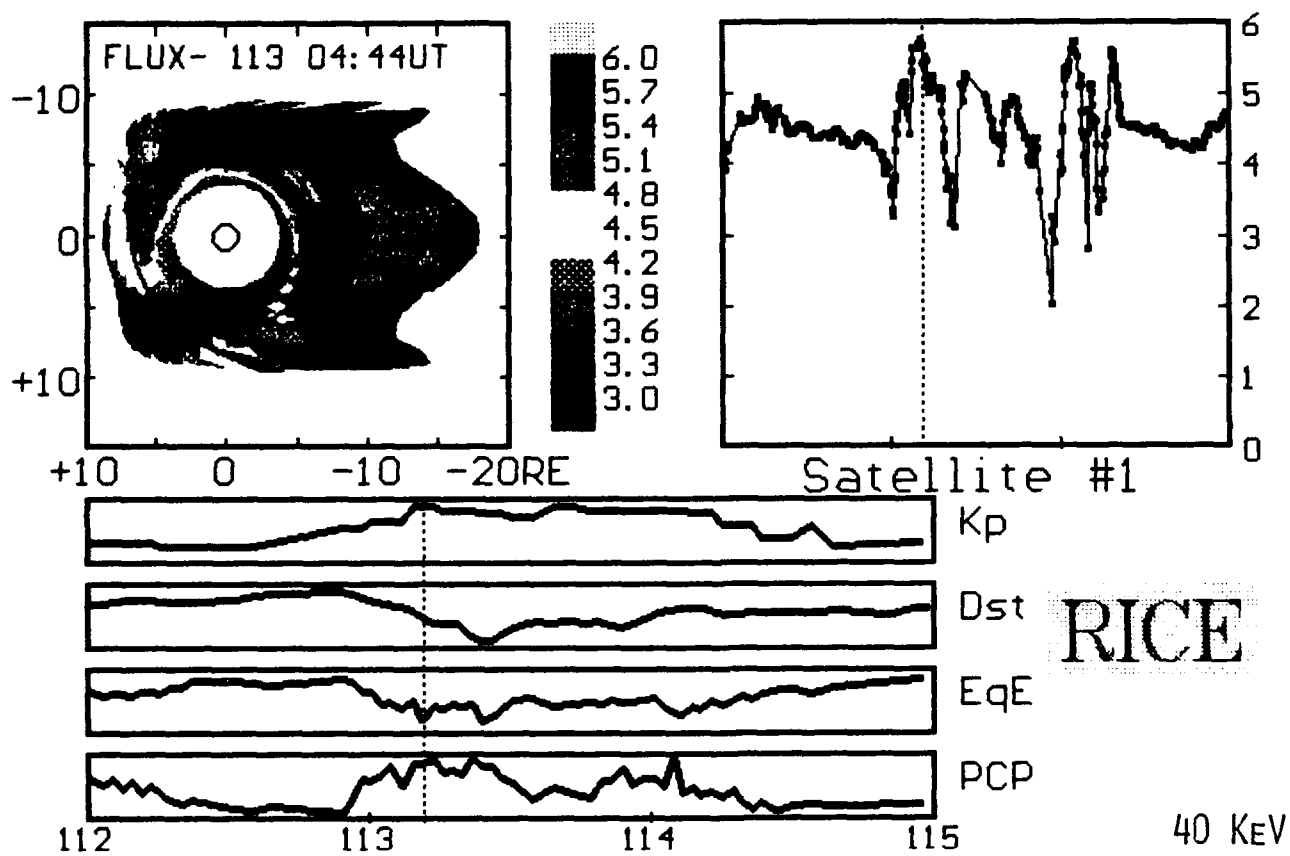


Figure 3.6

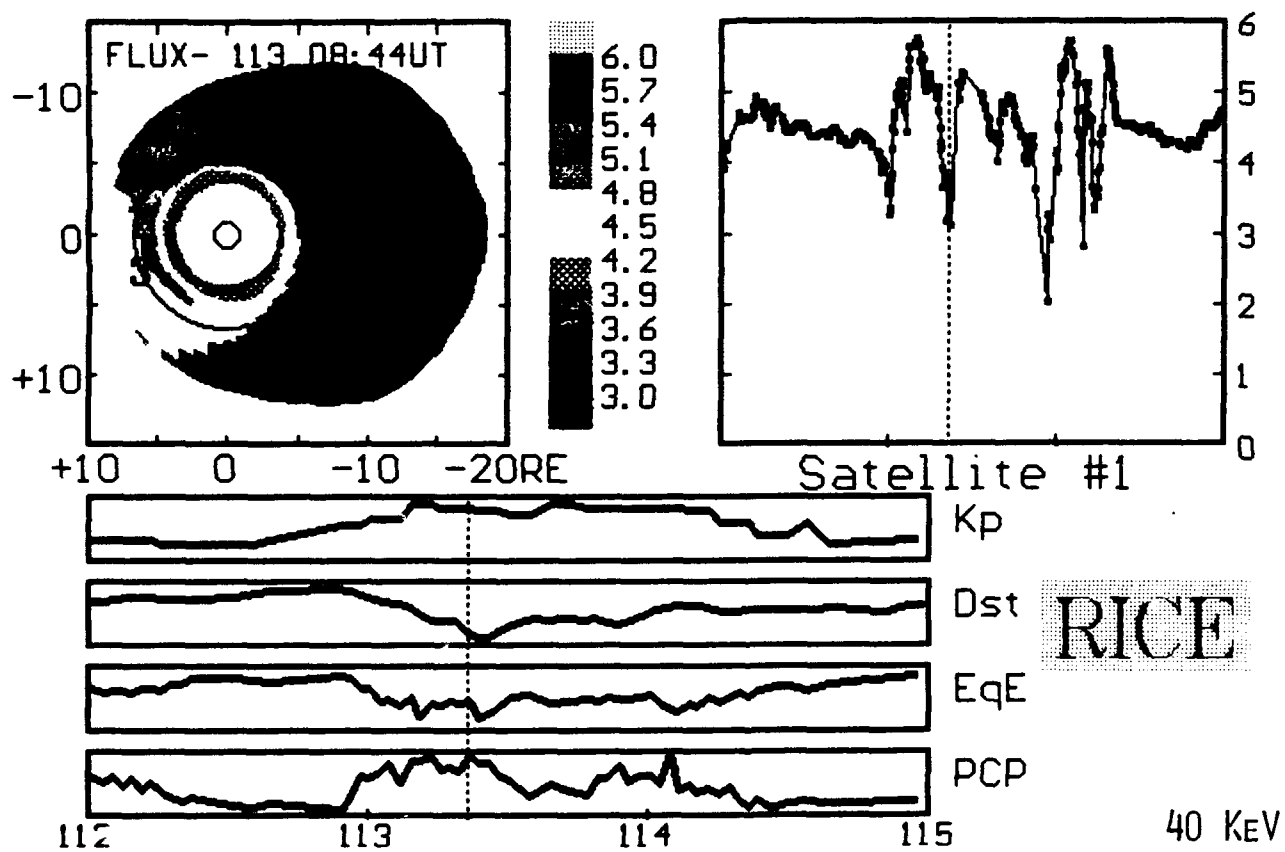


Figure 3.7

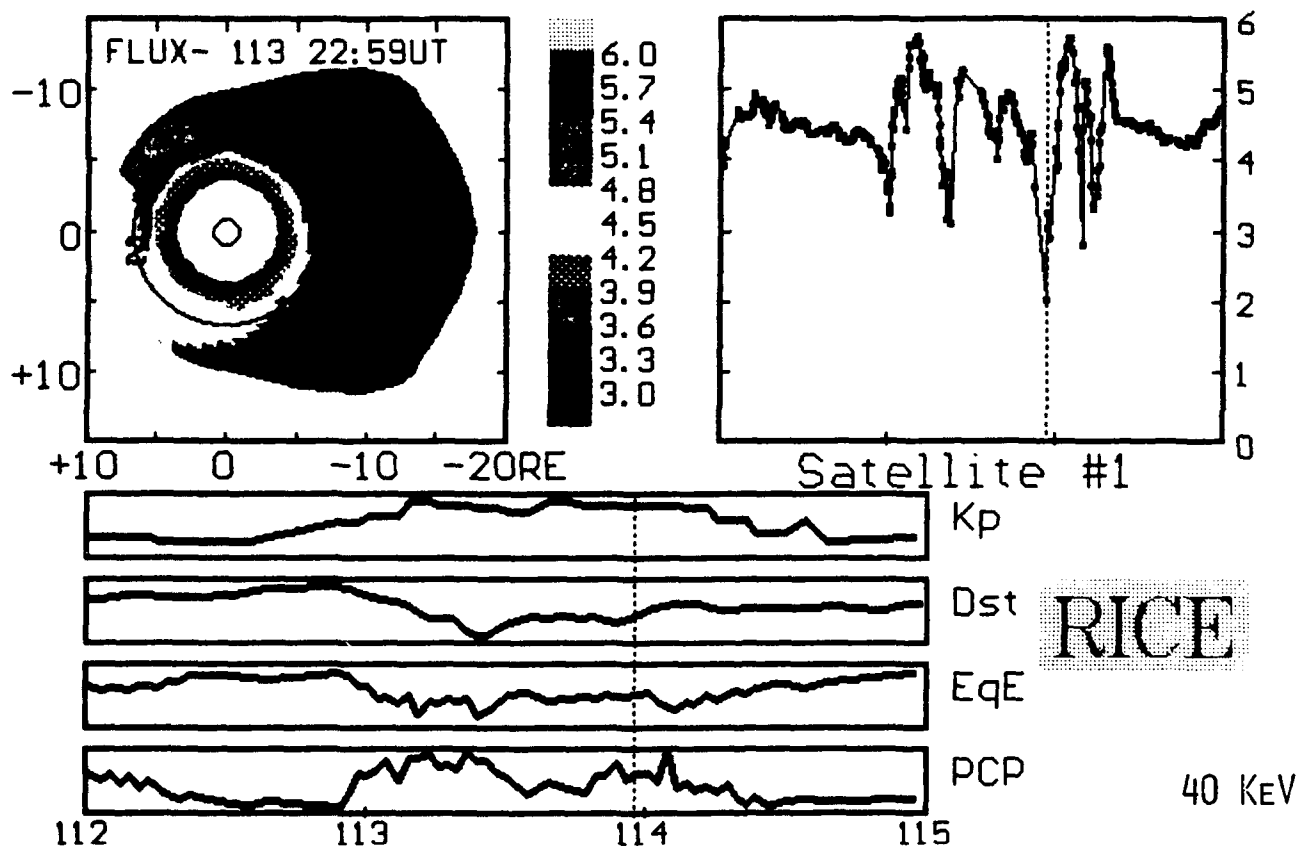


Figure 3.8

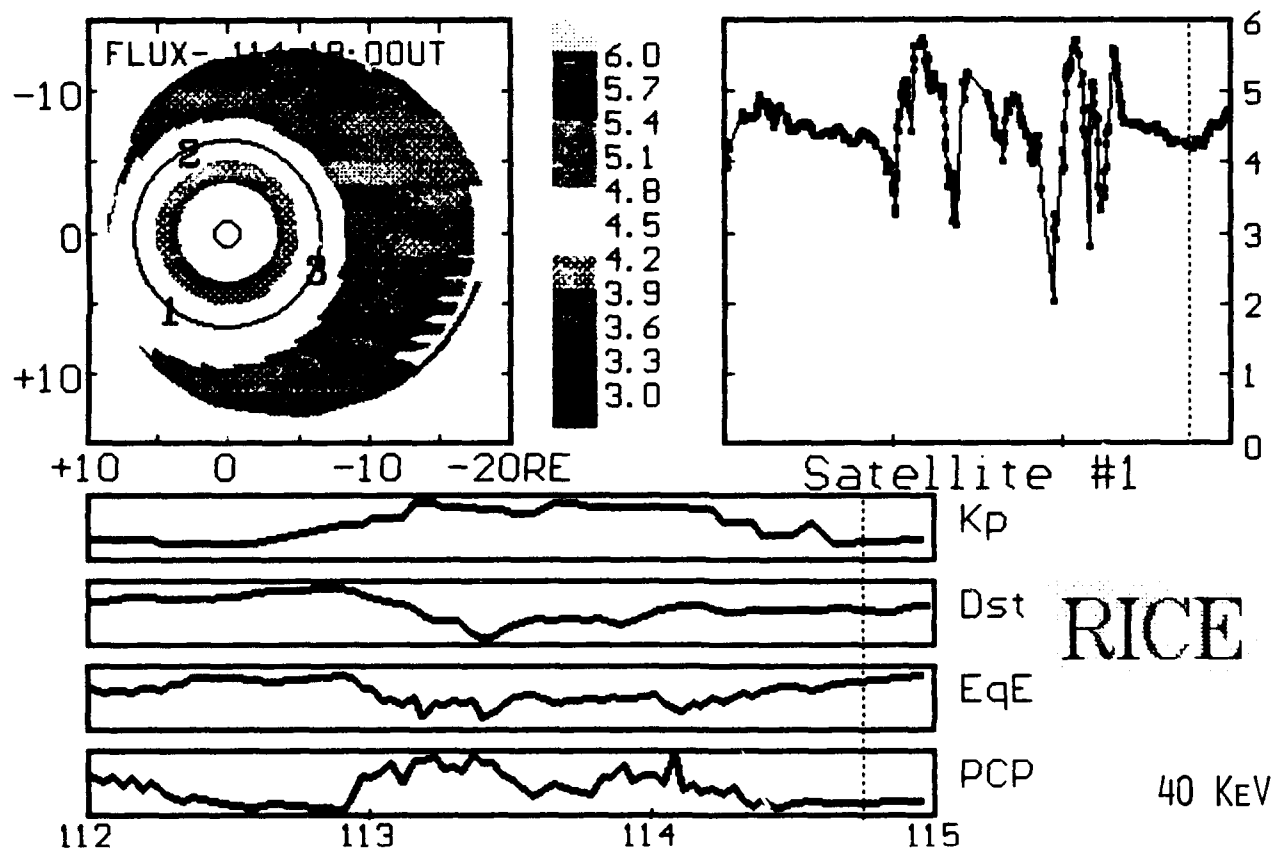


Figure 3.9

4. VALIDATION STATISTICS

In order to obtain statistics to determine the accuracy of the MSM, the model output was compared with electron flux data from three geostationary orbit satellites supplied by the Air Force. No geostationary satellite flux data were used as inputs to the model. The three satellites were well spaced in local time and therefore represent a good test of the model accuracy at all local times. The event used was the large magnetic storm of April 21-23, 1988 discussed in section 3.2. The following sections describe the results of this study.

4.1. Model Inputs

The input data to the MSM used for the test event are Kp, Dst, solar wind velocity, solar wind density, the polar cap potential drop, the polar cap potential pattern type and the equatorward edge of the auroral zone (see Table 4.1). The solar wind velocity and density were used to calculate the standoff distance, which is the distance from the center of the earth to the magnetopause at the subsolar-point. The standoff distance, Dst and the equatorward edge of the auroral zone are used by the B-field model in the MSM. The E-field model uses the polar cap potential, the polar cap potential pattern, the equatorward edge of diffuse aurora and its time derivative. Initial- and boundary-condition fluxes are based on Kp.

Table 4.1.

The MSM Input Parameters		
Input	Base	Figure
Kp	Ground observation	Figure 4.1
Dst	Ground observation	Figure 4.2
Solar wind velocity	Satellite observation NSSDC	Figure 4.3
Solar wind density	Satellite observation NSSDC	Figure 4.4
Polar cap potential drop	Satellite observation DMSP data GL/UTD	Figure 4.5
Polar cap potential pattern	Satellite observation DMSP data GL/UTD	Figure 4.6
Equatorward edge of the auroral zone	Satellite observation DMSP data GL	Figure 4.7

NSSDC: The National Space Science Data Center

GL: Geophysical Laboratory

UTD: University of Texas at Dallas

4.2. Model Outputs

4.2.1 The Interpolation

In order to compare the MSM output with the satellite observation, the MSM predicted fluxes had to be determined at the three Air-Force satellite local times and locations. Since the output time intervals of the MSM and the satellite data times are generally different, and since the MSM grid points are not necessarily at the geosynchronous orbit local times of the satellites, the model output fluxes had to be interpolated in time and space. This interpolation was accomplished as follows:

- (1) First, the spatial interpolation was performed both for t_1 and t_2 where

$$t_1 < t_{\text{satellite}} < t_2$$

and t_1, t_2 are the times of the closest MSM output. This spatial interpolation was linearly calculated in terms of the fluxes at the model grid points as shown in figure 4.8.

- (2) Then the two model fluxes $J(t_1)$ and $J(t_2)$ were linearly interpolated in time:

$$J(\text{at the satellite}) = J(t_1) * (t_2 - t_{\text{satellite}}) / (t_2 - t_1) + J(t_2) * (t_{\text{satellite}} - t_1) / (t_2 - t_1).$$

In summary, this is a 3-dimensional (2D-spatial and 1D-temporal) linear interpolation. In this evaluation, the magnetic and the geographic equatorial planes are assumed to be the same. And the quantity (flux volume)^{-2/3} at the geosynchronous orbit is taken to be approximately 7.0.

4.2.2 Results

The electron fluxes at geosynchronous orbit were computed for two differential energy channels, 30-44keV and 44-64keV, using the data supplied by the Air Force. The differential channel passbands of the detectors are much larger than these widths and so the fluxes in adjacent channels were subtracted to form the smaller differential channels. In consultation with Tom Cayton of LANL, a standard correction was added for detector dead-time. At the same time, the lowest channel flux was increased by a factor of 2 and the next lowest by 1.4 to achieve agreement with ATS data [Garrett, Private Communication]. These corrections are discussed in detail in Quarterly Report no.11.

The MSM output fluxes and the corresponding satellite fluxes are plotted in figures 4.9 to 4.14. In these figures, the thick solid lines denotes the MSM output, the solid lines with square markings are the satellite measurements. Also shown as the solid thin lines are the output from a model of the average geostationary electron fluxes prepared by Garrett.

4.3. The Garrett model

Through the courtesy of H.B. Garrett, Geophysics Laboratory (currently at the Jet Propulsion Laboratory), we obtained a statistical model that computes average electron fluxes at arbitrary local time for Kp values up to 6 at the geostationary orbit. This model is described in detail in section 2.2.2.4. The Garrett model was run for the April 21-23, 1988 event. The model generates geostationary electron fluxes with the input of the satellite local time and Kp.

4.4. Evaluation of Accuracy

For the evaluation of the accuracy of a model, it would seem to be desirable to have a single parameter, or accuracy index, which can be taken as an indicator of the extent to which the model follows the observations. In fact, as we shall see, such an approach is risky when the goal is to build a model which accurately predicts occurrences of worst-case or adverse storm conditions. Nonetheless, we have chosen for such an index the root-mean-square of the log of the ratio of the model to the satellite fluxes averaged over the most active two days of the test event. It is essential to use the logarithm because of the large dynamic range of the fluxes, nearly four orders of magnitude.

$$\sqrt{\left\langle \left(\log_{10} \frac{J_{\text{model}}}{J_{\text{satellite}}} \right)^2 \right\rangle}$$

This parameter was calculated for each of the two differential energy bands mentioned above and for all three satellites. The results are shown in Tables 4.2 and 4.3.

Table 4.2. The rms of errors (40keV)

model	Satellite-1	Satellite-2	Satellite-3
MSM	0.7350	0.5949	0.7434
Garrett	1.2062	1.1683	1.2817

Table 4.3. The rms of errors (65keV)

model	Satellite-1	Satellite-2	Satellite-3
MSM	0.9238	0.5231	0.7630
Garrett	0.6380	0.5328	0.4758

It is seen that the best agreement is with satellite -2 at the higher energy. For this case the difference would be a factor of 3.3. The worst case is found for satellite -1 for the same energy range, a factor of 8.4.

4.5 Conclusions

Based on the time-dependent data presented in this section and section 3.2, throughout the run, the Magnetospheric Specification Model was able to predict storm related electron enhancements in good time agreement with geosynchronous satellite data.

Based on the accuracy index reported in section 4.4, the MSM prediction was very much better than the statistical Garrett model for 40keV electron fluxes. This is partly because the Garrett average fluxes were too high for this energy range. However, for the higher energy channel, the index showed that the MSM predictions were worse than the Garrett model. At the same time, the MSM fluxes followed enhancements in the fluxes far better than the Garrett model. The Garrett model fails completely in predicting the high fluxes. This illustrates the inappropriateness of a single parameter index for the purpose of assessing model accuracy.

The MSM never failed to predict high electron fluxes when they were observed. There were, however, some instances when the satellites reported sudden decreases, or flux dropouts, not predicted by the MSM. We tentatively attribute these instances to two possible situations. In some cases, the plasma sheet may have been very thin, as reported to be possible by Sergeev et al., [1990], so that the spacecraft may have been beyond and above or below the plasma sheet and hence on open field lines or on field lines that extend very far out into the plasma sheet and therefore contain lower plasma fluxes. Our magnetic-field model is not stretched enough to represent these very thin plasma sheet configurations. In other cases, the electric-field model may have resulted in the particles being injected too deeply into the magnetosphere. The sunward-flow region of the electric-field model tends to be more confined in latitude than is consistent with observations, which would account for this extra-deep injection. There has not been sufficient time in the contract to correct these late-surfacing and rather minor deficiencies, however, a B-field model with a thinner current sheet is being tested.

Near 0200 UT of day 114, satellite-2 observed an average quiet-time electron flux level, but the MSM predicted a flux dropout. At the same time that the dropout was predicted by the MSM, a strong enhancement of the polar cap potential was observed by the DMSP satellite (see figure 4.5). The MSM dropout represented the transport of low-density flux tubes, which had previously been on trapped orbits at the geostationary orbit, to untrapped orbits which intersect the magnetopause. The fact that Spacecraft-2 did not experience any dropout may indicate that, either the model overestimated the radial transport associated with the increased potential drop, or that the outward transport occurred over a limited range of local time that did not include the spacecraft.

In summary, the model never failed to predict high fluxes when they were observed. However, it sometimes predicted high fluxes when they were not observed, and it failed to predict flux dropouts. On one occasion it predicted a dropout during a low flux level. The model fluxes for prestorm conditions were higher than reported by the satellites.

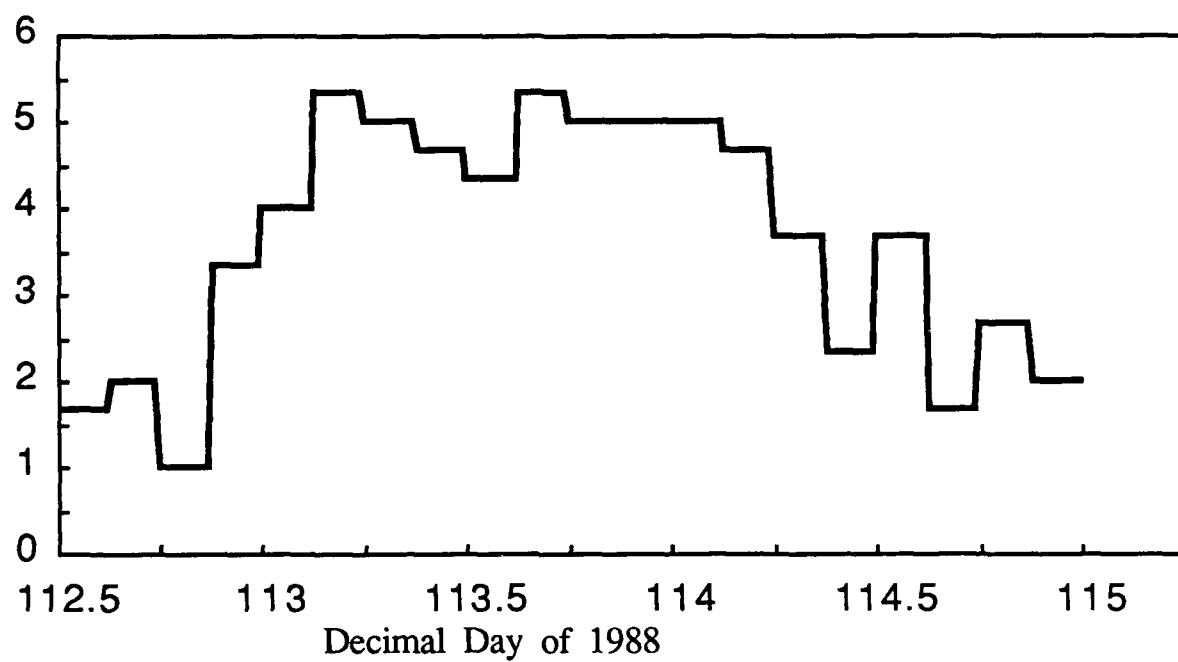


Figure 4.1 The MSM input: K_p

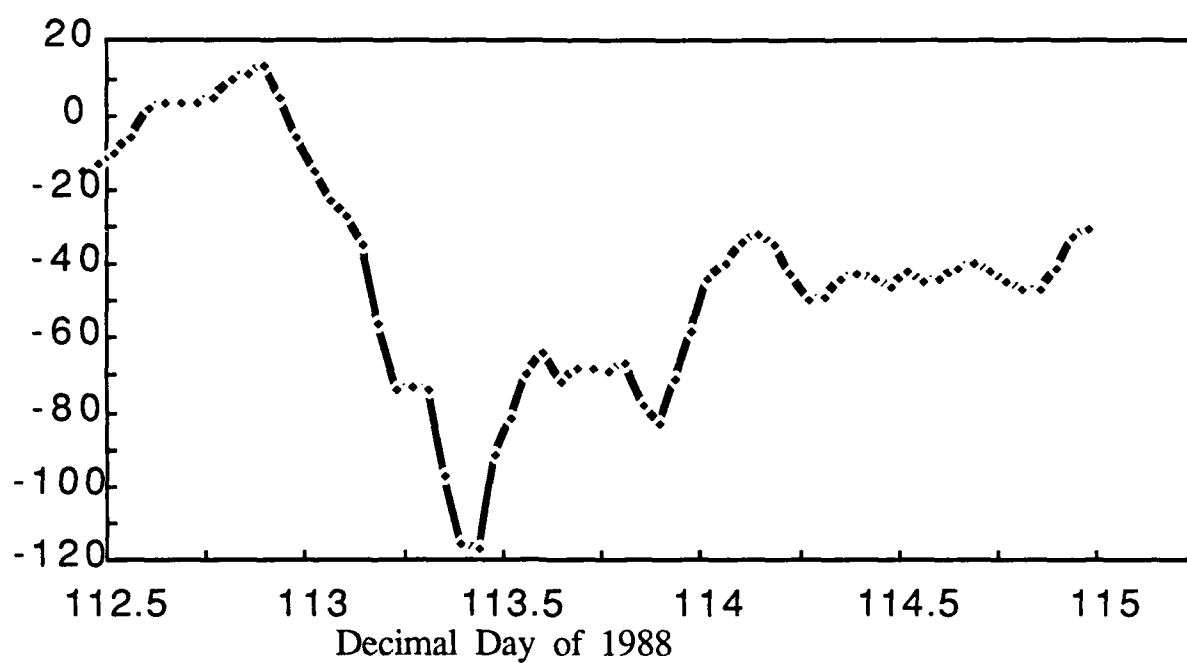


Figure 4.2 The MSM input: Dst [nT]

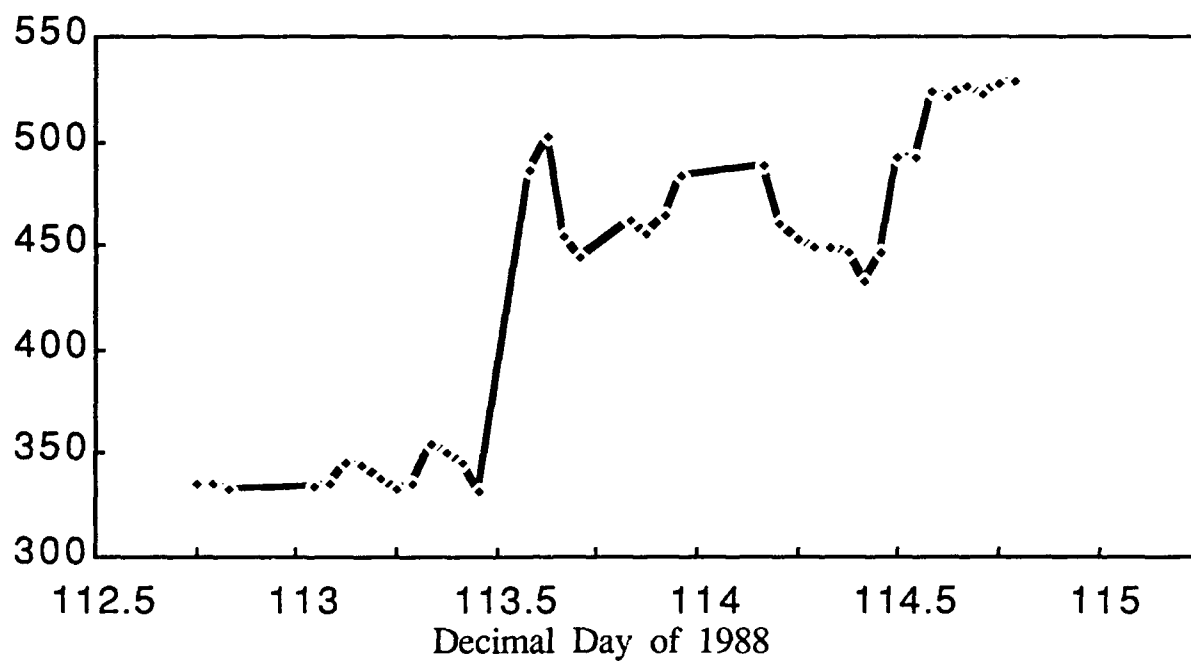


Figure 4.3 The MSM input: Solar wind velocity [km/s]

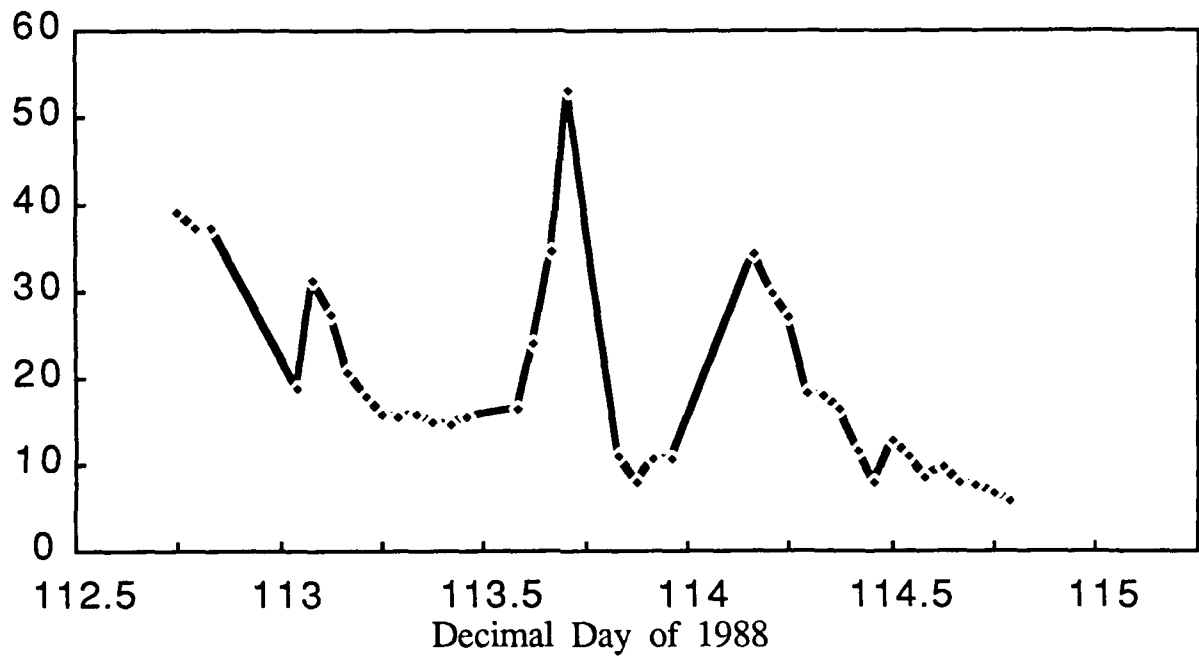


Figure 4.4 The MSM input: Solar Wind density [\#/cm^3]

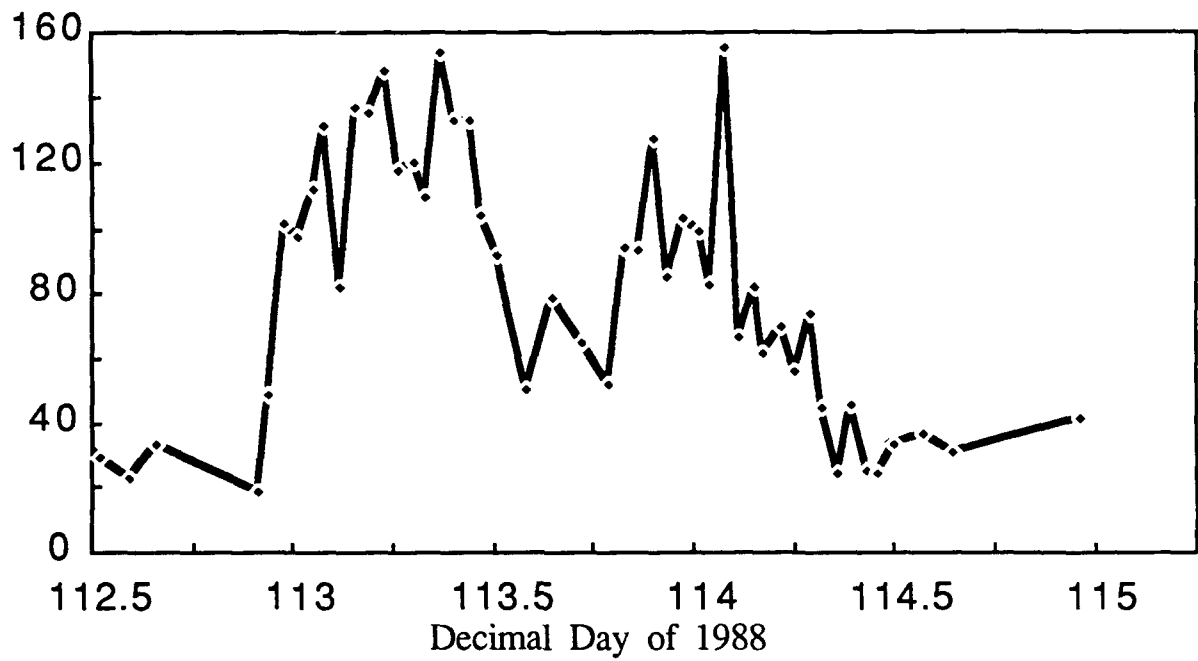


Figure 4.5 The MSM input: Polar cap potential

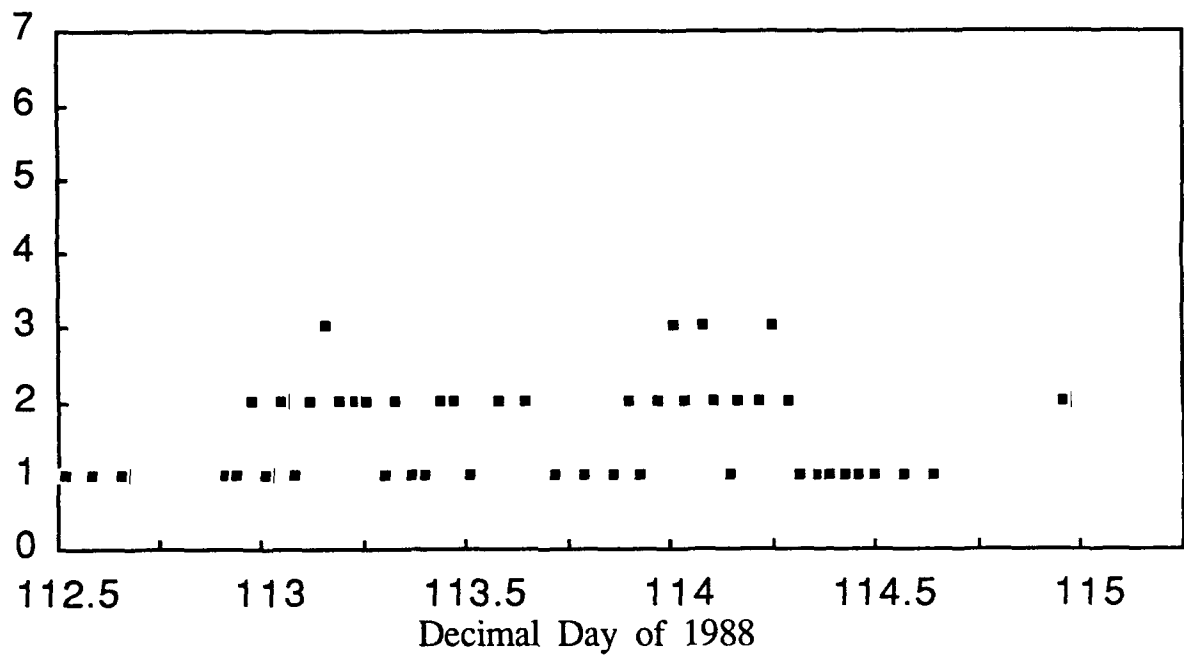


Figure 4.6 The MSM input: Polar cap potential pattern

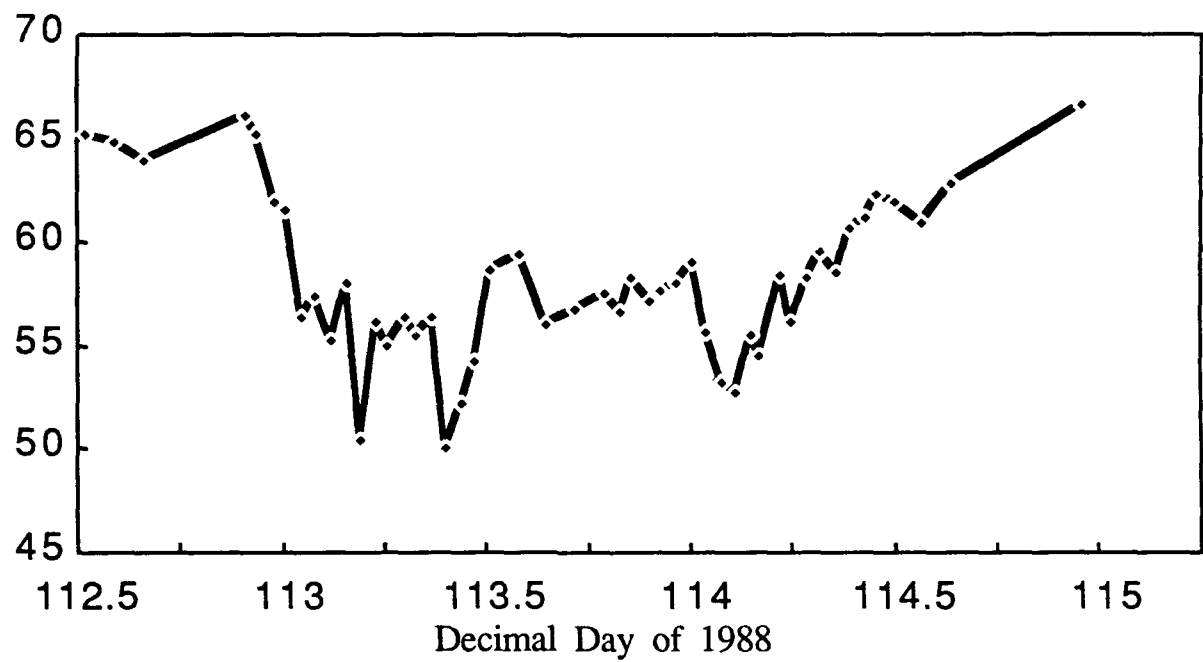
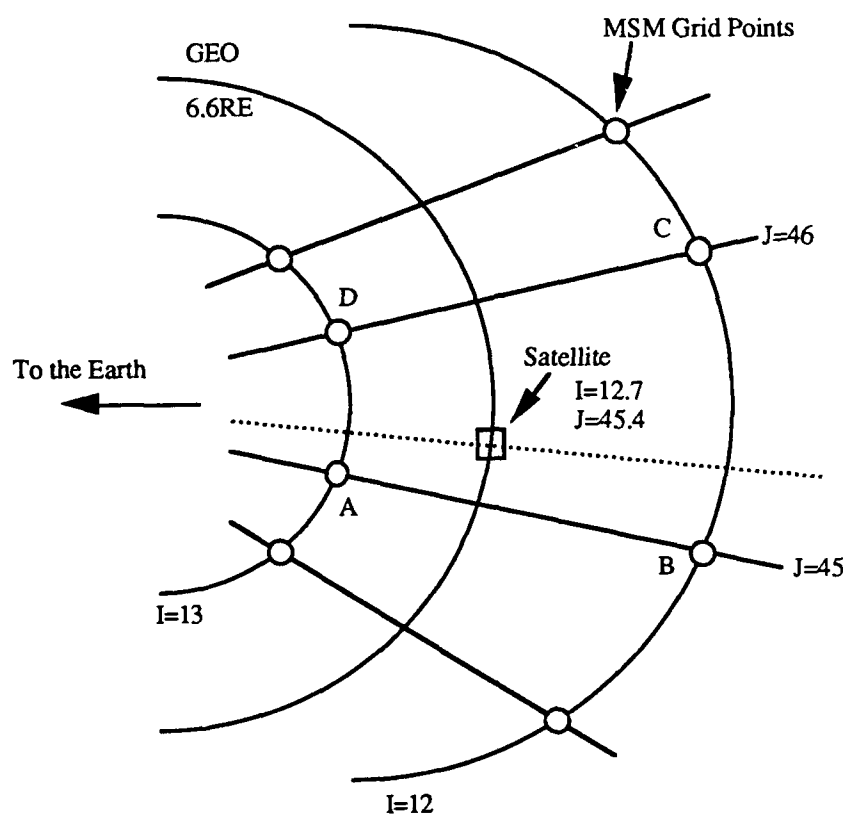


Figure 4.7 The MSM input: Equatorward edge of the auroral zone
[degree latitude]



$$J_{\text{satellite}} = 0.6 (0.7A + 0.3B) + 0.4 (0.7D + 0.3C)$$

Figure 4.8 An example of the spatial interpolation.

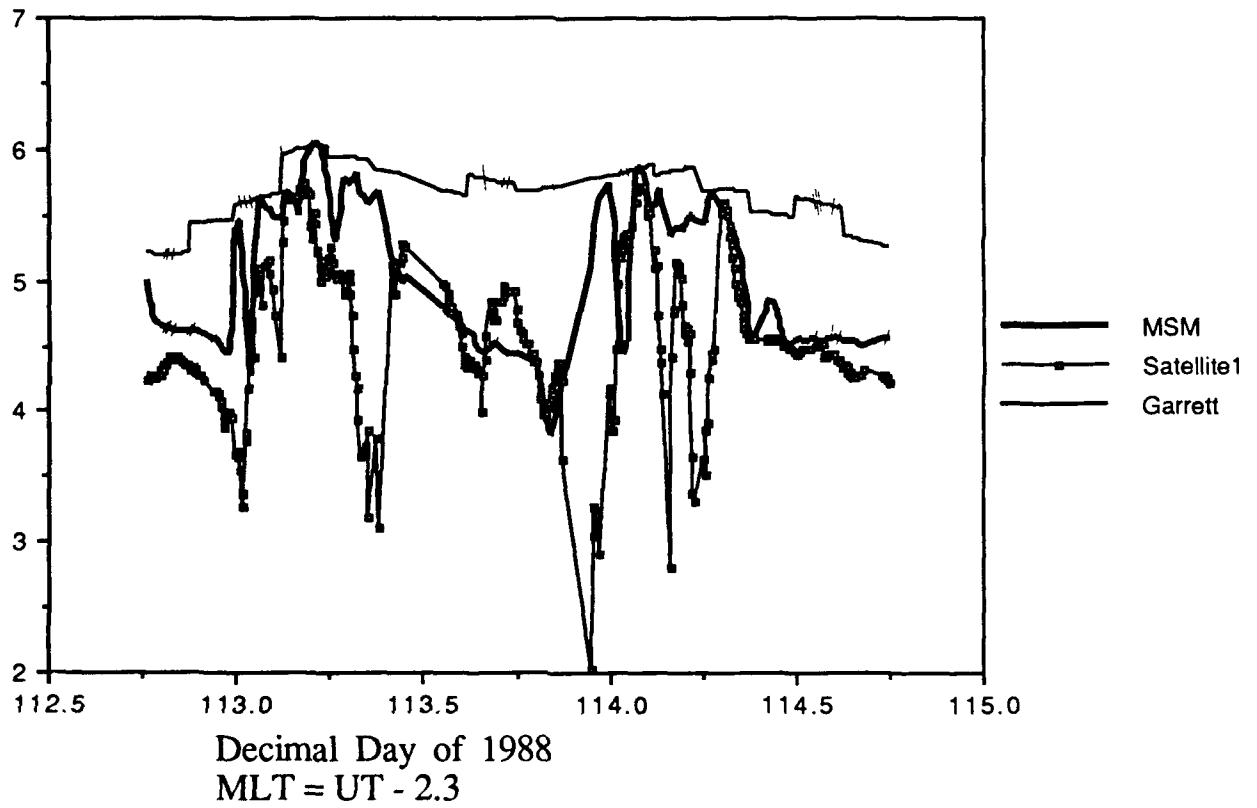


Figure 4.9 The 40keV electron differential fluxes of the MSM, Garrett model and the observations by the satellite-1.
[$\log_{10}(\text{electrons}/\text{cm}^2/\text{s}/\text{sr}/\text{keV})$]

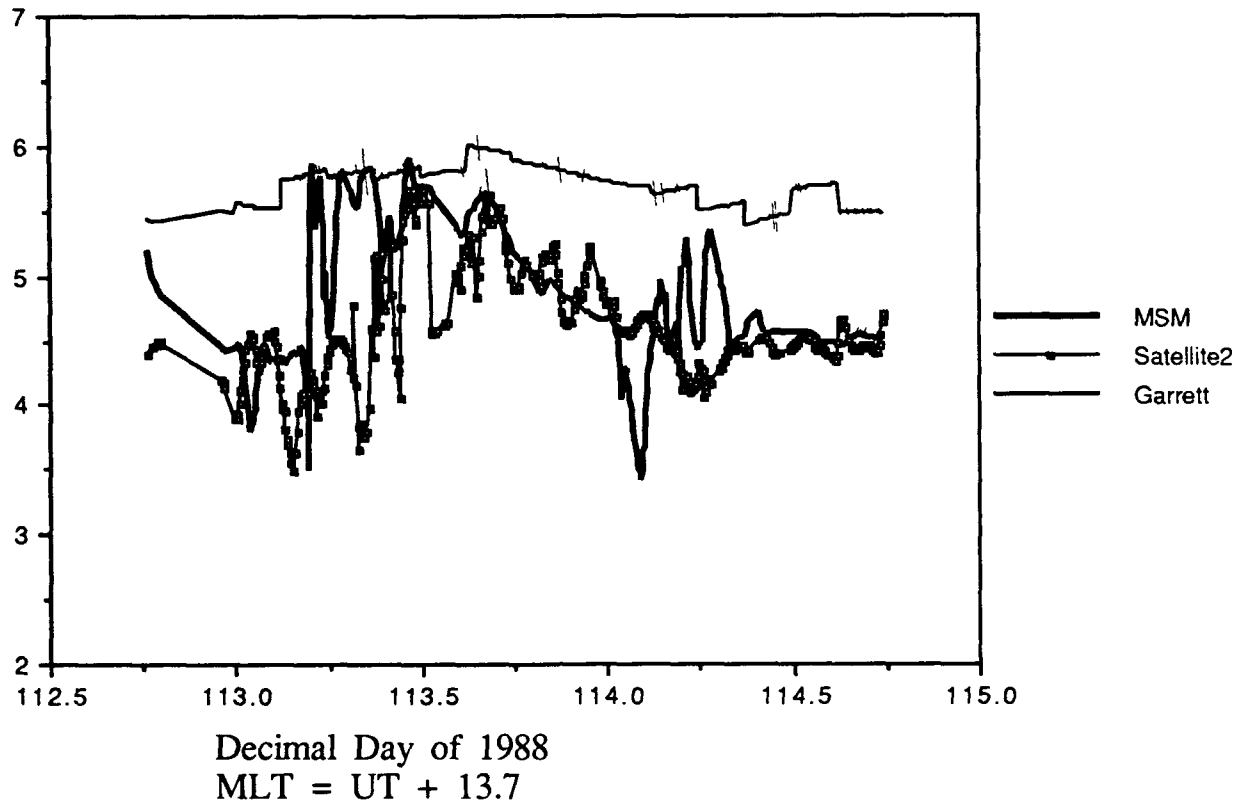
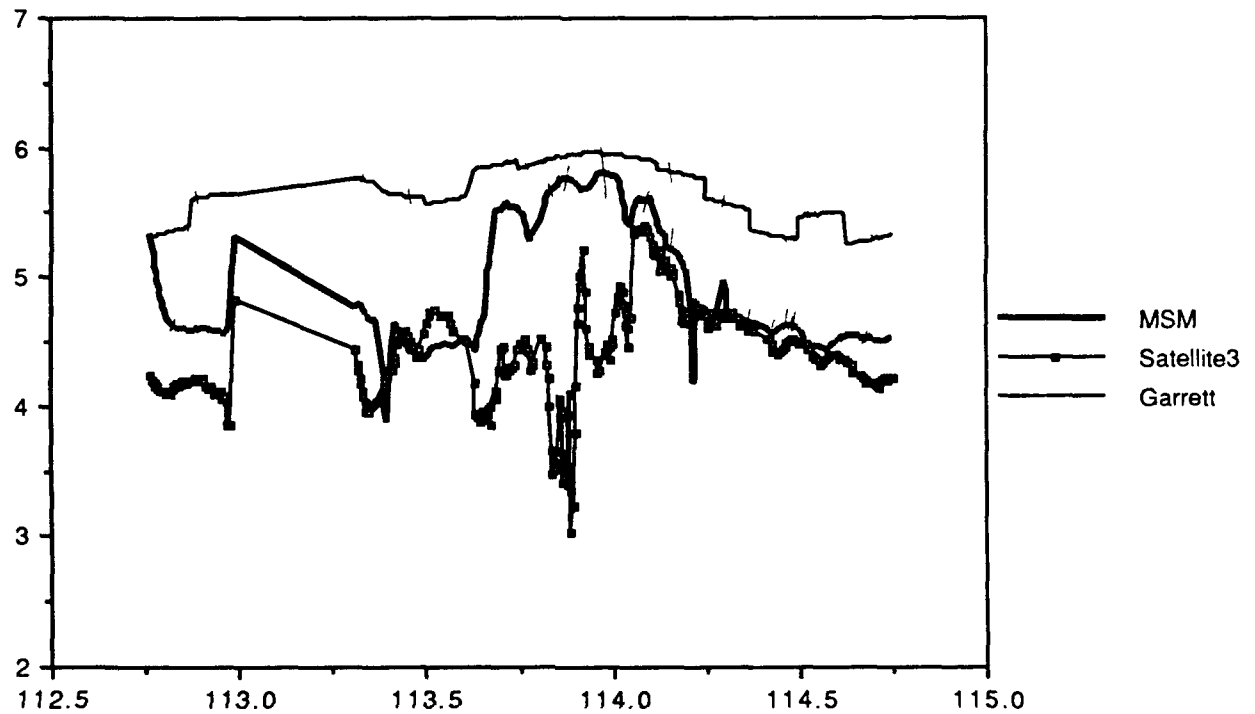


Figure 4.10 The 40keV electron differential fluxes of the MSM, Garrett model and the observations by the satellite-2.
 [$\log_{10}(\text{electrons /cm}^2 \text{ /s /sr /keV})$]



Decimal Day of 1988
MLT = UT + 4.7

Figure 4.11 The 40keV electron differential fluxes of the MSM, Garrett model and the observations by the satellite-3.
[$\log_{10}(\text{electrons /cm}^2 \text{ /s /sr /keV})$]

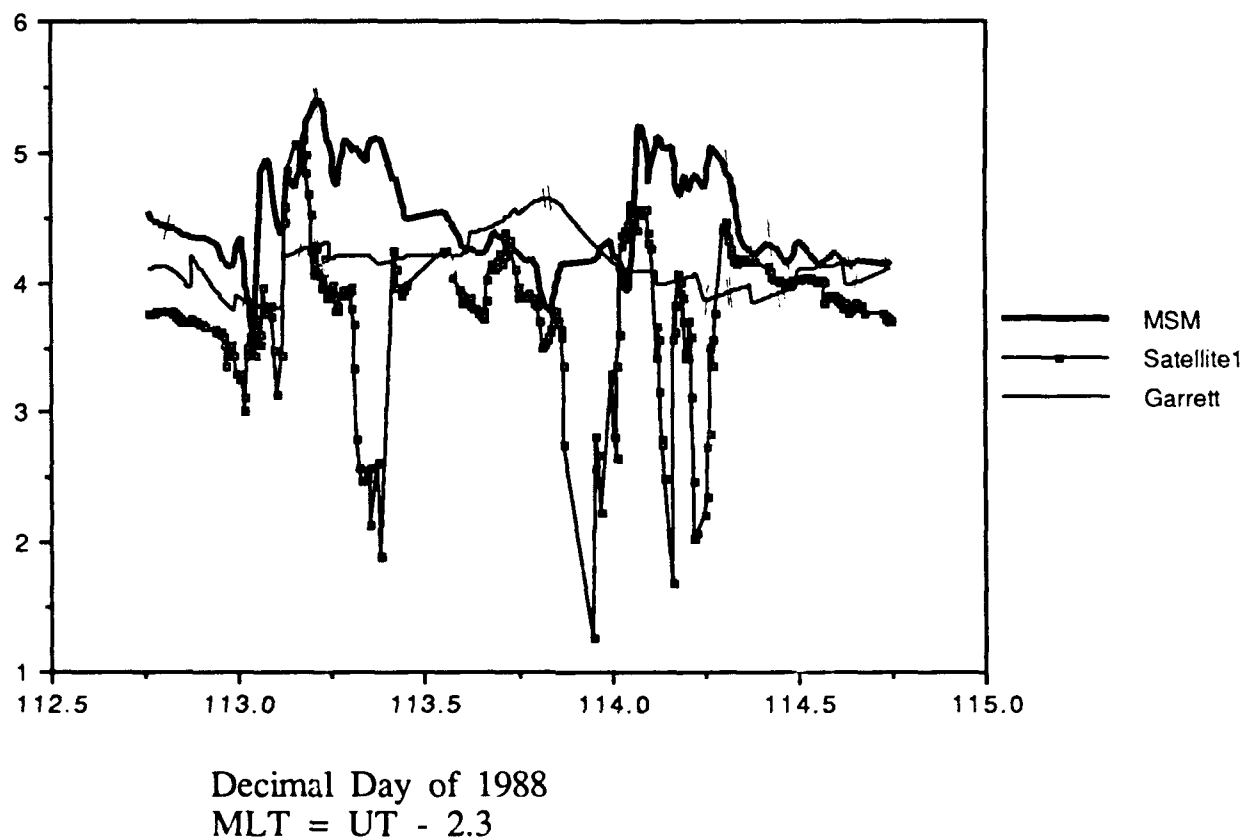


Figure 4.12 The 65keV electron differential fluxes of the MSM, Garrett model and the observations by the satellite-1.
 $[\log_{10}(\text{electrons}/\text{cm}^2/\text{s}/\text{sr}/\text{keV})]$

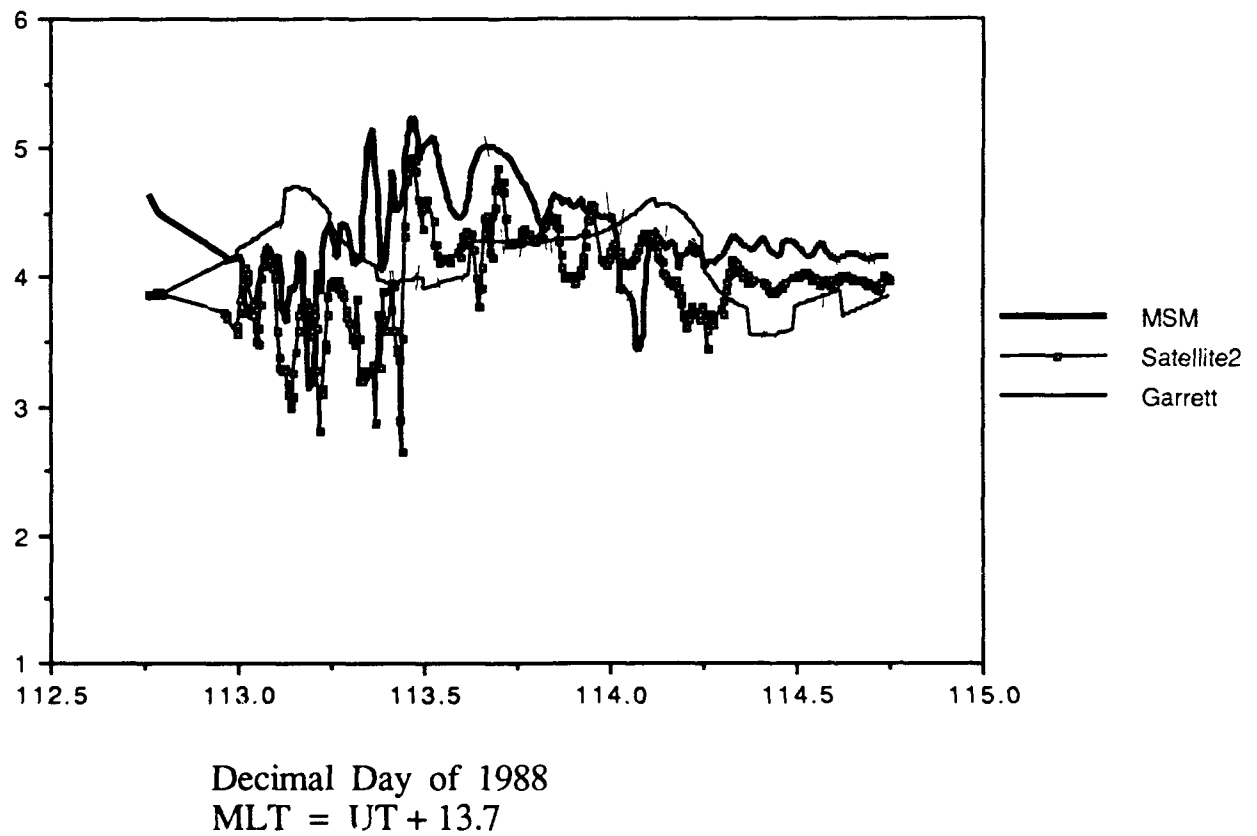


Figure 4.13 The 65keV electron differential fluxes of the MSM, Garrett model and the observation by the satellite-2.
 $[\log_{10}(\text{electrons}/\text{cm}^2/\text{s}/\text{sr}/\text{keV})]$

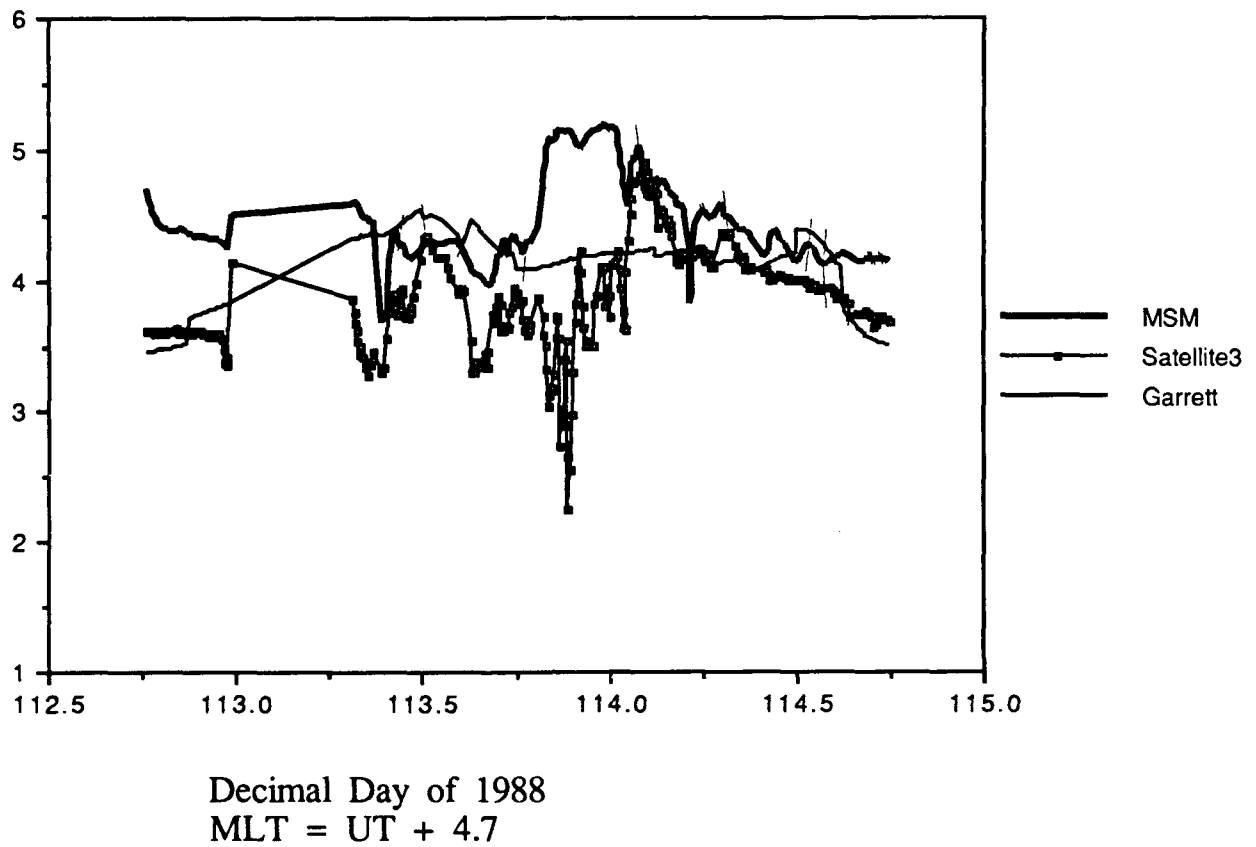


Figure 4.14 The 65keV electron differential fluxes of the MSM, Garrett model and the observations by the satellite-3.
[$\log_{10}(\text{electrons/cm}^2/\text{s}/\text{sr}/\text{keV})$]

5. MSM Source Code Description and Documentation

5.0 Language and Documentation

The MSM code was developed primarily on an IBM 3081d and is in ANSI standard Fortran-77. Before delivery to the Air Force, it was converted for operation on a Microvax II to be DEC compatible. The B-field matrices were computed on an Apollo 10000.

All code was written with AFWL-TR-85-26, Fortran-77 Computer Program Structure and Internal Documentation Standards for Scientific Applications, as a guide. The code itself is internally documented and has been carefully maintained throughout development.

As requested by the Air Force, drafts of specific sections of the documentation consistent with DoD-STD-7935A can be found in the Appendix of this report. This documentation was placed in the Appendix because the paragraph numbering system described by DoD-STD-7935A is not consistent with that used for the body of this report. A hard-copy program listing and tape copy are included with this report.

6. The Field Line Tracing Program, *MAPINT*

6.0. Background

The MSM generates values for the electron and ion fluxes at each grid point on a latitude - magnetic local time grid in the ionosphere and the point at which the field line from each grid point passes through the equatorial magnetic reference surface. New flux values are produced every 15 minutes of magnetosphere time. *MAPINT* is the program developed by Rice, at the request of the Air Force, to meet the practical requirement for obtaining the particle flux at any arbitrary satellite position, at any arbitrary time. *MAPINT* interpolates and extrapolates the MSM output to relevant times and locations. This is accomplished by tracing magnetic field lines and using the interpolated flux from the equatorial plane as the new flux value.

MAPINT is interactive, providing operator prompts and responding with the results on screen displays. *MAPINT* can also form the basis for more routine or sophisticated displays of MSM output such as those discussed in Quarterly Report No. 11 and presented by Rice at the February Review meeting.

MAPINT, as delivered, is a core program that uses machine specific file access for its input data files. The delivered version is self-contained i.e. has its own data files, and will need to be revised for use with the MSM on any new machine.

6.1 How *MAPINT* Works

Since the MSM magnetic field model is not computed "on-the-fly" but rather uses a table-lookup of precomputed matrices, the tracing of the magnetic field line passing through an arbitrary satellite position to the equator cannot be done directly. Instead, the values of the B-field input parameters (standoff, Dst, and lower latitude boundary of the aurora) nearest in time to the desired flux time, for which B-field matrices exist, are used to generate eight field line traces back to the equator. (The delivered version of *MAPINT* is capable of including both dipole tilt and collapse configurations, in which case thirty-two field line traces are performed.) Figures 6.1 and 6.2 illustrate the eight nearest neighbors in parameter space and the tracing of the resulting eight lines.

Next, the satellite's actual field line crossing point is determined by interpolating the eight model crossing points using weighting factors from the actual parameter space location. Finally, the flux at the satellite point is taken to be the same as the flux at the point determined above as interpolated from the fluxes at the adjacent four grid points.

6.2 *MAPINT* Operating Instructions

The following is a list of program input, output, program checks and required files for *MAPINT*:

Program input:

1. Time (year, julian day, hour, minute, second)-integer format.
2. Energy (KeV)-real format.
3. Particle type (electron, H⁺, O⁺)-integer format.(integer code included in prompt)
4. Point in space from which to start mapping e.g a satellite position (GSM coordinates, R_e)-real format.

Program output:

1. Spatial spread of equatorial reference surface points used for interpolating magnetic field equatorial crossing point (GSM coordinates, R_e).
2. Point on the magnetic equatorial plane that the satellite point maps to (GSM coordinates, R_e).
3. Flux at the input data point ($\log_{10}(\#/\text{cm}^2\text{-s-KeV-ster})$).
4. Error at geostationary orbit, if available.
5. Flag telling whether full-traceback or KP-based fluxes were used.

Program checks:

1. Input time is reasonable (ie, hours<24, minute<60).
2. Energy >0.
3. Input spatial point is valid (ie, >1 R_e).
4. Input spatial point is not on an open field line.
5. Input spatial point is within the model calculation boundary.
6. Particle type is correct.
7. Energy and particle type were calculated in the MSM run.

Files needed to run program and unit numbers:

1. FLUX, unit=15.
2. UPDAT, unit=44.
3. VM, unit=16.
4. BNDLOC, unit=17.
5. XMIN, unit=18.
6. YMIN, unit=19.
7. ZMIN, unit=20.
8. The magnetic field matrices associated with the run.

The program is fully interactive. It requests the input information and displays the results on the terminal. The following pages are copies of an actual session:

DMSL107401 Execution begins...

ENTER LAST 2 DIGITS OF YEAR AND JULIAN DAY

?

88 112

ENTER HOUR, MINUTE, AND SECONDS

?

18 40 30

INPUT ENERGY (KEV) AND 1 FOR ELECTRONS, 2 FOR H+,
OR 3 FOR O+

?

44.5 1

ENTER SPATIAL POINT OF INTEREST IN GSM (RE): X,Y,Z

?

0 -6.5 1.15

MAPPING POINTS USED FOR INTERPOLATION WERE SPREAD:

0.273004286E-01 RE ALONG THE XGSM DIRECTION

0.657844543E-01 RE ALONG THE YGSM DIRECTION

0.261033997E-01 RE ALONG THE ZGSM DIRECTION

INTERPOLATED MAPPING POINT: XGSM YGSM ZGSM

-0.229525417E-01 -6.85174847 -0.299130827E-01

LOG FLUX AT THE SATELLITE = 4.12708187

HOLDING RICECSUM

TRACE FROM ANOTHER STARTING POINT

WITH SAME TIME PARAMETERS? (1 = YES)

?

1

INPUT ENERGY (KEV) AND 1 FOR ELECTRONS, 2 FOR H+,
OR 3 FOR O+

?

150 1

ENTER SPATIAL POINT OF INTEREST IN GSM (RE): X,Y,Z

?

5.16 3.96 1.15

MAPPING POINTS USED FOR INTERPOLATION WERE SPREAD:

0.775260925E-01 RE ALONG THE XGSM DIRECTION

0.452785492E-01 RE ALONG THE YGSM DIRECTION

0.123842776 RE ALONG THE ZGSM DIRECTION

HOLDING RICECSUM

INTERPOLATED MAPPING POINT: XGSM YGSM ZGSM
5.34179783 4.13770580 0.488985181E-01

LOG FLUX AT THE SATELLITE = 2.26998138

TRACE FROM ANOTHER STARTING POINT
WITH SAME TIME PARAMETERS? (1 = YES)

?
0
AGAIN WITH NEW TIME? (1 = YES)

?
1
ENTER LAST 2 DIGITS OF YEAR AND JULIAN DAY

?
88 112
ENTER HOUR, MINUTE, AND SECONDS

?
45 30 23
INCORRECT INPUT FOR HOUR-MUST BE BETWEEN 1 AND 23

HOLDING RICECSUM

INCORRECT INPUT. DO YOU WANT TO TRY AGAIN?
ENTER 0 TO STOP, ANY OTHER NUMBER TO TRY AGAIN.

?
1
ENTER LAST 2 DIGITS OF YEAR AND JULIAN DAY

?
88 112
ENTER HOUR, MINUTE, AND SECONDS

?
18 23 45
INPUT ENERGY (KEV) AND 1 FOR ELECTRONS, 2 FOR H+,
OR 3 FOR O+

?
63 4
INCORRECT INPUT FOR PARTICLE TYPE. PLEASE RE-ENTER.

INPUT ENERGY (KEV) AND 1 FOR ELECTRONS, 2 FOR H+,
OR 3 FOR O+

HOLDING RICECSUM

?

63 1

ENTER SPATIAL POINT OF INTEREST IN GSM (RE): X,Y,Z

?

-3.96 5.16 1.15

MAPPING POINTS USED FOR INTERPOLATION WERE SPREAD:

0.131410599 RE ALONG THE XGSM DIRECTION

0.752048492E-01 RE ALONG THE YGSM DIRECTION

0.450904071E-01 RE ALONG THE ZGSM DIRECTION

INTERPOLATED MAPPING POINT: XGSM YGSM ZGSM

-4.23088074 5.47604370 -0.904994830E-02

LOG FLUX AT THE SATELLITE = 3.66756821

TRACE FROM ANOTHER STARTING POINT

WITH SAME TIME PARAMETERS? (1 = YES)

?

UM READ RICECSUM

0

AGAIN WITH NEW TIME? (1 = YES)

?

0

Ready; T=67.04/68.61 19:58:23

6.3 *MAPINT* Validation Using the April 21-23, 1988 Event

As a validation and demonstration exercise, *MAPINT* was applied to a hypothetical spacecraft located at 3 Re and 45 degrees inclination (GSM coordinates: $X=-2.12$, $Y=0$, $Z=2.12$) for three times during the April 21-23, 1988 event. The times selected were intended to be illustrative of expected behavior of the magnetic field during certain phases of the storm. The times were 18:30 on day 112, and 00:00 and 06:00 on day 113. Figure 6.3 shows the results.

In figure 6.3, we have a cartoon of the field line shapes and positions for each of the three times, for field lines originating at the spacecraft. The field lines are not drawn to scale. The Log of the electron fluxes and the equatorial crossing points of the satellites, as computed by *MAPINT*, are shown. We also show the position, in the storm, of each time as seen in the geophysical parameter diagram at the bottom of the figure.

The first time, 18:30 on day 112, is prestorm - early growth phase. The figure shows that the field is reasonably dipolar, in other words not stretched tailward too much by tail currents. The second time, the start of day 113, shows a highly stretched field line expected of the expansion phase, before the collapse or injection has reached the L-shell of the spacecraft. The last time, 06:00 on day 113, shows the field line connecting the spacecraft to have collapsed to the more dipole-like configuration, as would be expected for late injection.

The magnetic field morphology and dynamics exhibited here are generally what are expected. Since there are no measurements of the magnetic field available, there can be no true validation beyond this qualitative analysis. Moreover, we have no satellite particle flux data at the hypothetical location. Validation of the B-field model is actually accomplished by validation of the MSM, as discussed in sections 3 and 4. We are satisfied that *MAPINT* is providing a correct extrapolation of the MSM flux values and is using correctly the B-field model available to it.

For acceptance purposes, entry of the given times and satellite location in *MAPINT* should reproduce the fluxes and field line equatorial crossing points shown in figure 6.3.

Detailed documentation on *MAPINT* can be found in the Appendix.

6.3 *MAPINT* Validation Using the April 21-23, 1988 Event

As a validation and demonstration exercise, *MAPINT* was applied to a hypothetical spacecraft located at 3 Re and 45 degrees inclination (GSM coordinates: $X=-2.12$, $Y=0$, $Z=2.12$) for three times during the April 21-23, 1988 event. The times selected were intended to be illustrative of expected behavior of the magnetic field during certain phases of the storm. The times were 18:30 on day 112, and 00:00 and 06:00 on day 113. Figure 6.3 shows the results.

In figure 6.3, we have a cartoon of the field line shapes and positions for each of the three times, for field lines originating at the spacecraft. The field lines are not drawn to scale. The Log of the electron fluxes and the equatorial crossing points of the satellites, as computed by *MAPINT*, are shown. We also show the position, in the storm, of each time as seen in the geophysical parameter diagram at the bottom of the figure.

The first time, 18:30 on day 112, is prestorm - early growth phase. The figure shows that the field is reasonably dipolar, in other words not stretched tailward too much by tail currents. The second time, the start of day 113, shows a highly stretched field line expected of the expansion phase, before the collapse or injection has reached the L-shell of the spacecraft. The last time, 06:00 on day 113, shows the field line connecting the spacecraft to have collapsed to the more dipole-like configuration, as would be expected for late injection.

The magnetic field morphology and dynamics exhibited here are generally what are expected. Since there are no measurements of the magnetic field available, there can be no true validation beyond this qualitative analysis. Moreover, we have no satellite particle flux data at the hypothetical location. Validation of the B-field model is actually accomplished by validation of the MSM, as discussed in sections 3 and 4. We are satisfied that *MAPINT* is providing a correct extrapolation of the MSM flux values and is using correctly the B-field model available to it.

For acceptance purposes, entry of the given times and satellite location in *MAPINT* should reproduce the fluxes and field line equatorial crossing points shown in figure 6.3.

Detailed documentation on *MAPINT* in accordance with DoD-STD-7935A is given in the Appendix.

B-FIELD INPUT PARAMETER SPACE

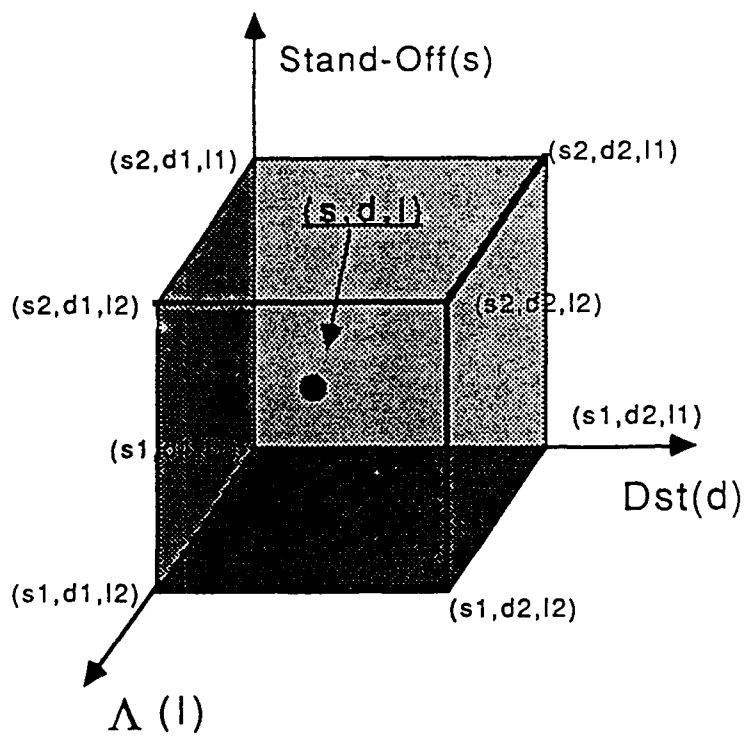


Figure 6.1

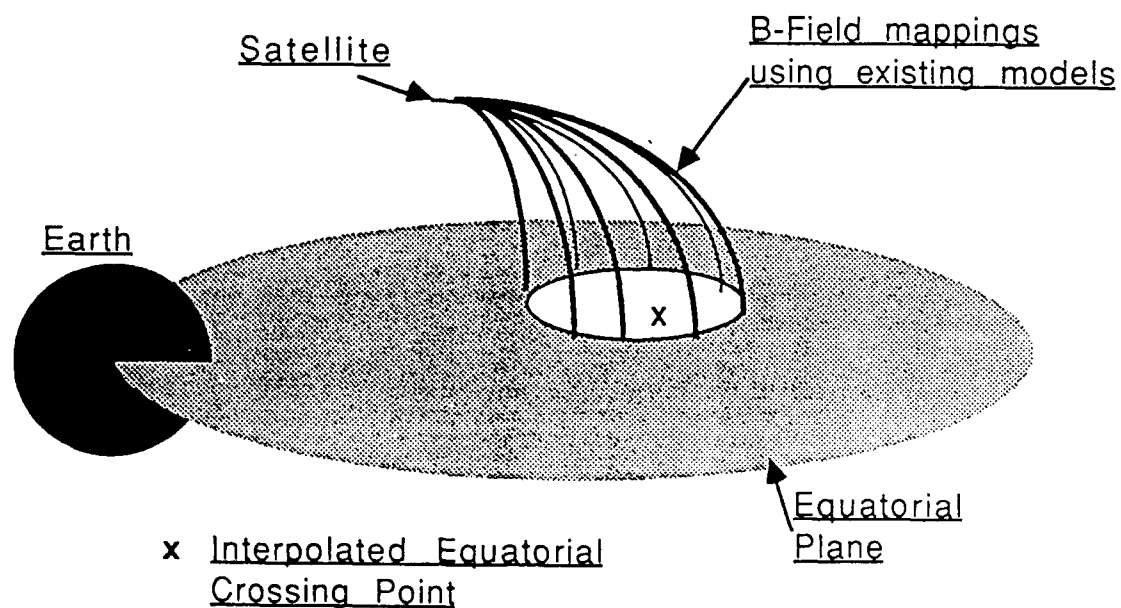


Figure 6.2

Demonstration of MAPINT for a spacecraft at 3
Re and 45 degree inclination for three times
during the April 88 event

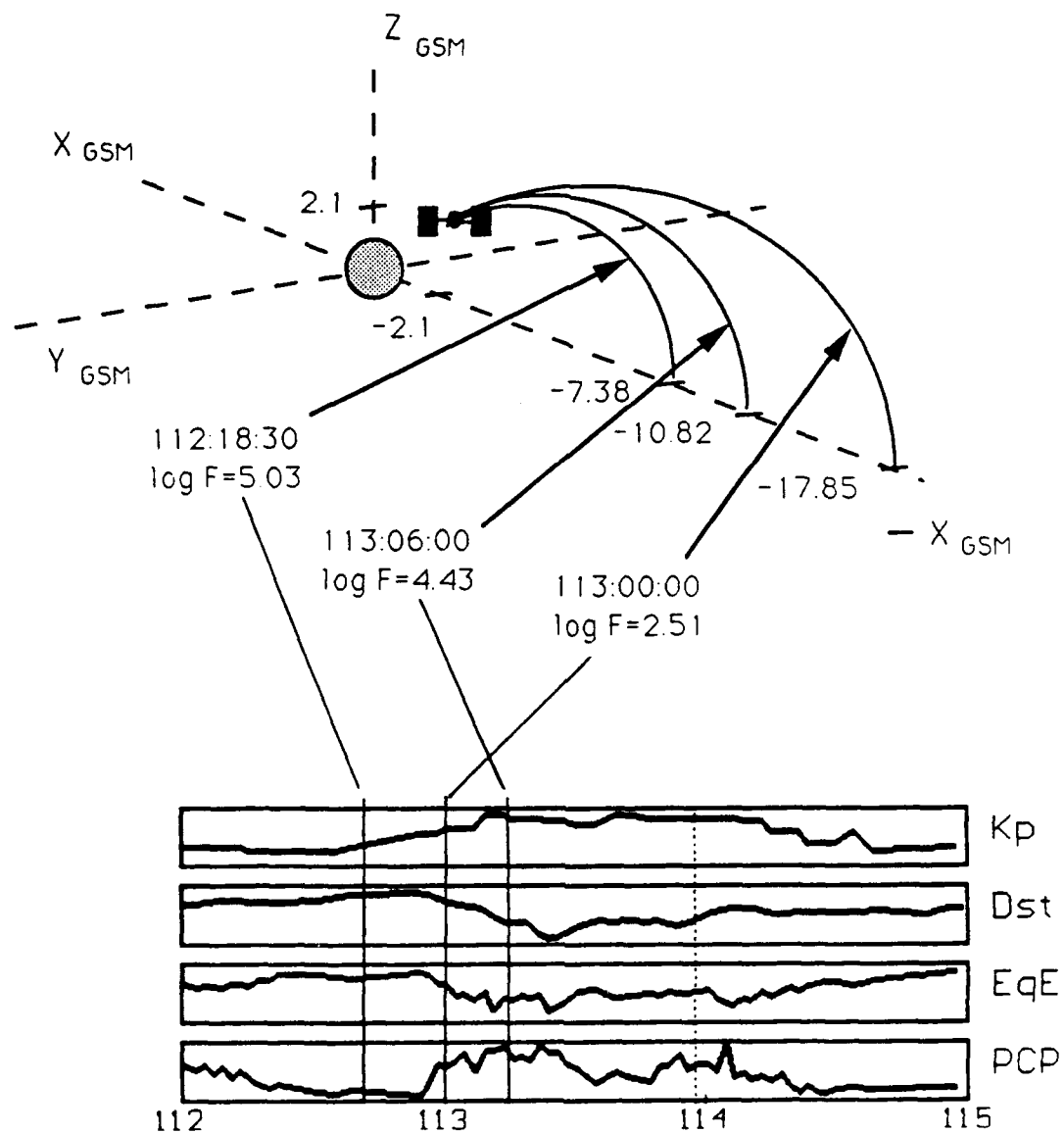


Figure 6.3

7. Summary

Rice has successfully developed a practical computer model capable of specifying electron and ion fluxes in the magnetosphere during geomagnetic storms, based on input data from the Environmental Database.

The Magnetospheric Specification Model represents the first effort at a large-scale computational model of the Earth's magnetosphere that is designed for operational use. The MSM computer algorithm represents a substantial effort to bring the observational knowledge, theoretical understanding, and computer-modeling technology that has been developed in the last thirty years of space research to bear on practical operational problems.

Our testing of the MSM, as presented in Sections 3 and 4 of this Report, indicates that it has achieved significant success in its primary goal of representing fluxes of kilovolt electrons in the geostationary-orbit region. It clearly provides good and useful specifications of these fluxes, and it represents a clear advance in the state of the art.

The application program MAPINT, which is provided with the MSM, provides the capability for mapping fluxes from an arbitrary point in the middle magnetosphere to the equatorial plane, thus providing the capability for flux specification for non-equatorial spacecraft.

A major advantage for the future is that the MSM calculates particle fluxes within the framework of a general magnetospheric model that consistently calculates most other large-scale parameters of the physical system, including the fluxes of precipitating auroral electrons and ionospheric electric fields. This gives the MSM great potential for growth in terms of wider and more valuable specifications.

A major limitation of the present MSM is that many of its capabilities for calculating a wide variety of magnetospheric parameters could not be tested as extensively as we would have liked against real-time observational data. This limitation, which was due to the configuration of available spacecraft and instrumentation, should disappear in large part over the next few years, as new observational data become available to us. The testing of the MSM that is planned for the follow-on contract will provide much better quantitative information on the model's capabilities for specifying parameters beyond the basic 35-100 keV geosynchronous electrons. Additional particle detectors that are now being installed on DoD geostationary spacecraft will provide checks on predictions of low-energy particles. The CRRES-SPACERAD spacecraft will provide a rich and invaluable source of data for $L < 6.6$. Data that are now being synthesized from the great magnetic storm of March 1989 will allow us to verify and quantify the MSM's accuracy for the most extreme geomagnetic conditions. The flexible, modular structure of the MSM will allow us to carry out simple "fixes" by changing very few lines of code, if the extended testing indicates the need for such changes.

In summary, the objectives of the Magnetospheric Specification Model have been met, and a model algorithm is ready for adaptation for use in an operational setting, where the goal is real-time and retrospective specification of hazardous charged-particle fluxes.

Acknowledgements

In addition to those named on the cover page, a large number of persons have contributed to the development of the MSM.

At the Geophysics Laboratory, Nelson Maynard, Lt Col. John Gaudet, Mike Heinemann, Fred Rich, David Hardy, Bill Denig, and Sue Gussenhoven have all made important contributions. We would particularly like to thank Nelson Maynard, Mike Heinemann, John Gaudet and Fred Rich for exceptional efforts to help make the project a success.

At the Air Weather Service, we would like to acknowledge the excellent contributions of Capt. Chris Tschan, Lt. Col. Roger Whiton, Kevin Scro, Mary Partington and numerous others. The MSM was begun under Tom Tascione.

At NOAA, Jo Ann Joselyn, Herb Sauer, Gary Heckman, Joe Allen, Dave Evans, Murray Dryer and Ron Zwickl have provided both information and inspiration.

Maj. H. B. Garrett, put in a large number of extra hours developing the revised geostationary particle model used in the MSM.

Dan Baker from the Goddard Space Flight Center has provide very useful advice. David stern and Don Fairfield have also offered assistance.

Bob McPherron from UCLA has made numerous useful contributions to the MSM project including an algorithm for high energy electrons.

At the Los Alamos National Laboratory, Tom Cayton has been very helpful. We would also like to thank the persons responsible for the development of the geostationary satellite detectors, Dick Belian and others, for allowing us the use of their data.

At UTD, Mark Hairston and Rod Heelis have developed E-field input parameter algorithms that are indispensable. We would like to thank them for their efforts.

Jim Bishop, from the University of Michigan, provided valuable assistance in the form of information and models for the ion charge-exchange loss rate.

Dave Gorney and Harry Koons, from the Aerospace Corp. have made useful contributions and have recently provided an algorithm for energetic electrons which we hope to incorporate into the MSM shortly.

At Rice, we could not have survived without Maria Bryne, Umbe Cantu, Norma Crowley, Kimberly M'Carver, Marie Magee, Wayne Smith, and Alex Dessler. Pat Reiff generously shared her knowledge of the polar cap potential drop. John Shade made very important contributions early in the project. Frank Toffoletto has helped to keep the Microvax II running. Duane Pontius and Wayne Smith have been a great source of information about Macintosh systems

IBM, through the auspices of Ken Kennedy and the Rice Department of Computer Science, has generously made available time on the IBM 3081d. This computer time has been invaluable to the project. Ed Hayes and Priscilla Huston and the rest of the staff at the Rice Computer Center have all contributed.

The Apollo Computer, through George Guerin, made an Apollo DN10000 computer available to the project. This computer was used to complete the large task of the computation of the B-field matrices in record time.

We gratefully acknowledge the support of all of the above persons as well as our, sometimes long-suffering, families.

Finally we acknowledge the support of the U. S. Air Force for contract F19628-87-K-0001.

REFERENCES

- Baker, D. N., S. J. Bame, R. D. Belian, W. C. Feldman, J. T. Gosling, P. R. Higbie, E. W. Hones, Jr., D. J. McComas, and R. D. Zwickl, Correlated dynamical changes in the near-Earth and distant magnetotail regions: ISEE-3, *J. Geophys. Res.*, **89**, 3855, 1984.
- Baker, D. N., T. A. Fritz, B. Wilkin, P. R. Higbie, S. M. Kaye, M. G. Kivelson, T. E. Moore, N. Studemann, A. J. Masley, P. H. Smith, and A. L. Vampola, Observation and modeling of energetic particles at synchronous orbit on July 29, 1977, *J. Geophys. Res.*, **87**, 5917, 1982.
- Baker, D. N., P. R. Higbie, E. W. Hones, Jr., and R. D. Belian, The use of > 30 keV electron anisotropies at 6.6 RE to predict magnetospheric substorms, Los Alamos National Laboratory Report LA-UR-2872, 1978.
- Baker, D. N., P. Stauning, E. W. Hones, Jr., P. R. Higbie, and R. D. Belian, Strong electron pitch angle diffusion observed at geostationary orbit, *Geophys. Res. Lett.*, **6**, 205-208, 1979.
- Baumjohann, W., G. Paschmann, and C. A. Cattell, Average plasma properties in the central plasma sheet, *J. Geophys. Res.*, **94**, 6597-6606, 1989.
- Erickson, G. M., and R. A. Wolf, Is steady convection possible in the Earth's magnetotail?, *Geophys. Res. Lett.*, **7**, 897-900, 1980.
- Frank, L. A., J. A. VanAllen, and J. D. Craven, Large diurnal variations of geomagnetically trapped and of precipitated electrons observed at low altitudes, *J. Geophys. Res.*, **69**, 3155-3167, 1964.
- Foster, J. C., J. M. Holt, R. G. Musgrove and D. S. Evans, Ionospheric Convection Associated with Discrete Levels of Particle Precipitation, *Geophys. Res. Lett.*, **13**, 656, 1986.
- Garrett, Henry B., and Sherman E. DeForest, An Analytical Simulation of the Geostationary Plasma Environment, *Planet. Space Sci.*, **27**, 1101, 1979.
- Garrett, H. B., D. C. Schwank, and S. E. DeForest, A statistical analysis of the low-energy geosynchronous plasma environment-1. electrons, *Planet. Space Sci.*, **29**, 1021-1044, 1981.
- Garrett, H. B., D. C. Schwenk, and S. E. DeForest, A Statistical Analysis of the Low-energy Geosynchronous Plasma Environment - - II Protons, *Planet. Space Sci.*, **29**, 1045, 1981a.
- Garrett, H. B., and J. Gaudet, Revised models of the geosynchronous orbit plasma environment, USAF GL internal report, 1989.
- Gloeckler, G., and D. C. Hamilton, AMPTE ion composition results, *Phys. Scripta.*, **T18**, 73-84, 1987.
- Gussenhoven, M. S., D. A. Hardy, and N. Heinemann, Systematics of the equatorward diffuse auroral boundary, *J. Geophys. Res.*, **88**, 5692-5708, 1983.

Hamilton, D. C., G. Gloeckler, F. M. Ipavich, W. Stüdemann, B. Wilken, and G. Kremser, Ring current development during the great geomagnetic storm of February 1986, *J. Geophys. Res.*, 93, 14343-14355, 1988.

Hardy, D. A., M. S. Gussenhoven, and D. Brautigam, A statistical model of auroral ion precipitation, *J. Geophys. Res.*, 94, 370-392, 1989.

Hardy, D. A., M. S. Gussenhoven, and E. Holeman, A statistical model of auroral electron precipitation, *J. Geophys. Res.*, 90, 4229-4248, 1985.

Harel, M., R. A. Wolf, P. H. Reiff, R. W. Spiro, W. J. Burke, F. J. Rich, and M. Smiddy, Quantitative simulation of a magnetospheric substorm 1, model logic and overview, *J. Geophys. Res.*, 86, 2217-2241, 1981.

Heppner, J. P., and N. C. Maynard, Empirical high-latitude electric field models, *J. Geophys. Res.*, 92, 4467-4489, 1987.

Horwitz, J. L., S. Menteer, J. Turnley, J. L. Burch, J. D. Winningham, C. R. Chappell, J. D. Craven, L. A. Frank, and D. W. Slater, Plasma boundaries in the inner magnetosphere, *J. Geophys. Res.*, 91, 8861-8882, 1986.

Huang, C. Y., and L. A. Frank, A statistical study of the central plasma sheet, *Geophys. Res. Lett.*, 13, 652-655, 1986.

Iijima, T., and T. A. Potemra, Large-scale characteristics of field-aligned currents associated with substorms, *J. Geophys. Res.*, 83, 599, 1978.

Kennel, C. F., and H. E. Petschek, Limit on stably trapped particle fluxes, *J. Geophys. Res.*, 71, 1-28, 1966.

King, Joseph H., Interplanetary Medium Data Book - Supplement 4, 1985-1988, NSSDC/WDC-A-R&S 89-17, 1989.

Kivelson, M. G., Magnetospheric electric fields and their variation with geomagnetic activity, *Rev. Geophys. Space Phys.*, 14, 189-197, 1976.

Lennartsson, W., and R. D. Sharp, A comparison of 0.1-17 keV/e ion composition in the near equatorial magnetosphere between quiet and disturbed conditions, *J. Geophys. Res.*, 87, 6109, 1982.

Lennartsson, W., and R. D. Sharp, Achievements of the plasma composition experiment on ISEE-1 during the IMS, *Achievements of the International Magnetospheric Study (IMS)*, ESA SP-217., 283-287, 1984.

Lu, G., P. H. Reiff, R. A. Heelis, M. R. Hairston, and J. L. Karty, Distribution of convection potential around the polar cap boundary as a function of the interplanetary magnetic field, *J. Geophys. Res.*, 94, 13447-13461, 1989.

Lyons, L. R., R. M. Thorne, and C. F. Kennel, Pitch angle diffusion of radiation belt electrons within the plasmasphere, *J. Geophys. Res.*, 77, 3455, 1972.

McPherron, R. L., and R. H. Manka, Dynamics of the 1054 UT March 22, 1979 substorm event: CDAW-6, *J. Geophys. Res.*, 90, 1175-1190, 1985.

- Owens, H. D., and L. A. Frank, Electron omnidirectional intensity contours in the Earth's outer radiation zone at the magnetic equator, *J. Geophys. Res.*, **73**, 199-208, 1968.
- Rich, F. J., and N. C. Maynard, Consequences of using simple analytic functions for the high-latitude convection electric field, *J. Geophys. Res.*, **94**, 3687-3701, 1989.
- Richmond, A. D., M. Blanc, B. A. Emery, R. H. Wand, B. G. Fejer, R. F. Woodman, S. Ganguly, P. Amayenc, R. A. Behnke, C. Calderon, and J. V. Evans, An empirical model of quiet-day ionospheric electric fields at middle and low latitudes, *J. Geophys. Res.*, **85**, 4658-4664, 1980.
- Schumaker, T. L., M. S. Gussenhoven, D. A. Hardy, and R. L. Carovillano, The relationship between diffuse auroral and plasma sheet electron distributions near local midnight, *J. Geophys. Res.*, **94**, 10061-10078, 1989.
- Spiro, R. W., R. A. Heelis, and W. B. Hanson, Ion convection and the formation of the midlatitude F region ionization trough, *J. Geophys. Res.*, **83**, 4255, 1978.
- Spiro, R. W., R. A. Wolf, and B. G. Fejer, Penetration of high-latitude-electric-field effects to low latitudes during SUNDIAL 1984, *Ann. Geophys.*, **6**, 39-50, 1988.
- Spjeldvik, W. N., and P. L. Rothwell, The radiation belts, in *Handbook of Geophysics and the Space Environment*, edited by A. T. Stair, Jr., Air Force Geophysics Laboratory, Air Force Systems Command, 1985.
- Tsyganenko, N. A., Global quantitative models of the geomagnetic field in the cislunar magnetosphere for different disturbance levels, *Planet. Space Sci.*, **35**, 1347-1358, 1987.
- Tsyganenko, N. A., A magnetospheric magnetic field model with a warped tail current sheet, *Planet. Space Sci.*, **37**, 5-20, 1989.
- Tsyganenko, N. A., and A. V. Usmanov, Determination of the magnetospheric current system parameters and development of experimental geomagnetic field models based on data from IMP and HEOS satellites, *Planet. Space Sci.*, **30**, 985-998, 1982.
- VanAllen, J. A., Particle description of the magnetosphere, in *Physics of the Magnetosphere*, edited by R. L. Carovillano, pp. 147-217, D. Reidel Publ. Co., Dordrecht-Holland, 1968.
- Vasyliunas, V. M., A survey of low-energy electrons in the evening sector of the magnetosphere with OGO 1 and OGO 3, *J. Geophys. Res.*, **73**, 2839-2884, 1968.
- Wolf, R. A., The quasi-static (slow-flow) region of the magnetosphere, in *Solar Terrestrial Physics*, edited by R. L. Carovillano and J. M. Forbes, pp. 303-368, D. Reidel, Hingham, MA, 1983.